POLITECNICO
MILANO 1863

SCUOLA DI INGEGNERIA INDUSTRIALE
E DELL'INFORMAZIONE

Numerical Analysis of Loosely Coupled Schemes for Fluid-Structure Interaction in presence of Large Added-Mass Effects

Tesi di Laurea Magistrale in
Mathematical Engineering - Ingegneria Matematica

Author: **Renee Crispo**

Student ID: 244634
Advisor Politecnico di Milano: Prof. Christian Vergara – LABS, Dipartimento di Chimica, Materiali e Ingegneria Chimica
Advisor Sorbonne Univeristé: Miguel A. Fernández – INRIA & CNRS
Academic Year: 2024-2025

Ai miei genitori, Elena e Rosario,
e a mia sorella, Lara.

Non cercare le risposte che potrebbero non esserci.
Non ora. Non puoi fare altro che vivere le domande.

Abstract

Fluid–Structure Interaction (FSI) refers to a class of phenomena which describe the mutual influence between fluid flows and deformable solids: the motion of one directly affects the other by exchanging energy. Applications can be found across multiple disciplines, from aeroelastic instabilities in airplane wings to blood flows in arteries.

FSI problems pose various numerical challenges due to their nonlinear, multiphysics nature and the coupling between fluid and structure. The main issues that must be faced are related to the geometrical and physical coupling, which must impose continuity of the velocity and the stresses at the interface. Loosely coupled schemes offer computational efficiency by decoupling the fluid and solid subproblems, but their stability and accuracy in the incompressible regime are affected by the added-mass effect.

The purpose of this work is to explore a class of loosely coupled time-splitting schemes based on Robin-like interface conditions. Building on prior work focused on Robin-Robin coupling, we aim to establish energy-based stability criteria and derive a priori error estimates for the Robin-Neumann scheme. Moreover, an alternative strategy will be investigated, the Neumann-Robin scheme. The reversed coupling configuration is shown to potentially enhance stability through additional damping effects on the structural side.

The analysis is conducted in a linearized setting for the first part. Later, we extend the study to a non-linear problem with a moving domain. All the theoretical findings are validated through a series of numerical experiments in 2D and 3D, which confirm the effectiveness of the proposed schemes.

Keywords: Fluid-structure interaction, Robin-Neumann scheme, Neumann-Robin scheme, loosely coupled scheme, stability analysis, a priori error estimates, added mass.

Abstract in lingua italiana

Le Interazioni Fluido-Struttura (FSI) rappresentano una classe di fenomeni che descrivono l'influenza reciproca tra il flusso di un fluido e un solido deformabile: il moto di uno influenza direttamente quello dell'altro, attraverso uno scambio di energia. Applicazioni di tali fenomeni si ritrovano in numerose discipline, dalle instabilità aeroelastiche nelle ali degli aeroplani al flusso sanguigno nelle arterie.

I problemi di FSI presentano notevoli difficoltà numeriche a causa della loro natura non lineare e multifisica, oltre che per il forte accoppiamento tra le due componenti. Le principali sfide riguardano la gestione dell'accoppiamento geometrico e fisico, che impone la continuità delle velocità e delle tensioni all'interfaccia. Gli approcci debolmente accoppiati offrono un'elevata efficienza computazionale grazie alla separazione dei sottoproblemi del fluido e della struttura, ma la loro stabilità e accuratezza nel regime incomprimibile possono risentire dell'effetto di massa aggiunta.

L'obiettivo di questa tesi è studiare una classe di schemi di tipo time-splitting debolmente accoppiati basati su condizioni al contorno di tipo Robin. A partire dai risultati ottenuti per lo schema Robin–Robin, si sviluppano criteri di stabilità basati sull'energia e si derivano stime d'errore a priori per lo schema Robin–Neumann. Verrà inoltre analizzata una configurazione alternativa, lo schema Neumann–Robin, che si dimostra in grado di introdurre un effetto di smorzamento aggiuntivo sul lato strutturale, migliorando potenzialmente la stabilità del metodo.

L'analisi è condotta inizialmente in un contesto linearizzato. Successivamente, lo studio viene esteso al problema non lineare con un dominio deformabile in tempo. I risultati teorici sono validati attraverso simulazioni numeriche bidimensionali e tridimensionali, che confermano la validità e l'efficacia degli schemi proposti.

Parole chiave: Interazione fluido-struttura, schema Robin-Neumann, schema Neumann-Robin, schema debolmente acccopiato, analisi di stabilitá, massa aggiunta.

Contents

1 | Introduction and motivations

Contents

This chapter begins by illustrating real-life scenarios of fluid-structure interaction problem, in order to highlight the importance of these phenomena. The discussion proceeds emphasizing the main modeling challenges, characterized by geometrical and physical coupling, with an overview on the existing numerical approaches. It will highlight the added-mass effect and how it influences on the stability of the schemes. The chapter concludes outlining the objectives of the thesis, and focusing on the methods and new contributions to the field.

1.1. The importance of FSI problems

The oscillations produced by wind on a bridge, the trembling of an airplane wing during a flight or blood pulses through vessels share an underlying phenomenon: the interplay between fluids and structures. These events, referred to as *Fluid–Structure Interactions* (FSI), are multiphysics phenomena in which a moving fluid directly interacts with a deformable structure by exchanging energy. The momentum generated by the motion of the fluid induces a structural deformation in the solid, which in turn modifies the surrounding flow field, generating a two-way coupling that could give rise to complex dynamics. It is evident that the fluid and structure behaviors are closely dependent: the solid is not a passive boundary, but it actively participates in the whole dynamics.

Real-life scenarios modeled by FSI could be found across multiple disciplines. In civil

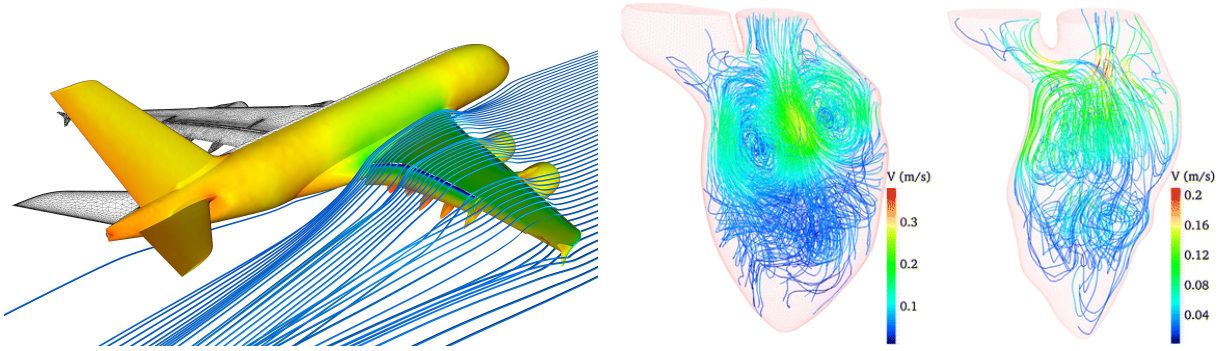

Figure 1.1: Example of fluid-structure interaction simulations: wind streamlines around a plane wing (on the left) and blood flow in the heart (on the right).

engineering, the interaction between fluid flows and bridges, tall buildings or offshore platforms could lead to vibrations and eventually to a catastrophic failure. An emblematic case is represented by the Tacoma Bridge collapse in 1940 an event in which aeroelastic instabilities led to the dramatic failure of a major piece of infrastructure. Similar aeroelastic phenomena, known as flutter and galloping [5, 42], are still central challenges in structural and aerospace engineering. Indeed, these phenomena could compromise the safety of airplanes: high speeds, flexible wings and resonance between wind and structure could trigger the formation of critical oscillations. An example could be found in supersonic aircrafts or turbine blades. To mitigate risks, engineers simulate fluid-structure interactions in wind tunnels in order to identify any potential instability and make the necessary adjustments. In biomedical engineering, where blood flowing through arteries and veins thanks to heartbeat pumps constitute another crucial example [22, 29, 50]. Simulations of blood flows that continuously deforms vessel walls are fundamental in order to model pathological conditions and designing medical devices, like stents, plaques, or heart valves, tailored to each patient [4, 15, 61]. Figure 1.1 shows a couple of examples of FSI simulations.

Therefore, there is the need of introducing accurate FSI mathematical and numerical methods, not only for academic purposes, but to extends the research field to aereospace and mechanical industries, as well as medical labs.

1.2. An overview on FSI problems

A fluid-structure interaction problem is characterized by four components:

(i) a fluid, governed by the equations of fluid dynamics in a domain Ω^{f};

(ii) a solid, governed by the equations of solid mechanics in a domain Ω^{s};

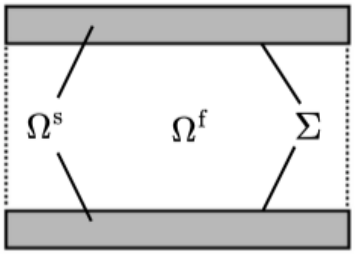

Figure 1.2: Schematic representation of a fluid–structure interaction problem with an internal flow Ω^f and a thick deformable structure Ω^s, separated by an interface Σ.

(iii) the interface between the fluid and solid domain, where suitable coupling conditions must be enforced;

(iv) the fluid domain Ω^f, which is itself an unknown of the problem.

An illustrative example of an FSI problem configuration is shown in Figure 1.2.

The fluid is usually modeled as incompressible and viscous, governed by Stokes or Navier-Stokes equations, while the solid could considered as a deformable elastic body, governed by the elastodynamic equations. In this context, a distinction is often made between *elastic* and *hyperelastic* materials. Elastic models assume a linear relation between stress and strain, which is accurate only for small deformations. On the other hand, hyperelastic models are designed to capture large, nonlinear deformations. Moreover, it is relevant to distinguish between *thick* and *thin* structures: the former occupies a volumetric region, while the latter are modeled by a reduced-dimensional equation, which must accurately capture the bending. Some examples of thick structures could be vascular walls, as they are composed of several layers, while examples of thin structures are plates or shells.

Since the fluid and structure are dependent on each other, the coupling conditions come in action on the interface. These conditions should enforce the *kinematic continuity* (mass conservation), which guarantees that the velocity of the fluid matches the one of the solid, as well as a *dynamic equilibrium*, imposing the balance of the stresses. The first condition results in having no-slip and no-penetration constraints, so that no relative motion is produced between the fluid and the structure. The second conditions ensure Newton's third law (principle of action-reaction).

From a numerical point of view, multiple challenges arise, related to the nonlinearities and multi-physics nature of the problem. Immediately, two issues stand out:

(i) the intrinsic nonlinearity of the governing equations for the structure and the fluid (*constitutive nonlinearities*);

(ii) the treatment of the interface position (*geometrical nonlinearity*);

together with two different types of coupling:

(iii) the displacement of the structure must match the displacement of the fluid domain (*geometrical adherence*);

(iv) the dynamic and kinematic coupling conditions must guarantee continuity between the two subproblems (*physical coupling*).

1.2.1. Numerical resolution strategies

In order to solve the FSI system at the numerical level, the geometrical coupling and the physical one must be clearly distinguished and treated.

Geometrical coupling. The problem of the interface position [46, 50] derives from the fact that the fluid domain is not known a prior and it is itself an unknown of the problem. This requires suitable numerical strategies to handle the evolution of the interface: on one hand, implicit approaches employing iterative methods, or explicit methods by extrapolating the solution at the previous time-steps [1, 38, 45]. The explicit treatment produces a limitation on the time-step in order to ensure stability [26].

One of the most used technique to deal with the geometric nonlinearity is the Arbitrary Lagrangian-Eulerian (ALE) formulation [19, 40]. The core idea is to construct an hybrid formulation combining the advantages of both the Eulerian (fixed mesh, well-suited for fluids) and Lagrangian (moving mesh, well-suited for solids) formulations: the problem is described on a moving domain, extending the displacement of the structure to the whole computational mesh. When ALE is employed, particular attention must be given to the mesh motion. Indeed, as the mesh follows the structural displacement, large deformations may lead to highly skewed grid elements, affecting stability and accuracy of the flow solver. Other limitations of this method are represented by topological changes of the domain, such as contact or self-intersection. Strategies for mesh motion include harmonic extension and adaptive remeshing techniques are often necessary, but they introduce additional computational cost. Alternative approaches that have been developed are the *fictitious domain method* and the *immersed boundary method* (IBM).

Physical coupling. On the other hand, regarding the physical coupling, two main approaches have been developed and studied in the literature over the years: *monolithic approaches* and *partitioned* (or *segregated*) *approaches*.

Monolithic procedures allow to solve the fluid and solid problems simultaneously, in a fully coupled implicit formulation. These methods guarantee a consistent treatment of the interface conditions as they are naturally embedded in the global system. As a consequence, monolithic approaches are proved to be characterized by an elevated degree of stability and robustness. Despite these advantages, monolithic methods present significant computational challenges. The unified formulation produces a nonlinear algebraic system of very large dimension, which combine the ill-conditioning associated with incompressible fluid equations and the high stiffness of elastic solids. Efficient solution of these systems requires advanced linear solvers, such as iterative methods enhanced with block preconditioners [38] that exploit the natural partitioning between fluid and solid unknowns, and multigrid techniques [3, 32] that accelerate iterative solvers by exploiting grids of different resolutions to eliminate errors at all scales. Furthermore, the implementation of monolithic schemes is considerably demanding as they often require ad hoc coding, which is typically less modular than two separate solvers. As a result, although monolithic methods provide a highly stable framework, their practical use has been restricted to academia, and it has not found solid ground in commercial and industrial applications. Ongoing research is devoted to improving their computational efficiency and scalability.

On the other hand, partitioned methods allow the independent solution of the fluid and structure subproblems using separate solvers. The interfacial quantities, that is velocities and normal stresses, are exchanged in a staggered manner, by introducing subiterations, between the fluid and the solid at each time step. Within this framework, it is possible to distinguish *loosely coupled* and *strongly coupled methods*. A scheme is said to be loosely coupled (or *weakly*) if few subiterations are performed at each time instance. As a result, the coupling conditions are not exactly satisfied at each time step, and the explicit nature of these schemes may present to instability issues. On the contrary, when the number of subiterations is sufficiently high so that the scheme becomes equivalent to the implicit one up to a prescribed tolerance, the coupling conditions are satisfied exactly after time discretization, and one says that the scheme is strongly coupled.

Therefore, it can be stated that both monolithic system and strongly partitioned schemes lead to the same solution, satisfying the same interface conditions, up to a suitable tolerance. On the other side, partitioned schemes provide different solutions, very appealing from the computational time, but possibly suffering from stability issues.

This thesis will focus on loosely coupled approaches for the physical scheme, as they are particularly suitable for investigating different coupling strategies within a computationally efficient framework. It will not deal with the geometrical coupling problem since in

the linear case the computational domain remains fixed in time. In contrast, for the non-linear problem, the geometrical coupling will be handled through an explicit treatment of the ALE map.

1.2.2. The added mass effect

As the communication between the fluid and solid subproblem happens via the coupling conditions, the most natural choice to handle the coupling is the Dirichlet-Neumann (DN) partition. This follows directly by the structure of the coupling conditions: the kinematic one can be perceives as a Dirichlet-type condition, while the dynamic condition can be seen as a Neumann-like condition.

This formulation is particular sensitive to the *added-mass effect* [16, 31]. Indeed, the interaction between solid and fluid could generate disturbances in the velocity filed causing pressure variations. These variations act as additional forces on the structure and can be interpreted as an artificial increase in its effective mass. The added-mass effect is particularly destabilizing when the fluid and structure densities are comparable, as it tends to amplify instabilities. When using a DN partition, the added mass is treated explicitly. As a consequence, if the added mass is big compared to the actual structural mass, the scheme could suffer of slow convergence and instabilities.

It is important to point out that the added-mass effect is manifested whether the fluid is compressible or incompressible, but there is a significant different in its character, as evidenced in [59]. When working with compressible fluids, the added mass is proportional to the time step. On the contrary, the incompressibility constraint, while it ensures volume conservation, creates an added mass independent of the time step τ, and it reaches a threshold when τ becomes smaller and smaller. Therefore, although such methods are feasible in compressible settings (see, [21]), they are much more critical in the incompressible regime.

1.3. Previous works and proposed solutions

In the literature, each of the above issues has been extensively investigated and many solutions have been proposed. This section aims to discuss the most relevant contributions in the field.

As mentioned before, the coupling conditions can be imposed implicitly [1, 2], where the the fluid and structure unknowns at the current time step appear together in the interface conditions, hence requiring iterative methods, or explicitly [9, 36, 37], in which

information from previous time steps are employed. Since explicit method usually lead to instabilities, implicit methods have always been preferred, even though the computational cost increases a lot (see [18, 23, 34, 43]).

In order to contrast the computational cost of implicit methods, different strategies have been proposed, such as fixed-point iterations or Newton-based approaches. Fixed-point iterations are relatively straightforward but may require a large number of iterations to converge and it exhibits linear convergence rates. An attempt to fasten the convergence was done in [51] thank to the method of *artificial compressibility*: in simple words, the incompressibility constraint is being relaxed by introducing an extra term named artificial compressibility. Eventually, at convergence, this term must vanish.

On the other hand, Newton's method offers quadratic convergence near the solution, at the cost of a higher computational effort per iteration, since it requires the evaluation of the Jacobian matrix at each time instance. In this framework, inexact Newton methods have been proposed as a first solution. These methods are based on the idea of solving an approximation of the linear systems: in [38, 57] the Jacobian is approximated using finite differences, while in [34] the coupled tangent operator is substituted by a linear operator. Later on, exact Newton methods have been addressed as a way to cope with the loss in accuracy caused by inexact methods: in particular, [23, 24] introduce a new approach that relies on linearized solvers to consistently compute the various Jacobian required in Newton's algorithm.

An alternative way of treating the coupling conditions is represented by *semi-implicit methods* [26, 47]. The idea behind these methods is to create an implicit/explicit splitting: the added mass effect is treated implicitly, while the remaining contributions (geometrical nonlinearities, dissipation and convection) are treated explicitly. In such a way, algebraic fractional-step method, such as Chorin-Temam [17, 55] or Yosida [49], can be adapted to solve FSI problems by splitting the explicit and implicit part. As a result, the computational cost evidently drops.

On the other hand, in order to overcome issue the added-mass effect issue, modified interface conditions have been introduced, but often without a rigorous theoretical error analysis or convergence rates. Among them, Robin-type couplings have gained increasing attention [1]. These conditions combine Dirichlet and Neumann data into a single weighted relation, effectively blending velocity and stress information across the interface. Therefore, the DN partition are a specific case of this class of methods, for a specific choice of the wight α. The most common approaches that use Robin-like conditions are the Robin-Neumann (RN) [8, 25, 28, 36] or Robin-Robin (RR) [1, 2, 10, 12, 13, 35] schemes.

Both RR and RN schemes have been studied on thin and thick solids. In [25], the analysis of RN on thick solid structures identified that this scheme may introduce a splitting error that is not uniform with respect to the mesh size h. The proposed analysis led to the conclusion that this accuracy loss is due to the non-uniformity in the discretization of the elastic operator, induced by the thick solid wall itself.

In all these cases, when employing a Robin-like condition, it has been observed that the careful selection of the Robin parameters (see [33, 37]) plays a crucial role: optimal tuning can suppress the artificial amplification due to added mass and lead to stability properties comparable to those of fully implicit monolithic solvers, but at a lower computational cost. In [33], the optimal values for the Robin-Robin transmission conditions are found using the optimized Schwarz method, where the objective is to minimize the reduction factor, describing the error rate at each iteration. The values of the parameters differ based on the model that has been considered.

In recent years, numerous studies have focused on achieving optimal convergence rates, but most of them focused on the thin solid case. In [44], a novel coupled nonstationary Ritz projection was introduced, enabling optimal convergence in the L^2 norm. Subsequently, [54] proposed a stable scheme based on a carefully designed combination of the Crank–Nicolson and BDF2 methods, along with a stress-type stabilization, achieving a convergence rate of order $\mathcal{O}(\tau^{3/2})$. Recently, optimal accuracy has been achieved in a linear setting with Robin-Robin conditions for the thick solid case in [13], showing linear convergence rates.

An alternative to the classical coupling conditions is *Nitsche's method*. It was originally developed to impose weakly the coupling on the interface by including the kinematic and dynamic conditions directly into the weak formulation of the problem, and it was later extended to FSI problems, as in [9, 28]. It can be seen as a generalization of a Robin-like condition, as the added terms represent a weighted penalization between stresses and velocities, but the weighting term is chosen from the discretization and physical properties of the problem. Moreover, this method allows the natural management of non matching grids, as in [3].

1.4. Objectives of the thesis

In the framework of loosely coupled approaches, the present thesis builds upon the work of [13] done on Robin-Robin coupling conditions, extending the stability and convergence analysis to the case of time-splitting schemes for linear and nonlinear FSI problems based on Robin-Neumann coupling conditions. In particular, it aims to

(i) study the stability and provide a complete convergence analysis of the Robin-Neumann scheme.

(ii) investigate a reversed coupling approach (Neumann-Robin loosely coupled scheme), associating the Robin condition to the solid and the Neumann condition to the fluid.

(iii) evaluate the performance of these schemes on benchmark problems and compare them with existing partitioned strategies, that is the Robin-Robin scheme.

The stability and convergence analysis are conducted in a linearized settings, both for the Neumann-Robin and the Robin-Neumann scheme. Then the same schemes will be applied on the nonlinear problem to show their performance in more complex configurations.

The choice of studying the reversed scheme is motivated by the similarity of the coupling structure to the Robin-Robin setting. In fact, assigning the Robin condition to the solid might introduce a stabilizing effect analogous to viscous damping, which enhances the energy dissipation on the structural side. The stability analysis will show that this method is conditionally stable for both the used time discretization schemes.

The theoretical results are supported by numerical simulations using:

- `FreeFem++`, a software development platform that provides a simple, yet powerful, framework suited for the chosen linear test case;
- `FELiScE`[1], a `C++` library for FEM developed by the COMMEDIA project team at Inria Paris, as the simulations of the nonlinear problem required a significantly higher computational cost.

This thesis introduces some novelties to the study of loosely coupled schemes for FSI. In particular, it addresses:

(i) a rigorous analysis of the convergence properties of the Robin-Neumann scheme on the linear problem, confirming the expected linear convergence rate;

(ii) the first detailed investigation of the stability of the Neumann-Robin scheme in both linear and nonlinear settings.

By establishing rigorous error bounds and testing these approaches in both linear and nonlinear settings, this thesis aims to bridge the gap between the theoretical advances achieved for Robin-Robin and Robin-Neumann couplings and the practical applicability of partitioned methods in more general scenarios.

[1] Finite Elements for LIfe SCiences and Engineering: `https://team.inria.fr/commedia/software/felisce/`

Part I

Linear Setting

The first part of this thesis is devoted to the analysis of a linear fluid-structure interaction model. The primary objective is to rigorously investigate the stability and convergence properties of loosely coupled time-splitting schemes based on Robin-Neumann and Neumann-Robin interface conditions.

This part is structured as follows:

Chapter 2. It introduces the model problem, its variational and discrete formulation. The stability analysis of the proposed method is also presented, including different choices for the time discretization of the solid (Backward Euler and mid-point).

Chapter 3. It aims at presenting and exploring the effect of stability when reversing the coupling conditions in the Robin-Neumann scheme, where the Robin condition is applied to the solid and the Neumann condition to the fluid. The scheme will be proven to be conditionally stable for both time discretizations.

Chapter 4. In this chapter, starting from the converge proof for the heat equation, we provide a detailed convergence analysis of the Robin-Neumann scheme, establishing sub-optimal to start, and later quasi-optimal error estimates in the energy norm.

Chapter 5. Finally, the numerical results are presented in order to validate the theoretical findings while varying different parameters, and comparing the results with the Robin-Robin scheme. The results will confirm the expected linear convergence rate and the improved accuracy achieved through the use of correction iterations.

2 | FSI problem and Robin-based schemes

Contents

This chapter introduces the linear FSI model problem and its variational formulation. We then derive fully discrete schemes based on different time discretizations for the coupling conditions, focusing on backward Euler and mid-point schemes. Particular attention is devoted to the stability properties of the resulting Robin–Neumann loosely coupled algorithms, for which we provide a detailed analysis. We discuss the effect of correction iterations as a strategy to enhance both accuracy and robustness.

2.1. Problem description

We consider a coupled problem given by a linear Stokes-elasticity system, where we suppose that the solid undergoes infinitesimal displacements, and that the convective effects are negligible in the fluid. We define a reference configuration $\Omega = \Omega^{\mathrm{f}} \cup \Omega^{\mathrm{s}}$, represented by a rectangular tube $\Omega^{\mathrm{f}} = [0, L] \times [0, R]$ and $\Omega^{\mathrm{s}} = [0, L] \times [R, R + H_{\mathrm{s}}]$, where H_{s} is the thickness of the solid (see Figure 2.1). The interface between fluid and solid is denoted by Σ. The remaining parts of the fluid and solid boundaries are indicated by Γ^{f} and Γ^{s},

respectively, such that $\partial\Omega^{\mathrm{f}} = \Gamma^{\mathrm{f}} \cup \Sigma$ and $\partial\Omega^{\mathrm{s}} = \Gamma^{\mathrm{s}} \cup \Sigma$. The outward pointing normals of $\partial\Omega^i$ are denoted as $\boldsymbol{n}^i$, for $i \in \{\mathrm{s}, \mathrm{f}\}$.

As the solid deformation is infinitesimal, the domain Ω can be considered fixed in time, meaning also that the fluid-solid interface Σ does not move or deform during the simulation. Therefore, there is no geometric coupling to be accounted for: the position of the interface is prescribed and remains constant, so the fluid mesh does not need to be updated to track the structure. In this setting, the coupling between fluid and solid is purely physical, meaning that the interaction occurs only through the transmission of forces and stresses across the interface, rather than through the motion of the geometry itself. This simplification allows us to focus on the stability and accuracy of the numerical scheme for the physical coupling without the additional complexity associated with moving or deforming meshes.

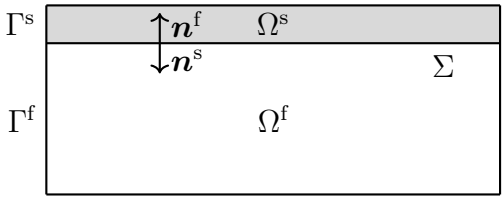

Figure 2.1: Geometrical description of the computational domain for the linear problem.

For a given final time $T > 0$, we look for the velocity of the fluid $\boldsymbol{u} : \Omega^{\mathrm{f}} \times (0,T) \to \mathbb{R}^2$ and the pressure $p : \Omega^{\mathrm{f}} \times (0,T) \to \mathbb{R}$, the displacement of the solid $\boldsymbol{d} : \Omega^{\mathrm{s}} \times (0,T) \to \mathbb{R}^2$ and the velocity of the solid $\dot{\boldsymbol{d}} : \Omega^{\mathrm{s}} \times (0,T) \to \mathbb{R}^2$ that solve

$$
\begin{cases}
\rho^{\mathrm{f}} \partial_t \boldsymbol{u} - \mathbf{div}\, \boldsymbol{\sigma}^{\mathrm{f}}(\boldsymbol{u}, p) = \mathbf{0} & \text{in } \Omega^{\mathrm{f}} \times (0,T), \\
\operatorname{div} \boldsymbol{u} = 0 & \text{in } \Omega^{\mathrm{f}} \times (0,T), \\
\boldsymbol{u} = \mathbf{0} & \text{on } \Gamma^{\mathrm{f}} \times (0,T), \\
\rho^{\mathrm{s}} \partial_t \dot{\boldsymbol{d}} - \mathbf{div}\, \boldsymbol{\sigma}^{\mathrm{s}}(\boldsymbol{d}) = \mathbf{0} & \text{in } \Omega^{\mathrm{s}} \times (0,T), \\
\dot{\boldsymbol{d}} = \partial_t \boldsymbol{d} & \text{in } \Omega^{\mathrm{s}} \times (0,T), \\
\boldsymbol{d} = \mathbf{0} & \text{on } \Gamma^{\mathrm{s}} \times (0,T), \\
\boldsymbol{u} = \dot{\boldsymbol{d}} & \text{on } \Sigma \times (0,T), \\
\boldsymbol{\sigma}^{\mathrm{f}}(\boldsymbol{u}, p)\boldsymbol{n}^{\mathrm{f}} = -\boldsymbol{\sigma}^{\mathrm{s}}(\boldsymbol{d})\boldsymbol{n}^{\mathrm{s}} & \text{on } \Sigma \times (0,T),
\end{cases}
\tag{2.1}
$$

complemented with appropriate initial conditions: $\boldsymbol{d}(0,\cdot) = \boldsymbol{d}_0$, $\dot{\boldsymbol{d}}(0,\cdot) = \dot{\boldsymbol{d}}_0$ in Ω^{s} and $\boldsymbol{u}(0,\cdot) = \boldsymbol{u}_0$ in Ω^{f}. The symbol $\boldsymbol{\sigma}^{\mathrm{f}}(\boldsymbol{u}, p)$ refers to the Cauchy stress tensor, which describes

the internal forces per unit area within a fluid due to pressure and viscosity μ. It is related to the strain rate tensor $\boldsymbol{\epsilon}(\mathbf{u})$, which is the symmetric part of the gradient of the velocity, measuring the local deformation rate of the fluid, as in the following relation:

$$\boldsymbol{\sigma}^{\mathrm{f}}(\boldsymbol{u}, p) := 2\mu\boldsymbol{\epsilon}(\boldsymbol{u}) - p\boldsymbol{I}, \quad \boldsymbol{\epsilon}(\boldsymbol{u}) := \frac{1}{2}\left(\nabla\boldsymbol{u} + (\nabla\boldsymbol{u})^{\mathrm{T}}\right). \tag{2.2}$$

On the other hand, the symbol $\boldsymbol{\sigma}^{\mathrm{s}}(\boldsymbol{d})$ stands for the linearized solid stress tensor, which is assumed to be given in terms of $\boldsymbol{d}$ by

$$\boldsymbol{\sigma}^{\mathrm{s}}(\boldsymbol{d}) := 2L_1\boldsymbol{\epsilon}(\boldsymbol{d}) + L_2(\operatorname{div}\boldsymbol{d})\boldsymbol{I}, \tag{2.3}$$

where $L_1 > 0, L_2 \geq 0$ denote the so called Lamé coefficients of the solid, defined as:

$$L_1 := \frac{E}{1+\nu}, \qquad L_2 := \frac{E\nu}{(1+\nu)(1-2\nu)},$$

with E denoting the Young's modulus and ν the Poisson's ratio of the solid. Young's modulus E is a measure of the stiffness of the solid, while Poisson's ratio ν describes the ratio of transverse strain to axial strain in the material, characterizing its elastic behavior.

From a physical point of view, the boundary conditions, represented by $(2.1)_3$ and $(2.1)_6$, impose respectively a non-penetration and no-slip condition for the fluid and a clamped boundary for the solid. In hemodynamic, condition $(2.1)_6$ would be normally replaced by a Robin condition in order to model the surrounding tissue's elasticity. However, here we consider a simplified case imposing a homogeneous Dirichlet condition.

In addition to boundary conditions, the first coupling condition $(2.1)_7$ is a kinematic condition, which enforces the continuity of the velocities at the interface, so that the solid and the fluid move together, preventing any slipping between the two. The second one $(2.1)_8$ is a dynamic condition, where the equilibrium of forces is imposed at the interface, ensuring that the stress exerted by the fluid on the solid is equal and opposite to the stress exerted by the solid on the fluid, following Newton's third law.

2.1.1. Variational formulation

To obtain the variational formulation of (2.1), it is necessary to define the following functional spaces:

$$\begin{aligned} \boldsymbol{V}^{\mathrm{s}} &:= \left\{\boldsymbol{v} \in \boldsymbol{H}^1(\Omega^{\mathrm{s}}) \,:\, \boldsymbol{v} = \mathbf{0} \text{ on } \Gamma^{\mathrm{s}}\right\}, \\ \boldsymbol{V}^{\mathrm{f}} &:= \left\{\boldsymbol{v} \in \boldsymbol{H}^1(\Omega^{\mathrm{f}}) \,:\, \boldsymbol{v} = \mathbf{0} \text{ on } \Gamma^{\mathrm{f}}\right\}, \\ M^{\mathrm{f}} &:= L^2_0(\Omega^{\mathrm{f}}). \end{aligned} \tag{2.4}$$

Taking $(\boldsymbol{\xi}, \boldsymbol{v}, q) \in \boldsymbol{V}^{\mathrm{s}} \times \boldsymbol{V}^{\mathrm{f}} \times M^{\mathrm{f}}$ as test functions and integrating over the corresponding domains, problem (2.1) satisfies the variational formulation: find $\boldsymbol{u}(t) \in \boldsymbol{V}^{\mathrm{f}}$, $p(t) \in M^{\mathrm{f}}$, $\boldsymbol{d}(t) \in \boldsymbol{V}^{\mathrm{s}}$ and $\dot{\boldsymbol{d}}(t) \in \boldsymbol{V}^{\mathrm{s}}$ such that

$$\begin{aligned} \rho^{\mathrm{s}} \int_{\Omega^{\mathrm{s}}} \partial_t \dot{\boldsymbol{d}} \cdot \boldsymbol{\xi} + a^{\mathrm{s}}(\boldsymbol{d}, \boldsymbol{\xi}) + \int_{\Sigma} \boldsymbol{\lambda} \cdot \boldsymbol{\xi} = 0, \\ \rho^{\mathrm{f}} \int_{\Omega^{\mathrm{f}}} \partial_t \boldsymbol{u} \cdot \boldsymbol{v} + a^{\mathrm{f}}((\boldsymbol{u}, p), (\boldsymbol{v}, q)) - \int_{\Sigma} \boldsymbol{\lambda} \cdot \boldsymbol{v} = 0, \end{aligned} \tag{2.5}$$

for all $(\boldsymbol{\xi}, \boldsymbol{v}, q) \in \boldsymbol{V}^{\mathrm{s}} \times \boldsymbol{V}^{\mathrm{f}} \times M^{\mathrm{f}}$. Notice that in the previous formulation we have indicated with $\boldsymbol{\lambda} = \boldsymbol{\sigma}^{\mathrm{f}}(\boldsymbol{u}, p)\boldsymbol{n}^{\mathrm{f}} (= -\boldsymbol{\sigma}^{\mathrm{s}}(\boldsymbol{d})\boldsymbol{n}^{\mathrm{s}}) \in \boldsymbol{L}^2(\Sigma)$ the fluid normal stresses, obtaining from integration by parts. The bilinear forms of the fluid and of the solid, respectively denoted as $a^{\mathrm{f}}((\boldsymbol{u}, p), (\boldsymbol{v}, q))$ and $a^{\mathrm{s}}(\boldsymbol{d}, \boldsymbol{\xi})$, are given by

$$\begin{aligned} a^{\mathrm{f}}((\boldsymbol{u}, p), (\boldsymbol{v}, q)) &:= 2\mu \int_{\Omega^{\mathrm{f}}} \boldsymbol{\epsilon}(\boldsymbol{u}) : \boldsymbol{\epsilon}(\boldsymbol{v}) - \int_{\Omega^{\mathrm{f}}} p \operatorname{div} \boldsymbol{v} + \int_{\Omega^{\mathrm{f}}} q \operatorname{div} \boldsymbol{u}, \\ a^{\mathrm{s}}(\boldsymbol{d}, \boldsymbol{\xi}) &:= 2L_1 \int_{\Omega^{\mathrm{s}}} \boldsymbol{\epsilon}(\boldsymbol{d}) : \boldsymbol{\epsilon}(\boldsymbol{\xi}) + L_2 \int_{\Omega^{\mathrm{s}}} (\operatorname{div} \boldsymbol{d})(\operatorname{div} \boldsymbol{\xi}). \end{aligned}$$

It is relevant to notice that both the solid and fluid equation in (2.5) involve $\boldsymbol{\lambda}$ arising by the dynamic condition $(2.1)_7$. On the other hand, the the kinematic condition $(2.1)_8$ remains explicitly in the formulation.

For future analysis, we also introduce the elastic energy norm of the solid:

$$\|\boldsymbol{d}\|_{\mathrm{s}} = \sqrt{a^{\mathrm{s}}(\boldsymbol{d}, \boldsymbol{d})}. \tag{2.6}$$

2.1.2. Fully discrete formulations

Given a time step τ, let us define $t_n = n\tau, n \in \mathbb{N}$, as well as the approximation in time of the velocity $\boldsymbol{u}^n \simeq \boldsymbol{u}(t_n)$, of the pressure $p^n \simeq p(t_n)$, of the solid displacement $\boldsymbol{d}^n \simeq \boldsymbol{d}(t_n)$, of the solid velocity $\dot{\boldsymbol{d}}^n = \dot{\boldsymbol{d}}(t_n)$ and of the fluid stresses $\boldsymbol{\lambda}^n \simeq \boldsymbol{\lambda}(t_n)$. For a general quantity f, we introduce the notation

$$\partial_\tau f^n := \frac{f^n - f^{n-1}}{\tau}.$$

Then, problem (2.5) could be solved at each time instance

$$\begin{aligned} \rho^{\mathrm{s}} \int_{\Omega^{\mathrm{s}}} \partial_t \dot{\boldsymbol{d}}^n \cdot \boldsymbol{\xi} + a^{\mathrm{s}}(\boldsymbol{d}^n, \boldsymbol{\xi}) + \int_{\Sigma} \boldsymbol{\lambda}^n \cdot \boldsymbol{\xi} = 0, \\ \rho^{\mathrm{f}} \int_{\Omega^{\mathrm{f}}} \partial_t \boldsymbol{u}^n \cdot \boldsymbol{v} + a^{\mathrm{f}}((\boldsymbol{u}^n, p^n), (\boldsymbol{v}, q)) - \int_{\Sigma} \boldsymbol{\lambda}^n \cdot \boldsymbol{v} = 0, \end{aligned} \tag{2.7}$$

where the coupling conditions $(2.1)_{7,8}$ between the fluid and structure domains

$$\begin{cases} \boldsymbol{u}^n = \dot{\boldsymbol{d}}^n \\ \boldsymbol{\lambda}^n = -\boldsymbol{\sigma}^{\mathrm{s}}(\boldsymbol{d}^n)\boldsymbol{n}^{\mathrm{s}} \end{cases} \quad \text{on } \Sigma$$

are enforced strongly by requiring that the test functions satisfy $\boldsymbol{v} = \boldsymbol{\xi}$ on Σ. As a consequence, when summing together the equations in (2.7), the terms related to the fluid stresses cancel out.

For the spatial discretization, we define the finite element spaces $\boldsymbol{V}_h^{\mathrm{f}} \subset \boldsymbol{V}^{\mathrm{f}}$, $\boldsymbol{V}_h^{\mathrm{s}} \subset \boldsymbol{V}^{\mathrm{s}}$, and $M_h^{\mathrm{f}} \subset M^{\mathrm{f}}$, such that $\dim \boldsymbol{V}_{\mathrm{h}}^{\mathrm{f}} < \infty$, $\dim \boldsymbol{V}_{\mathrm{h}}^{\mathrm{s}} < \infty$, and $\mathrm{dimM}_{\mathrm{h}}^{\mathrm{f}} < \infty$. In particular, we consider a piecewise affine continuous finite elements, where we assume that the fluid and solid meshes, respectively $\mathcal{T}_h^{\mathrm{f}}$ and $\mathcal{T}_h^{\mathrm{s}}$, are fitted on the interface Σ. More precisely, the spaces are:

$$\begin{aligned} \boldsymbol{V}_h^{\mathrm{s}} &:= \left\{ \boldsymbol{v} \in \boldsymbol{V}^{\mathrm{s}} : \boldsymbol{v}|_K \in \mathbb{P}^1(K),\, \forall K \in \mathcal{T}_h^{\mathrm{s}} \right\}, \\ \boldsymbol{V}_h^{\mathrm{f}} &:= \left\{ \boldsymbol{v} \in \boldsymbol{V}^{\mathrm{f}} : \boldsymbol{v}|_K \in \mathbb{P}^1(K),\, \forall K \in \mathcal{T}_h^{\mathrm{f}} \right\}, \\ M_h^{\mathrm{f}} &:= \left\{ v \in M^{\mathrm{f}} : v|_K \in \mathbb{P}^1(K),\, \forall K \in \mathcal{T}_h^{\mathrm{f}} \right\}. \end{aligned} \tag{2.8}$$

Moreover, since the fluid and solid meshes must match at the interface Σ, it is necessary to define the space

$$\boldsymbol{V}_h^{\mathrm{g}} := \mathrm{Tr}_\Sigma\, \boldsymbol{V}_h^{\mathrm{f}} = \mathrm{Tr}_\Sigma\, \boldsymbol{V}_h^{\mathrm{s}}$$

In mixed finite elements formulations with incompressible fluids, the pressure field acts as a Lagrange multiplier for the incompressible constraint. The well-posedness of the fully discrete problem relies on the inf-sup (or Ladyzhenskaya–Babuška–Brezzi) condition, which requires the discrete space for velocities to be larger than the discrete space for pressures. If this condition is not fulfilled, the discrete formulation may admit spurious pressure modes: these are solutions to the Stokes equation but do not correspond to any velocity field. In practice, this issue often arises when equal-order interpolation spaces are used for both velocity and pressure, as we are supposing in (2.8). In order to accommodate the lack of inf-sup condition, the fluid bilinear form is modified adding a pressure stabilized bilinear form (see [7]):

$$a_h^{\mathrm{f}}((\boldsymbol{u}_h, p_h), (\boldsymbol{v}_h, q_h)) = a^{\mathrm{f}}((\boldsymbol{u}_h, p_h), (\boldsymbol{v}_h, q_h)) + \frac{\gamma_{\mathrm{p}} h^2}{\mu} \int_{\Omega^{\mathrm{f}}} \nabla p_h \cdot \nabla q_h, \tag{2.9}$$

with $\gamma_{\mathrm{p}} > 0$ a user-defined parameter.

The fully discrete monolithic formulation is found in Algorithm 2.1.

Algorithm 2.1 Monolithic scheme with BDF1 (MONO-BDF1)

Given $\boldsymbol{u}_h^0, \boldsymbol{d}_h^0, \dot{\boldsymbol{d}}_h^0$, $\forall n \geq 1$, find $(\boldsymbol{u}_h^n, p_h^n, \boldsymbol{d}_h^n, \dot{\boldsymbol{d}}_h^n) \in \boldsymbol{V}_h^{\mathrm{f}} \times M_h^{\mathrm{f}} \times \boldsymbol{V}_h^{\mathrm{s}} \times \boldsymbol{V}_h^{\mathrm{s}}$ such that

$$\rho^{\mathrm{f}} \int_{\Omega^{\mathrm{f}}} \partial_\tau \boldsymbol{u}_h^n \cdot \boldsymbol{v}_h + a_h^{\mathrm{f}}((\boldsymbol{u}_h^n, p_h^n), (\boldsymbol{v}_h, q_h)) + \rho^{\mathrm{s}} \int_{\Omega^{\mathrm{s}}} \partial_\tau \dot{\boldsymbol{d}}_h^n \cdot \boldsymbol{\xi}_h + a^{\mathrm{s}}(\boldsymbol{d}_h^n, \boldsymbol{\xi}_h) = 0$$

for all $(\boldsymbol{v}_h, q_h) \in \boldsymbol{V}_h^{\mathrm{f}} \times M_h^{\mathrm{f}}$ and $\boldsymbol{\xi}_h \in \boldsymbol{V}_h^{\mathrm{s}}$, such that $\boldsymbol{v}_h = \boldsymbol{\xi}_h$ on Σ.

2.2. Loosely partitioned schemes

This thesis will focus on the discretization of problem (2.5) based on a loosely coupled scheme, where we solve the fluid and solid subproblems separately, exchanging information at the interface Σ at each time step.

We can choose different type of treatments to ensure the coupling conditions $(2.1)_{7,8}$ based on linear combinations of the latter ones relying on Robin-like conditions. The use of Robin interface conditions is based on the introduction of the so-called Robin parameter α, which acts as a weight factor between the solid and fluid velocity [1, 36], leading to a general interface condition of the form:

$$\boldsymbol{\sigma}^{\mathrm{s}}(\boldsymbol{d})\boldsymbol{n}^{\mathrm{s}} + \alpha \dot{\boldsymbol{d}} = \alpha \boldsymbol{u} - \boldsymbol{\sigma}^{\mathrm{f}}(\boldsymbol{u}, p)\boldsymbol{n}^{\mathrm{f}}.$$

Among the possible formulations, the two most used choices are: the Robin-Robin (RR) scheme and the Robin-Neumann (RN) scheme, possibly, after time discretization, in their explicit formulations, that is performing just one (or a few) iteration at each time step. In the RR scheme, both the solid and the fluid are treated with Robin conditions, whereas in the RN approach the fluid with a Robin condition and the solid with a Neumann condition.

In particular, regarding the first choice, if a Backward Euler (BDF1) scheme is used both in the solid and in the fluid, the explicit RR scheme, derived in [10], reads as follows:

$$\text{RR-BDF1:} \quad \begin{cases} \boldsymbol{\lambda}^n + \alpha \boldsymbol{u}^n = \alpha \dot{\boldsymbol{d}}^{n-1} + \boldsymbol{\lambda}^{n-1} \\ \boldsymbol{\sigma}^{\mathrm{s}}(\boldsymbol{d}^n)\boldsymbol{n}^{\mathrm{s}} + \alpha \dot{\boldsymbol{d}}^n = \alpha \boldsymbol{u}^{n-1} - \boldsymbol{\lambda}^{n-1} \end{cases} \quad \text{on } \Sigma. \tag{2.10}$$

Notice that in the previous conditions we have used the same parameter α to linearly combine the kinematic and dynamic interface conditions. This is allowed since in the second one we have used $\boldsymbol{\lambda}$ instead of $\boldsymbol{\sigma}^{\mathrm{s}}(\boldsymbol{d})$, exploiting the dynamic condition.

The first equation represents the balance of the stresses in Robin form, blending the

current solid velocity with the previous fluid velocity through α, while the second one represents the update of the fluid stresses.

It is also possible to rewrite the same coupling conditions choosing a mid-point (MD) scheme in the solid, while the fluid still advances with a BDF1 scheme. From now on, this scheme will always be indicated with the only label MD. In particular, introducing the approximation at the intermediate time-step $t^{n-\frac{1}{2}}$ for a general quantity f as

$$f^{n-\frac{1}{2}} := \frac{f^n + f^{n-1}}{2},$$

and substituting it into (2.10), it yields to

$$\text{RR-MD:} \quad \begin{cases} \boldsymbol{\lambda}^n + \alpha \boldsymbol{u}^n = \alpha \dot{\boldsymbol{d}}^{n-\frac{1}{2}} + \boldsymbol{\lambda}^{n-1} \\ \boldsymbol{\sigma}^{\mathrm{s}}(\boldsymbol{d}^{n-\frac{1}{2}})\boldsymbol{n}^{\mathrm{s}} + \alpha \dot{\boldsymbol{d}}^{n-\frac{1}{2}} = \alpha \boldsymbol{u}^{n-1} - \boldsymbol{\lambda}^{n-1} \end{cases} \quad \text{on } \Sigma. \tag{2.11}$$

Regarding the second choice, that is the Robin-Neumann scheme, we have a linear combination of the kinematic and dynamic condition only associated to the fluid problem. The same idea can be applied on the other coupling choice: the Robin-Neumann scheme, where a Robin condition is associated to the fluid subproblem, while a Neumann one is associated to the solid subproblem. Therefore, in its explicit form, the interface conditions read:

$$\text{RN-BDF1:} \quad \begin{cases} \boldsymbol{\lambda}^n + \alpha \boldsymbol{u}^n = \alpha \dot{\boldsymbol{d}}^{n-1} + \boldsymbol{\lambda}^{n-1} \\ \boldsymbol{\sigma}^{\mathrm{s}}(\boldsymbol{d}^n)\boldsymbol{n}^{\mathrm{s}} = -\boldsymbol{\lambda}^n \end{cases} \quad \text{on } \Sigma, \tag{2.12}$$

$$\text{RN-MD:} \quad \begin{cases} \boldsymbol{\lambda}^n + \alpha \boldsymbol{u}^n = \alpha \dot{\boldsymbol{d}}^{n-\frac{3}{2}} + \boldsymbol{\lambda}^{n-1} \\ \boldsymbol{\sigma}^{\mathrm{s}}(\boldsymbol{d}^{n-\frac{1}{2}})\boldsymbol{n}^{\mathrm{s}} = -\boldsymbol{\lambda}^n \end{cases} \quad \text{on } \Sigma. \tag{2.13}$$

The fully discrete formulation of the Robin-Neumann scheme is detailed in Algorithm 2.2 for BDF1 [27] and in Algorithm 2.3 for the mid-point in the solid. The fully discrete formulations of the Robin-Robin schemes can be found in Appendix A.

The coupling conditions are presented with the appropriate ordering. For stability reasons (see Section 2.3), the subproblem linked to the Robin condition must be always solved first.

Note that the fluid stress updates in Algorithms 2.2 and 2.3 are directly derived from the Robin-Neumann coupling conditions. Specifically, equation (2.15) originates from the first equation of (2.12), while equation (2.18) corresponds to the first equation of (2.13). It also should be noted that the interfacial stresses $\boldsymbol{\lambda}_h^n$ are omitted in any implementation:

they are not unknowns of the problem, as they are reconstructed at each iteration and used directly in the fluid and solid subproblem.

2.2.1. Correction iterations

It is relevant to point out that Algorithm 2.2 and 2.3 can be modified by adding correction iterations (see [28]). This means that for each time instance, we iterate over the fluid and solid subproblems until convergence, i.e. up to a suitable tolerance, or for a fixed number of subiterations $K \geq 1$.

After defining the notation

$$\partial_\tau f^{n,k} := \frac{f^{n,k} - f^{n-1}}{\tau}, \quad \text{for } k = 1, \dots, K$$

where f is a generic variable, and $f^{n,k}$ is the approximation of f^n at the k-th subiteration, the semi-discrete formulation of problem (2.1), using BDF1 in the fluid and solid, reads:

$$\begin{cases} \rho^{\mathrm{f}} \dfrac{\boldsymbol{u}^{n,k} - \boldsymbol{u}^{n-1}}{\tau} - \mathbf{div}\, \boldsymbol{\sigma}^{\mathrm{f}}(\boldsymbol{u}^{n,k}, p^{n,k}) = 0 & \text{in } \Omega^{\mathrm{f}}, \\ \operatorname{div} \boldsymbol{u}^{n,k} = 0 & \text{in } \Omega^{\mathrm{f}}, \\ \boldsymbol{\lambda}^{n,k} + \alpha \boldsymbol{u}^{n,k} = \alpha \dot{\boldsymbol{d}}^{n,k-1} + \boldsymbol{\lambda}^{n,k-1} & \text{on } \Sigma, \\ \rho^{\mathrm{s}} \dfrac{\dot{\boldsymbol{d}}^{n,k} - \dot{\boldsymbol{d}}^{n-1}}{\tau} - \mathbf{div}\, \boldsymbol{\sigma}^{\mathrm{s}}(\dot{\boldsymbol{d}}^{n,k}) = 0 & \text{in } \Omega^{\mathrm{s}}, \\ \dot{\boldsymbol{d}}^{n,k} = \dfrac{\boldsymbol{d}^{n,k} - \boldsymbol{d}^{n-1}}{\tau} & \text{in } \Omega^{\mathrm{s}}, \\ \boldsymbol{\sigma}^{\mathrm{s}}(\boldsymbol{d}^{n,k}) \boldsymbol{n}^{\mathrm{s}} = -\boldsymbol{\lambda}^{n,k} & \text{on } \Sigma, \end{cases}$$

for $k = 1, \dots, K$. The fully discrete formulation is detailed in Algorithm 2.4. Same discussion applies to the mid-point scheme, and its fully discrete formulation can be found in Algorithm 2.5.

Note that when $K = 1$, Algorithm 2.4 simply reduces to Algorithm 2.2, while Algorithm 2.5 reduces to Algorithm 2.3. On the other hand, when $K \to +\infty$, the Robin coupling condition enforces $\alpha \boldsymbol{u}^n = \alpha \dot{\boldsymbol{d}}^n$ in both algorithms. In the limit, the solution of each algorithm converges to that of a fully implicit monolithic scheme, recovering strong coupling at the interface.

Algorithm 2.2 Loosely coupled scheme with Robin-Neumann interface conditions and BDF1 time discretization (LC-RN-BDF1)

Given $\boldsymbol{u}_h^0, \boldsymbol{d}_h^0, \dot{\boldsymbol{d}}_h^0, \boldsymbol{\lambda}_h^0$ and α, $\forall n \geq 1$:

1. Fluid subproblem: find $(\boldsymbol{u}_h^n, p_h^n) \in \boldsymbol{V}_h^{\mathrm{f}} \times M_h^{\mathrm{f}}$ such that

$$\rho^{\mathrm{f}} \int_{\Omega^{\mathrm{f}}} \partial_\tau \boldsymbol{u}_h^n \cdot \boldsymbol{v}_h + a_h^{\mathrm{f}}((\boldsymbol{u}_h^n, p_h^n), (\boldsymbol{v}_h, q_h)) + \alpha \int_\Sigma (\boldsymbol{u}_h^n - \dot{\boldsymbol{d}}_h^{n-1}) \cdot \boldsymbol{v}_h = \int_\Sigma \boldsymbol{\lambda}_h^{n-1} \cdot \boldsymbol{v}_h \tag{2.14}$$

   for all $(\boldsymbol{v}_h, q_h) \in \boldsymbol{V}_h^{\mathrm{f}} \times M_h^{\mathrm{f}}$.
2. Fluid-stress update: set $\boldsymbol{\lambda}_h^n \in \boldsymbol{V}_h^{\mathrm{g}}$ as

$$\boldsymbol{\lambda}_h^n = \boldsymbol{\lambda}_h^{n-1} + \alpha(\dot{\boldsymbol{d}}_h^{n-1} - \boldsymbol{u}_h^n) \quad \text{on } \Sigma. \tag{2.15}$$

3. Solid subproblem: find $(\boldsymbol{d}_h^n, \dot{\boldsymbol{d}}_h^n) \in \boldsymbol{V}_h^{\mathrm{s}} \times \boldsymbol{V}_h^{\mathrm{s}}$, such that $\dot{\boldsymbol{d}}_h^n = \partial_\tau \boldsymbol{d}_h^n$ and

$$\rho^{\mathrm{s}} \int_{\Omega^{\mathrm{s}}} \partial_\tau \dot{\boldsymbol{d}}_h^n \cdot \boldsymbol{\xi}_h + a^{\mathrm{s}}(\boldsymbol{d}_h^n, \boldsymbol{\xi}_h) = -\int_\Sigma \boldsymbol{\lambda}_h^n \cdot \boldsymbol{\xi}_h \tag{2.16}$$

   for all $\boldsymbol{\xi}_h \in \boldsymbol{V}_h^{\mathrm{s}}$.

Algorithm 2.3 Loosely coupled scheme with Robin-Neumann interface conditions and mid-point time discretization (LC-RN-MD)

Given $\boldsymbol{u}_h^0, \boldsymbol{d}_h^0, \dot{\boldsymbol{d}}_h^0, \boldsymbol{\lambda}_h^0$ and α, $\forall n \geq 1$:

1. Fluid subproblem: find $(\boldsymbol{u}_h^n, p_h^n) \in \boldsymbol{V}_h^{\mathrm{f}} \times M_h^{\mathrm{f}}$ such that

$$\rho^{\mathrm{f}} \int_{\Omega^{\mathrm{f}}} \partial_\tau \boldsymbol{u}_h^n \cdot \boldsymbol{v}_h + a_h^{\mathrm{f}}((\boldsymbol{u}_h^n, p_h^n), (\boldsymbol{v}_h, q_h)) + \alpha \int_\Sigma (\boldsymbol{u}_h^n - \dot{\boldsymbol{d}}_h^{n-\frac{3}{2}}) \cdot \boldsymbol{v}_h = \int_\Sigma \boldsymbol{\lambda}_h^{n-1} \cdot \boldsymbol{v}_h \tag{2.17}$$

   for all $(\boldsymbol{v}_h, q_h) \in \boldsymbol{V}_h^{\mathrm{f}} \times M_h^{\mathrm{f}}$.
2. Fluid-stress update: set $\boldsymbol{\lambda}_h^n \in \boldsymbol{V}_h^{\mathrm{g}}$ as

$$\boldsymbol{\lambda}_h^n = \boldsymbol{\lambda}_h^{n-1} + \alpha(\dot{\boldsymbol{d}}_h^{n-\frac{3}{2}} - \boldsymbol{u}_h^n) \quad \text{on } \Sigma. \tag{2.18}$$

3. Solid subproblem: find $(\boldsymbol{d}_h^n, \dot{\boldsymbol{d}}_h^n) \in \boldsymbol{V}_h^{\mathrm{s}} \times \boldsymbol{V}_h^{\mathrm{s}}$, such that $\dot{\boldsymbol{d}}_h^{n-\frac{1}{2}} = \partial_\tau \boldsymbol{d}_h^n$ and

$$\rho^{\mathrm{s}} \int_{\Omega^{\mathrm{s}}} \partial_\tau \dot{\boldsymbol{d}}_h^n \cdot \boldsymbol{\xi}_h + a^{\mathrm{s}}(\boldsymbol{d}_h^{n-\frac{1}{2}}, \boldsymbol{\xi}_h) = -\int_\Sigma \boldsymbol{\lambda}_h^n \cdot \boldsymbol{\xi}_h \tag{2.19}$$

   for all $\boldsymbol{\xi}_h \in \boldsymbol{V}_h^{\mathrm{s}}$.

Algorithm 2.4 Loosely coupled scheme with Robin-Neumann interface conditions, BDF1 time discretization and $K \geq 1$ correction iterations (LC-RN-BDF1-CI)

Given $\boldsymbol{u}_h^0, \boldsymbol{d}_h^0, \dot{\boldsymbol{d}}_h^0, \boldsymbol{\lambda}_h^0$ and α, for each time step $n \geq 1$:

- Initialize iteration $k = 0$:

$$\boldsymbol{u}_h^{n,0} = \boldsymbol{u}_h^{n-1}, \quad \boldsymbol{d}_h^{n,0} = \boldsymbol{d}_h^{n-1}, \quad \dot{\boldsymbol{d}}_h^{n,0} = \dot{\boldsymbol{d}}_h^{n-1}, \quad \boldsymbol{\lambda}_h^{n,0} = \boldsymbol{\lambda}_h^{n-1}.$$

- Repeat for $k = 1, \dots, K$:
  1. Fluid subproblem: find $(\boldsymbol{u}_h^{n,k}, p_h^{n,k}) \in \boldsymbol{V}_h^{\mathrm{f}} \times M_h^{\mathrm{f}}$ such that

$$\rho^{\mathrm{f}} \int_{\Omega^{\mathrm{f}}} \partial_\tau \boldsymbol{u}_h^{n,k} \cdot \boldsymbol{v}_h + a_h^{\mathrm{f}}((\boldsymbol{u}_h^{n,k}, p_h^{n,k}), (\boldsymbol{v}_h, q_h)) + \alpha \int_\Sigma (\boldsymbol{u}_h^{n,k} - \dot{\boldsymbol{d}}_h^{n,k-1}) \cdot \boldsymbol{v}_h = \int_\Sigma \boldsymbol{\lambda}_h^{n,k-1} \cdot \boldsymbol{v}_h$$

     for all $(\boldsymbol{v}_h, q_h) \in \boldsymbol{V}_h^{\mathrm{f}} \times M_h^{\mathrm{f}}$.
  2. Fluid-stress update: set $\boldsymbol{\lambda}_h^n \in \boldsymbol{V}_h^{\mathrm{g}}$ as

$$\boldsymbol{\lambda}_h^{n,k} = \boldsymbol{\lambda}_h^{n,k-1} + \alpha(\dot{\boldsymbol{d}}_h^{n,k-1} - \boldsymbol{u}_h^{n,k}) \quad \text{on } \Sigma.$$

  3. Solid subproblem: find $\boldsymbol{d}_h^{n,k}, \dot{\boldsymbol{d}}_h^{n,k} \in \boldsymbol{V}_h^{\mathrm{s}}$, such that $\dot{\boldsymbol{d}}_h^{n,k} = \frac{\boldsymbol{d}_h^{n,k} - \boldsymbol{d}_h^{n-1}}{\tau}$ and

$$\rho^{\mathrm{s}} \int_{\Omega^{\mathrm{s}}} \partial_\tau \dot{\boldsymbol{d}}_h^{n,k} \cdot \boldsymbol{\xi}_h + a^{\mathrm{s}}(\boldsymbol{d}_h^{n,k}, \boldsymbol{\xi}_h) = -\int_\Sigma \boldsymbol{\lambda}_h^{n,k} \cdot \boldsymbol{\xi}_h$$

     for all $\boldsymbol{\xi}_h \in \boldsymbol{V}_h^{\mathrm{s}}$.
- Update:

$$\boldsymbol{u}_h^n := \boldsymbol{u}_h^{n,K}, \quad \boldsymbol{d}_h^n := \boldsymbol{d}_h^{n,K}, \quad \dot{\boldsymbol{d}}_h^n := \dot{\boldsymbol{d}}_h^{n,K}, \quad \boldsymbol{\lambda}_h^n := \boldsymbol{\lambda}_h^{n,K}.$$

2.3. Energy stability analysis

In this section we analyze the energy stability of the Robin-Neumann scheme for Algorithm 2.2 and 2.3. We will show that the choice of the time discretization on the solid has a big impact on the stability of the scheme. In particular, Algorithm 2.2 is conditionally energy stable, while Algorithm 2.3 is unconditionally unstable in the energy norm.

2.3.1. Stability for the LC-RN-BDF1 scheme

In the case of BDF1 time discretization, the result we obtain is that the scheme is conditionally stable under a CFL-like condition, where the time step τ is bounded by a quantity inversely proportional to the Robin parameter α. The precise statement is provided in the following theorem.

Algorithm 2.5 Loosely coupled scheme with Robin-Neumann interface conditions, MD time discretization and $K \geq 1$ correction iterations (LC-RN-MD-CI)

Given $\boldsymbol{u}_h^0, \boldsymbol{d}_h^0, \dot{\boldsymbol{d}}_h^0, \boldsymbol{\lambda}_h^0$ and α, for each time step $n \geq 1$:

- Initialize iteration $k = 0$:

$$\boldsymbol{u}_h^{n,0} = \boldsymbol{u}_h^{n-1}, \quad \boldsymbol{d}_h^{n,0} = \boldsymbol{d}_h^{n-1}, \quad \dot{\boldsymbol{d}}_h^{n,0} = \dot{\boldsymbol{d}}_h^{n-1}, \quad \boldsymbol{\lambda}_h^{n,0} = \boldsymbol{\lambda}_h^{n-1}.$$

- Repeat for $k = 1, \ldots, K$:
  1. Fluid subproblem: find $(\boldsymbol{u}_h^{n,k}, p_h^{n,k}) \in \boldsymbol{V}_h^{\mathrm{f}} \times M_h^{\mathrm{f}}$ such that

$$\rho^{\mathrm{f}} \int_{\Omega^{\mathrm{f}}} \partial_\tau \boldsymbol{u}_h^{n,k} \cdot \boldsymbol{v}_h + a_h^{\mathrm{f}}((\boldsymbol{u}_h^{n,k}, p_h^{n,k}), (\boldsymbol{v}_h, q_h)) + \alpha \int_\Sigma (\boldsymbol{u}_h^{n,k} - \dot{\boldsymbol{d}}_h^{n-\frac{1}{2},k-1}) \cdot \boldsymbol{v}_h = \int_\Sigma \boldsymbol{\lambda}_h^{n,k-1} \cdot \boldsymbol{v}_h$$

     for all $(\boldsymbol{v}_h, q_h) \in \boldsymbol{V}_h^{\mathrm{f}} \times M_h^{\mathrm{f}}$.
  2. Fluid-stress update: $\boldsymbol{\lambda}_h^n \in \boldsymbol{V}_h^{\mathrm{g}}$ as

$$\boldsymbol{\lambda}_h^{n,k} = \boldsymbol{\lambda}_h^{n,k-1} + \alpha(\dot{\boldsymbol{d}}_h^{n-\frac{1}{2},k-1} - \boldsymbol{u}_h^{n,k}) \quad \text{on } \Sigma.$$

  3. Solid subproblem: find $\boldsymbol{d}_h^{n,k}, \dot{\boldsymbol{d}}_h^{n,k} \in \boldsymbol{V}_h^{\mathrm{s}}$, such that $\dot{\boldsymbol{d}}_h^{n-\frac{1}{2},k} = \frac{\boldsymbol{d}_h^{n,k} - \boldsymbol{d}_h^{n-1}}{\tau}$ and

$$\rho^{\mathrm{s}} \int_{\Omega^{\mathrm{s}}} \partial_\tau \dot{\boldsymbol{d}}_h^{n,k} \cdot \boldsymbol{\xi}_h + a^{\mathrm{s}}(\boldsymbol{d}_h^{n-\frac{1}{2},k}, \boldsymbol{\xi}_h) = -\int_\Sigma \boldsymbol{\lambda}_h^{n,k} \cdot \boldsymbol{\xi}_h$$

     for all $\boldsymbol{\xi}_h \in \boldsymbol{V}_h^{\mathrm{s}}$.
- Update:

$$\boldsymbol{u}_h^n := \boldsymbol{u}_h^{n,K}, \quad \boldsymbol{d}_h^n := \boldsymbol{d}_h^{n,K}, \quad \dot{\boldsymbol{d}}_h^n := \dot{\boldsymbol{d}}_h^{n,K}, \quad \boldsymbol{\lambda}_h^n := \boldsymbol{\lambda}_h^{n,K}.$$

Theorem 2.1. *Let $\{(\boldsymbol{u}_h^n, p_h^n, \boldsymbol{d}_h^n, \dot{\boldsymbol{d}}_h^n, \boldsymbol{\lambda}_h^n)\}_{n \geq 1}$ be given by Algorithm 2.2. Assuming that*

$$\tau < \delta_h^{-1} := \frac{\rho^{\mathrm{s}} h}{2\alpha C_{\mathrm{T}}^2}, \tag{2.20}$$

the following energy estimates hold, for $n \geq 1$ and $n\tau \leq T$:

$$E_h^n + \sum_{m=1}^{n} G_h^m \leq \exp\left(\frac{\delta_h T}{1 - \tau\delta_h}\right) E_h^0,$$

where, for all $n \geq 1$*:*

$$E_h^n := \frac{\rho^{\mathrm{f}}}{2}\|\boldsymbol{u}_h^n\|_{0,\Omega^{\mathrm{f}}}^2 + \frac{\rho^{\mathrm{s}}}{2}\|\dot{\boldsymbol{d}}_h^n\|_{0,\Omega^{\mathrm{s}}}^2 + \frac{1}{2}\|\boldsymbol{d}_h^n\|_{\mathrm{s}}^2 + \frac{\tau}{2\alpha}\|\boldsymbol{\lambda}_h^n\|_{0,\Sigma}^2,$$

$$G_h^n := \frac{\rho^{\mathrm{f}}}{2}\|\boldsymbol{u}_h^n - \boldsymbol{u}_h^{n-1}\|_{0,\Omega^{\mathrm{f}}}^2 + \frac{\rho^{\mathrm{s}}}{4}\|\dot{\boldsymbol{d}}_h^n - \dot{\boldsymbol{d}}_h^{n-1}\|_{0,\Omega^{\mathrm{s}}}^2 + \frac{1}{2}\|\boldsymbol{d}_h^n - \boldsymbol{d}_h^{n-1}\|_{\mathrm{s}}^2$$
$$+ \frac{\tau}{2\alpha}\|\boldsymbol{\lambda}_h^n - \boldsymbol{\lambda}_h^{n-1}\|_{0,\Sigma}^2 + 2\tau\mu\|\boldsymbol{\epsilon}(\boldsymbol{u}_h^n)\|_{0,\Sigma}^2 + \frac{\gamma_{\mathrm{p}}h^2\tau}{\mu}\|\nabla p_h^n\|_{0,\Omega^{\mathrm{f}}}^2.$$

Proof. By combining (2.14) with (2.15), we have that

$$\rho^{\mathrm{f}}\int_{\Omega^{\mathrm{f}}}\partial_\tau \boldsymbol{u}_h^n\cdot\boldsymbol{v}_h + a_h^{\mathrm{f}}((\boldsymbol{u}_h^n, p_h^n),(\boldsymbol{v}_h, q_h)) = \int_\Sigma \boldsymbol{\lambda}_h^n\cdot\boldsymbol{v}_h \tag{2.21}$$

A key point is that we can see Algorithm 2.2 as a kinematic perturbation of the corresponding strongly coupled scheme, Algorithm 2.1, because adding (2.21) to (2.16) and taking $\boldsymbol{v}_h| = \boldsymbol{\xi}_h$ on Σ, we retrieve Algorithm 2.1. Therefore, owing to (2.15) we have

$$\boldsymbol{u}_h^n = \dot{\boldsymbol{d}}_h^n + \frac{1}{\alpha}(\boldsymbol{\lambda}_h^{n-1} - \boldsymbol{\lambda}_h^n) + (\dot{\boldsymbol{d}}_h^{n-1} - \dot{\boldsymbol{d}}_h^n) \quad \text{on } \Sigma. \tag{2.22}$$

The perturbation is given by the last two terms of (2.22). Notice that the amount of perturbation increases as the Robin parameter α diminishes, which is hence expected to degrade accuracy.

We test the fluid subproblem (2.14) with $(\boldsymbol{v}_h, q_h) = \tau(\boldsymbol{u}_h^n, p_h^n)$:

$$\rho^{\mathrm{f}}\tau\int_{\Omega^{\mathrm{f}}}\partial_\tau \boldsymbol{u}_h^n\cdot\boldsymbol{u}_h^n + \tau a^{\mathrm{f}}((\boldsymbol{u}_h^n, p_h^n),(\boldsymbol{u}_h^n, p_h^n)) + \frac{\gamma_{\mathrm{p}}h^2\tau}{\mu}\int_{\Omega^{\mathrm{f}}}\nabla p_h^n\cdot\nabla p_h^n = \tau\int_\Sigma \boldsymbol{\lambda}_h^n\cdot\boldsymbol{u}_h^n.$$

Applying the standard identity

$$(a-b)a = \frac{1}{2}[a^2 - b^2 + (a-b)^2], \tag{2.23}$$

on the first term, we get

$$\frac{\rho^{\mathrm{f}}}{2}\|\boldsymbol{u}_h^n\|_{0,\Omega^{\mathrm{f}}}^2 + \frac{\rho^{\mathrm{f}}}{2}\|\boldsymbol{u}_h^n - \boldsymbol{u}_h^{n-1}\|_{0,\Omega^{\mathrm{f}}}^2 + 2\tau\mu\|\boldsymbol{\epsilon}(\boldsymbol{u}_h^n)\|_{0,\Omega^{\mathrm{f}}}^2 + \frac{\gamma_{\mathrm{p}}h^2\tau}{\mu}\|\nabla p_h^n\|_{0,\Omega^{\mathrm{f}}}^2$$
$$= \frac{\rho^{\mathrm{f}}}{2}\|\boldsymbol{u}_h^{n-1}\|_{0,\Omega^{\mathrm{f}}}^2 + \tau\int_\Sigma \boldsymbol{\lambda}_h^n\cdot\boldsymbol{u}_h^n.$$

Then, the solid subproblem (2.16) is tested with $\boldsymbol{\xi}_h = \tau \dot{\boldsymbol{d}}_h^n$:

$$\rho^{\mathrm{s}} \int_{\Omega^{\mathrm{s}}} \tau \partial_\tau \dot{\boldsymbol{d}}_h^n \cdot \dot{\boldsymbol{d}}_h^n + \tau a^{\mathrm{s}}(\boldsymbol{d}_h^n, \dot{\boldsymbol{d}}_h^n) = -\tau \int_\Sigma \boldsymbol{\lambda}_h^n \cdot \dot{\boldsymbol{d}}_h^n.$$

The first integral is being treated in the same way as before, using (2.23), to obtain

$$\begin{aligned}\frac{\rho^{\mathrm{s}}}{2}\|\dot{\boldsymbol{d}}_h^n\|_{0,\Omega^{\mathrm{s}}}^2 + \frac{\rho^{\mathrm{s}}}{2}\|\dot{\boldsymbol{d}}_h^n - \dot{\boldsymbol{d}}_h^{n-1}\|_{0,\Omega^{\mathrm{s}}}^2 + \frac{1}{2}\|\boldsymbol{d}_h^n\|_{\mathrm{s}}^2 + \frac{1}{2}\|\boldsymbol{d}_h^n - \boldsymbol{d}_h^{n-1}\|_{\mathrm{s}}^2 \\ = \frac{\rho^{\mathrm{s}}}{2}\|\dot{\boldsymbol{d}}_h^{n-1}\|_{0,\Omega^{\mathrm{s}}}^2 + \frac{1}{2}\|\boldsymbol{d}_h^{n-1}\|_{\mathrm{s}}^2 - \tau \int_\Sigma \boldsymbol{\lambda}_h^n \cdot \dot{\boldsymbol{d}}_h^n.\end{aligned}$$

Summing up the two resulting equations, we obtain:

$$\begin{aligned}&\frac{\rho^{\mathrm{f}}}{2}\|\boldsymbol{u}_h^n\|_{0,\Omega^{\mathrm{f}}}^2 + \frac{\rho^{\mathrm{s}}}{2}\|\dot{\boldsymbol{d}}_h^n\|_{0,\Omega^{\mathrm{s}}}^2 + \frac{\rho^{\mathrm{f}}}{2}\|\boldsymbol{u}_h^n - \boldsymbol{u}_h^{n-1}\|_{0,\Omega^{\mathrm{f}}}^2 + \frac{\rho^{\mathrm{s}}}{2}\|\dot{\boldsymbol{d}}_h^n - \dot{\boldsymbol{d}}_h^{n-1}\|_{0,\Omega^{\mathrm{s}}}^2 \\ &\quad + 2\tau\mu\|\boldsymbol{\epsilon}(\boldsymbol{u}_h^n)\|_{0,\Omega^{\mathrm{f}}}^2 + \frac{1}{2}\|\boldsymbol{d}_h^n\|_{\mathrm{s}}^2 + \frac{1}{2}\|\boldsymbol{d}_h^n - \boldsymbol{d}_h^{n-1}\|_{\mathrm{s}}^2 + \frac{\gamma_{\mathrm{p}} h^2 \tau}{\mu}\|\nabla p_h^n\|_{0,\Omega^{\mathrm{f}}}^2 \\ &\quad = \frac{\rho^{\mathrm{f}}}{2}\|\boldsymbol{u}_h^{n-1}\|_{0,\Omega^{\mathrm{f}}}^2 + \frac{\rho^{\mathrm{s}}}{2}\|\dot{\boldsymbol{d}}_h^{n-1}\|_{0,\Omega^{\mathrm{s}}}^2 + \frac{1}{2}\|\boldsymbol{d}_h^{n-1}\|_{\mathrm{s}}^2 + \int_\Sigma \tau \boldsymbol{\lambda}_h^n \cdot (\boldsymbol{u}_h^n - \dot{\boldsymbol{d}}_h^n).\end{aligned}$$

Since all the terms are positive, with positive coefficients, the only term that remains to be bounded is the one on the right-hand side:

$$T_1 := \tau \int_\Sigma \boldsymbol{\lambda}_h^n \cdot (\boldsymbol{u}_h^n - \dot{\boldsymbol{d}}_h^n).$$

By inserting (2.22) into this expression, we have

$$T_1 = \underbrace{\frac{\tau}{\alpha}\int_\Sigma \boldsymbol{\lambda}_h^n \cdot (\boldsymbol{\lambda}_h^{n-1} - \boldsymbol{\lambda}_h^n)}_{T_2} \underbrace{+\tau \int_\Sigma \boldsymbol{\lambda}_h^n \cdot (\dot{\boldsymbol{d}}_h^{n-1} - \dot{\boldsymbol{d}}_h^n)}_{T_3}.$$

For the first term we can simply use (2.23) to obtain:

$$T_2 = \frac{\tau}{2\alpha}\left(\|\boldsymbol{\lambda}_h^{n-1}\|_{0,\Sigma}^2 - \|\boldsymbol{\lambda}_h^n\|_{0,\Sigma}^2 - \|\boldsymbol{\lambda}_h^n - \boldsymbol{\lambda}_h^{n-1}\|_{0,\Sigma}^2\right).$$

Notice that when summing over multiple time steps, the first two terms form a telescoping sum, leading to cancellation of intermediate terms.

For the second term, we proceed by using the Cauchy-Schwarz inequality, the discrete trace inequality (see [6])

$$\|\dot{\boldsymbol{d}}_h^n - \dot{\boldsymbol{d}}_h^{n-1}\|_{0,\Sigma}^2 \leq C_{\mathrm{T}} h^{-1}\|\dot{\boldsymbol{d}}_h^n - \dot{\boldsymbol{d}}_h^{n-1}\|_{0,\Omega^{\mathrm{s}}}^2. \tag{2.24}$$

and Young's inequality, as follows

$$\begin{aligned} T_3 &\geq -\tau \|\boldsymbol{\lambda}_h^n\|_{0,\Sigma} \|\dot{\boldsymbol{d}}_h^{n-1} - \dot{\boldsymbol{d}}_h^n\|_{0,\Sigma} \\ &\geq -\tau C_{\mathrm{T}} h^{-\frac{1}{2}} \|\boldsymbol{\lambda}_h^n\|_{0,\Sigma} \|\dot{\boldsymbol{d}}_h^{n-1} - \dot{\boldsymbol{d}}_h^n\|_{0,\Omega^{\mathrm{s}}} \\ &\geq -\underbrace{\frac{2\alpha C_{\mathrm{T}}^2}{h\rho^{\mathrm{s}}}}_{:=\delta_h} \frac{\tau^2}{2\alpha} \|\boldsymbol{\lambda}_h^n\|_{0,\Sigma}^2 - \frac{\rho^{\mathrm{s}}}{4} \|\dot{\boldsymbol{d}}_h^{n-1} - \dot{\boldsymbol{d}}_h^n\|_{0,\Omega^{\mathrm{s}}}^2. \end{aligned}$$

At the end, summing all the terms over $m = 1, \ldots, n$, we get the following estimate:

$$E_h^n + \sum_{m=1}^{n} G_h^m \leq E_h^0 + \sum_{m=1}^{n} \delta_h \frac{\tau^2}{2\alpha} \|\boldsymbol{\lambda}_h^m\|_{0,\Sigma}^2 \leq E_h^0 + \tau \sum_{m=1}^{n} \delta_h E_h^m. \tag{2.25}$$

Now we can apply Gronwall's lemma [39, Lemma 5.1]:

Lemma 2.1. *Let τ, B, and a_m, b_m, c_m, γ_m, for integers $m \geq 0$, be nonnegative numbers such that*

$$a_n + k \sum_{m=0}^{n} b_m \leq \tau \sum_{m=0}^{n} \gamma_m a_m + \tau \sum_{m=0}^{n} c_m + B \quad \text{for } n \geq 0. \tag{2.26}$$

Suppose that $\tau\gamma_m < 1$, for all m, and set $\sigma_m \equiv (1 - \tau\gamma_m)^{-1}$. Then,

$$a_n + \tau \sum_{m=0}^{n} b_m \leq \exp\left(\tau \sum_{m=0}^{n} \sigma_m \gamma_m\right) \left\{\tau \sum_{m=0}^{n} c_m + B\right\} \quad \text{for } n \geq 0. \tag{2.27}$$

The last part of the proof follows directly from the application of Lemma 2.1 to (2.25). Indeed, we can notice that (2.25) and (2.26) have the same structure, identifying

$$a_n = E_h^n, \quad b_m = G_h^m, \quad c_m = 0, \quad \gamma_m = \delta_h, \quad B = E_h^0 \tag{2.28}$$

The assumption $\tau\gamma_m < 1$, in our case, leads to the CFL-like condition:

$$\tau < \delta_h^{-1} := \frac{\rho^{\mathrm{s}}}{2\alpha C_{\mathrm{T}}^2} h.$$

Substituting (2.28) into (2.27) and using that $n\tau \leq T$, we get

$$\tau \sum_{m=0}^{n} \sigma_m \gamma_m = \tau \sum_{m=1}^{n} \frac{\delta_h}{1 - \tau\delta_h} = \frac{\delta_h n\tau}{1 - \tau\delta_h} \leq \frac{\delta_h T}{1 - \tau\delta_h}.$$

which concludes the proof. □

It is relevant to notice that the estimate provided by Theorem 2.1 guarantees that the energy is bounded for a fixed spatial mesh, under condition (2.20). Indeed, the exponential term blows up when $h \to 0$ for a fixed final time T.

Remark 2.1. *A similar result for a thin-walled solid model could be obtained by using the same arguments. In this case, the discrete trace inequality is not needed in the bound of T_2. This reduces the stability condition* (2.20) *to*

$$\tau < \delta^{-1} := \frac{\rho^{\mathrm{s}}\epsilon}{2\alpha},$$

and we have the following energy estimate:

$$E_h^n + \sum_{m=1}^{n} G_h^m \leq \exp\left(\frac{\delta T}{1-\tau\delta}\right) E_h^0.$$

2.3.2. Stability for the LC-RN-MD scheme

The result stated in Theorem 2.1 strongly relies on the temporal dissipation of the solid time discretization, i.e. on the term

$$\frac{\rho^{\mathrm{s}}}{2}\sum_{m=1}^{n} \|\dot{\boldsymbol{d}}_h^m - \dot{\boldsymbol{d}}_h^{m-1}\|_{0,\Omega^{\mathrm{s}}}^2,$$

in order to control the solid velocity perturbation introduced in (2.22). This is likely to yield instability in the case in which the solid is discretized in time with a neutrally stable scheme, i.e. energy preserving, such as the mid-point scheme. We obtain the following result.

Theorem 2.2. *Let $\{(\boldsymbol{u}_h^n, p_h^n, \boldsymbol{d}_h^n, \dot{\boldsymbol{d}}_h^n \boldsymbol{\lambda}_h^n)\}_{n\geq 1}$ be given by Algorithm 2.3. The following energy estimates hold, for $n \geq 1$:*

$$E_h^n + \sum_{m=1}^{n} G_h^m \leq E_h^0 + \sum_{m=1}^{n} \frac{2\alpha C_{\mathrm{T}}}{h\rho^{\mathrm{s}}}\frac{\tau}{2\alpha}\|\boldsymbol{\lambda}_h^m\|_{0,\Sigma}^2 + \sum_{m=1}^{n}\frac{\rho^{\mathrm{s}}}{4}\|\dot{\boldsymbol{d}}_h^{m-\frac{3}{2}} - \dot{\boldsymbol{d}}_h^{m-\frac{1}{2}}\|_{0,\Omega^{\mathrm{s}}}^2,$$

where

$$E_h^n := \frac{\rho^{\mathrm{f}}}{2}\|\boldsymbol{u}_h^n\|_{0,\Omega^{\mathrm{f}}}^2 + \frac{\rho^{\mathrm{s}}}{2}\|\dot{\boldsymbol{d}}_h^n\|_{0,\Omega^{\mathrm{s}}}^2 + \frac{1}{2}\|\boldsymbol{d}_h^n\|_{\mathrm{s}}^2 + \frac{\tau}{2\alpha}\|\boldsymbol{\lambda}_h^n\|_{0,\Sigma}^2,$$

$$G_h^n := \frac{\rho^{\mathrm{f}}}{2}\|\boldsymbol{u}_h^n - \boldsymbol{u}_h^{n-1}\|_{0,\Omega^{\mathrm{f}}}^2 + \frac{\tau\alpha}{2}\|\dot{\boldsymbol{d}}_h^{n-\frac{3}{2}} - \boldsymbol{u}_h^n\|_{0,\Sigma}^2 + 2\tau\mu\|\boldsymbol{\epsilon}(\boldsymbol{u}_h^n)\|_{0,\Sigma}^2 + \frac{\gamma_{\mathrm{p}}h^2\tau}{\mu}\|\nabla p_h^n\|_{0,\Omega^{\mathrm{f}}}^2.$$

As a result, Algorithm 2.3 is unconditionally unstable in the energy norm.

Proof. The same calculations as the previous section can be repeated on Algorithm 2.3. In this case, the coupling condition (2.18) becomes

$$\boldsymbol{u}_h^n = \dot{\boldsymbol{d}}_h^{n-\frac{1}{2}} + \frac{1}{\alpha}(\boldsymbol{\lambda}_h^{n-1} - \boldsymbol{\lambda}_h^n) + (\dot{\boldsymbol{d}}_h^{n-\frac{3}{2}} - \dot{\boldsymbol{d}}_h^{n-\frac{1}{2}}). \tag{2.29}$$

Following the sames steps, we test the fluid subproblem (2.17) with $(\boldsymbol{v}_h, q_h) = \tau(\boldsymbol{u}_h^n, p_h^n)$ and the solid subproblem (2.19) with $\boldsymbol{\xi}_h = \tau\dot{\boldsymbol{d}}_h^{n-\frac{1}{2}}$. The fluid problem reads exactly as previously, while the solid one now becomes:

$$\rho^{\mathrm{s}} \int_{\Omega^{\mathrm{s}}} \partial_\tau \dot{\boldsymbol{d}}_h^n \cdot \tau\dot{\boldsymbol{d}}_h^{n-\frac{1}{2}} + a^{\mathrm{s}}(\boldsymbol{d}_h^{n-\frac{1}{2}}, \tau\dot{\boldsymbol{d}}_h^{n-\frac{1}{2}}) = -\int_\Sigma \boldsymbol{\lambda}_h^n \cdot \tau\dot{\boldsymbol{d}}_h^{n-\frac{1}{2}}.$$

The first integral is

$$\rho^{\mathrm{s}} \int_{\Omega^{\mathrm{s}}} \partial_\tau \dot{\boldsymbol{d}}_h^n \cdot \tau\dot{\boldsymbol{d}}_h^{n-\frac{1}{2}} = \frac{\rho^{\mathrm{s}}}{2}\|\dot{\boldsymbol{d}}_h^n\|_{0,\Omega^{\mathrm{s}}}^2 - \frac{\rho^{\mathrm{s}}}{2}\|\dot{\boldsymbol{d}}_h^{n-1}\|_{0,\Omega^{\mathrm{s}}}^2.$$

On the other hand, the bilinear form of the solid becomes

$$a^{\mathrm{s}}(\boldsymbol{d}_h^{n-\frac{1}{2}}, \dot{\boldsymbol{d}}_h^{n-\frac{1}{2}}) = \frac{1}{2}a^{\mathrm{s}}(\boldsymbol{d}_h^n, \boldsymbol{d}_h^n) - \frac{1}{2}a^{\mathrm{s}}(\boldsymbol{d}_h^{n-1}, \boldsymbol{d}_h^{n-1}).$$

Then summing the two equations

$$\begin{aligned}\frac{\rho^{\mathrm{f}}}{2}\|\boldsymbol{u}_h^n\|_{0,\Omega^{\mathrm{f}}}^2 + \frac{\rho^{\mathrm{s}}}{2}\|\dot{\boldsymbol{d}}_h^n\|_{0,\Omega^{\mathrm{s}}}^2 + \frac{\rho^{\mathrm{f}}}{2}\|\boldsymbol{u}_h^n - \boldsymbol{u}_h^{n-1}\|_{0,\Omega^{\mathrm{f}}}^2 + 2\tau\mu\|\boldsymbol{\epsilon}(\boldsymbol{u}_h^n)\|_{0,\Omega^{\mathrm{f}}}^2 + \frac{1}{2}\|\boldsymbol{d}_h^n\|_{\mathrm{s}}^2 + \frac{\gamma_{\mathrm{p}}h^2\tau}{\mu}\|\nabla p_h^n\|_{0,\Omega^{\mathrm{f}}}^2 \\ = \frac{\rho^{\mathrm{f}}}{2}\|\boldsymbol{u}_h^{n-1}\|_{0,\Omega^{\mathrm{f}}}^2 + \frac{\rho^{\mathrm{s}}}{2}\|\dot{\boldsymbol{d}}_h^{n-1}\|_{0,\Omega^{\mathrm{s}}}^2 + \frac{1}{2}\|\boldsymbol{d}_h^{n-1}\|_{\mathrm{s}}^2 + \int_\Sigma \tau\boldsymbol{\lambda}_h^n \cdot (\boldsymbol{u}_h^n - \dot{\boldsymbol{d}}_h^{n-\frac{1}{2}}),\end{aligned}$$

where the only term remaining to be bounded is

$$T := \tau\int_\Sigma \boldsymbol{\lambda}_h^n \cdot (\boldsymbol{u}_h^n - \dot{\boldsymbol{d}}_h^{n-\frac{1}{2}}).$$

Using (2.29) and (2.23), we can estimate T as

$$\begin{aligned}T &= \tau\int_\Sigma \boldsymbol{\lambda}_h^n \cdot \left[\frac{1}{\alpha}(\boldsymbol{\lambda}_h^{n-1} - \boldsymbol{\lambda}_h^n) + (\dot{\boldsymbol{d}}_h^{n-\frac{3}{2}} - \dot{\boldsymbol{d}}_h^{n-\frac{1}{2}})\right] \\ &= \frac{\tau}{2\alpha}\left(\|\boldsymbol{\lambda}_h^{n-1}\|_{0,\Sigma}^2 - \|\boldsymbol{\lambda}_h^n\|_{0,\Sigma}^2 - \|\boldsymbol{\lambda}_h^n - \boldsymbol{\lambda}_h^{n-1}\|_{0,\Sigma}^2\right) + \tau\int_\Sigma \boldsymbol{\lambda}_h^n \cdot (\dot{\boldsymbol{d}}_h^{n-\frac{3}{2}} - \dot{\boldsymbol{d}}_h^{n-\frac{1}{2}}).\end{aligned}$$

The last integral can be estimated using the Cauchy-Schwarz inequality and the discrete

trace inequality (2.24) as before:

$$\tau \int_\Sigma \boldsymbol{\lambda}_h^n \cdot (\dot{\boldsymbol{d}}_h^{n-\frac{3}{2}} - \dot{\boldsymbol{d}}_h^{n-\frac{1}{2}}) \geq -\frac{2\alpha C_{\mathrm{T}}^2}{h\rho^{\mathrm{s}}} \frac{\tau}{2\alpha} \|\boldsymbol{\lambda}_h^n\|_{0,\Sigma}^2 - \frac{\rho^{\mathrm{s}}}{4} \|\dot{\boldsymbol{d}}_h^{n-\frac{3}{2}} - \dot{\boldsymbol{d}}_h^{n-\frac{1}{2}}\|_{0,\Omega^{\mathrm{s}}}^2.$$

Summing all the terms over $m = 1, \ldots, n$, we obtain the estimate. □

Notice that, differently than Algorithm 2.2, the perturbation introduced by the coupling condition (2.29) is not controlled by the dissipation term in the solid subproblem, indeed the term $\|\dot{\boldsymbol{d}}_h^{n-\frac{3}{2}} - \dot{\boldsymbol{d}}_h^{n-\frac{1}{2}}\|_{0,\Omega^{\mathrm{s}}}^2$ cannot be bounded by any other term on the left-hand side. As a result, Algorithm 2.3 is unconditionally unstable in the energy norm.

3 | An alternative strategy: the Neumann-Robin scheme

Contents

In this chapter, we investigate an alternative coupling strategy: the Neumann-Robin scheme, which peculiarity is that it reverses the roles of the interface conditions. We will replicate the energy stability analysis done in the previous chapter, which will show that this alternative choice is conditionally stable both for BDF1 and MD time schemes.

3.1. Motivations and formulations of the scheme

Normally, the Robin-Neumann scheme associates the Robin condition to the fluid and the Neumann condition to the solid. This choice directly reflects the nature of the problem: the solid is assigned a Neumann condition in order to balance the stresses exerted by the fluid, while the fluid is assigned a Robin condition in order to mitigate the added mass effect.

Although this choice seems the most natural, we want to answer the following questions: how is the stability affected when the coupling conditions are reversed? Therefore, we propose an alternative coupling strategy by reversing the roles of the interface conditions: we apply a Neumann condition to the fluid and a Robin condition to the solid, creating a Neumann-Robin scheme (NR). This reversal changes the information exchange between the two subdomains and may impact the numerical properties of the scheme, such as stability, accuracy, and energy conservation. Although this scheme might seem counterintuitive, given that the Neumann-Dirichlet is proven to be unconditionally unstable,

applying the Robin condition on the fluid introduces a dissipation on the solid velocities as shown in the previous chapter. In the reversed setting, imposing the Robin condition on the solid is expected to produce an additional dissipative effect, analogous to viscous damping, on the fluid velocities (measured by $\|\boldsymbol{u}^n - \boldsymbol{u}^{n-1}\|$). Consequently, this mechanism allows us to control the energy dissipation more effectively, even for the choice of mid-point scheme, leading to a conditional stable scheme.

To analyze this setup, we firstly derive the variational formulation corresponding to this reversed coupling strategy. Taking $(\boldsymbol{\xi}, \boldsymbol{v}, q) \in \boldsymbol{V}^{\mathrm{s}} \times \boldsymbol{V}^{\mathrm{f}} \times M^{\mathrm{f}}$ test functions, the variational formulation of problem (2.1) reads: find $\boldsymbol{u}(t) \in \boldsymbol{V}^{\mathrm{f}}$, $p(t) \in M^{\mathrm{f}}$, $\boldsymbol{d}(t) \in \boldsymbol{V}^{\mathrm{s}}$ and $\dot{\boldsymbol{d}}(t) \in \boldsymbol{V}^{\mathrm{s}}$ such that

$$\rho^{\mathrm{s}} \int_{\Omega^{\mathrm{s}}} \partial_t \dot{\boldsymbol{d}} \cdot \boldsymbol{\xi} + a^{\mathrm{s}}(\boldsymbol{d}, \boldsymbol{\xi}) - \int_{\Sigma} \boldsymbol{\lambda} \cdot \boldsymbol{\xi} = 0,$$
$$\rho^{\mathrm{f}} \int_{\Omega^{\mathrm{f}}} \partial_t \boldsymbol{u} \cdot \boldsymbol{v} + a^{\mathrm{f}}((\boldsymbol{u}, p), (\boldsymbol{v}, q)) + \int_{\Sigma} \boldsymbol{\lambda} \cdot \boldsymbol{v} = 0,$$

for all $(\boldsymbol{\xi}, \boldsymbol{v}, q) \in \boldsymbol{V}^{\mathrm{s}} \times \boldsymbol{V}^{\mathrm{f}} \times M^{\mathrm{f}}$. Note that this variational formulation differs from (2.5) in the sign of the integrals on the interface Σ, since here we associate with $\boldsymbol{\lambda} = \boldsymbol{\sigma}^{\mathrm{s}}(\boldsymbol{d})\boldsymbol{n}^{\mathrm{s}} (= \boldsymbol{\sigma}^{\mathrm{f}}(\boldsymbol{u}, p)\boldsymbol{n}^{\mathrm{f}}) \in \boldsymbol{L}^2(\Sigma)$ the solid stresses and not the fluid stresses anymore.

The time discretization of the coupling condition can be expressed using a BDF1 scheme or a mid-point scheme as follows:

$$\text{BDF1:} \quad \begin{cases} \boldsymbol{\sigma}^{\mathrm{f}}(\boldsymbol{u}^n, p^n)\boldsymbol{n}^{\mathrm{f}} = -\boldsymbol{\lambda}^{n-1} \\ \boldsymbol{\lambda}^n + \alpha \dot{\boldsymbol{d}}^n = \alpha \boldsymbol{u}^{n-1} + \boldsymbol{\lambda}^{n-1} \end{cases} \quad \text{on } \Sigma,$$

$$\text{Mid-point:} \quad \begin{cases} \boldsymbol{\sigma}^{\mathrm{f}}(\boldsymbol{u}^n, p^n)\boldsymbol{n}^{\mathrm{f}} = -\boldsymbol{\lambda}^{n-\frac{1}{2}} \\ \boldsymbol{\lambda}^{n-\frac{1}{2}} + \alpha \dot{\boldsymbol{d}}^{n-\frac{1}{2}} = \alpha \boldsymbol{u}^{n-1} + \boldsymbol{\lambda}^{n-\frac{3}{2}} \end{cases} \quad \text{on } \Sigma.$$

Again, this choice of time discretization only influences the solid coupling, while the fluid is always solved with a BDF1 scheme.

The fully discrete formulation of this problem is detailed in Algorithm 3.1 when we use BDF1 for the solid, and in Algorithm 3.2 when we use the mid-point scheme for the solid. Moreover, both of these algorithms can be modified to include correction iterations (see Appendix B for details).

Although the scheme is named Neumann-Robin, which might suggests that the fluid subproblem with Neumann condition is solved first, the actual procedure starts with solving the solid subproblem with the Robin condition. This choice is justified by the stability analysis, whose key step consists in writing the algorithms as numerical perturbation of

the strongly coupled counterpart. In order to do so, in the solid-stress updates, we must always have that $\boldsymbol{u}$ and $\dot{\boldsymbol{d}}$ are taken at different time instances.

3.2. Energy stability analysis

The purpose of this section is to analyze the energy stability of the algorithms presented above. We will show that LC-RN-BDF1 and LC-RN-MD are both conditionally energy stable.

3.2.1. Stability for the LC-NR-BDF1 scheme

Starting with LC-RN-BDF1, the energy stability result is stated in the following theorem.

Theorem 3.1. *Let* $\{(\boldsymbol{u}_h^n, p_h^n, \boldsymbol{d}_h^n, \dot{\boldsymbol{d}}_h^n, \boldsymbol{\lambda}_h^n)\}_{n\geq 1}$ *be given by Algorithm 3.1. Assuming that*

$$\tau < \delta_h^{-1} := \frac{\rho^{\mathrm{f}} h}{2\alpha C_{\mathrm{T}}^2}, \tag{3.7}$$

the following energy estimates hold, for $n \geq 1$ *and* $n\tau \leq T$*:*

$$E_h^n + \sum_{m=1}^{n} G_h^m \leq \exp\left(\frac{\delta_h T}{1-\tau\delta_h}\right) E_h^0,$$

where

$$\begin{aligned} E_h^n &:= \frac{\rho^{\mathrm{f}}}{2}\|\boldsymbol{u}_h^n\|_{0,\Omega^{\mathrm{f}}}^2 + \frac{\rho^{\mathrm{s}}}{2}\|\dot{\boldsymbol{d}}_h^n\|_{0,\Omega^{\mathrm{s}}}^2 + \frac{1}{2}\|\boldsymbol{d}_h^n\|_{\mathrm{s}}^2 + \frac{\tau}{2\alpha}\|\boldsymbol{\lambda}_h^n\|_{0,\Sigma}^2, \\ G_h^n &:= \frac{\rho^{\mathrm{s}}}{2}\|\dot{\boldsymbol{d}}_h^n - \dot{\boldsymbol{d}}_h^{n-1}\|_{0,\Omega^{\mathrm{s}}}^2 + \frac{\rho^{\mathrm{f}}}{4}\|\boldsymbol{u}_h^n - \boldsymbol{u}_h^{n-1}\|_{0,\Omega^{\mathrm{f}}}^2 + 2\tau\mu\|\boldsymbol{\epsilon}(\boldsymbol{u}_h^n)\|_{0,\Omega^{\mathrm{f}}}^2 \\ &\quad + \frac{\tau\alpha}{2}\|\boldsymbol{u}_h^{n-1} - \dot{\boldsymbol{d}}_h^n\|_{0,\Sigma}^2 + \frac{1}{2}\|\boldsymbol{d}_h^n - \boldsymbol{d}_h^{n-1}\|_{\mathrm{s}}^2 + \frac{\gamma_{\mathrm{p}} h^2 \tau}{\mu}\|\nabla p_h^n\|_{0,\Omega^{\mathrm{f}}}^2. \end{aligned}$$

Proof. We proceed as in the proof of Theorem 2.1. We first show that Algorithm 3.1 can be seen as a numerical perturbation of its strongly coupled counterpart thanks to the kinematic perturbation condition obtained from (3.8):

$$\dot{\boldsymbol{d}}_h^n = \boldsymbol{u}_h^n + \frac{1}{\alpha}(\boldsymbol{\lambda}_h^{n-1} - \boldsymbol{\lambda}_h^n) + (\boldsymbol{u}_h^{n-1} - \boldsymbol{u}_h^n), \tag{3.8}$$

which now is the perturbation of the fluid velocity $\boldsymbol{u}_h^n$, instead of the solid velocity $\dot{\boldsymbol{d}}_h^n$.

Algorithm 3.1 Loosely coupled scheme with Neumann-Robin interface conditions and BDF1 time discretization (LC-NR-BDF1)

Given $\boldsymbol{u}_h^0, \boldsymbol{d}_h^0, \dot{\boldsymbol{d}}_h^0, \boldsymbol{\lambda}_h^0$ and α, $\forall n \geq 1$:

1. Solid subproblem: find $\boldsymbol{d}_h^n$, $\dot{\boldsymbol{d}}_h^n \in \boldsymbol{V}_h^{\mathrm{s}}$, such that $\dot{\boldsymbol{d}}_h^n = \partial_\tau \boldsymbol{d}_h^n$ and

$$\rho^{\mathrm{s}} \int_{\Omega^{\mathrm{s}}} \partial_\tau \dot{\boldsymbol{d}}_h^n \cdot \boldsymbol{\xi}_h + a^{\mathrm{s}}(\boldsymbol{d}_h^n, \boldsymbol{\xi}_h) + \alpha \int_\Sigma (\dot{\boldsymbol{d}}_h^n - \boldsymbol{u}_h^{n-1}) \cdot \boldsymbol{\xi}_h = \int_\Sigma \boldsymbol{\lambda}_h^{n-1} \cdot \boldsymbol{\xi}_h \tag{3.1}$$

   for all $\boldsymbol{\xi}_h \in \boldsymbol{V}_h^{\mathrm{s}}$.

2. Solid-stress update: set $\boldsymbol{\lambda}_h^n \in \boldsymbol{V}_h^{\mathrm{g}}$ as

$$\boldsymbol{\lambda}_h^n = \boldsymbol{\lambda}_h^{n-1} + \alpha(\boldsymbol{u}_h^{n-1} - \dot{\boldsymbol{d}}_h^n) \quad \text{on } \Sigma. \tag{3.2}$$

3. Fluid subproblem: find $(\boldsymbol{u}_h^n, p_h^n) \in \boldsymbol{V}_h^{\mathrm{f}} \times M_h^{\mathrm{f}}$ such that

$$\rho^{\mathrm{f}} \int_{\Omega^{\mathrm{f}}} \partial_\tau \boldsymbol{u}_h^n \cdot \boldsymbol{v}_h + a_h^{\mathrm{f}}((\boldsymbol{u}_h^n, p_h^n), (\boldsymbol{v}_h, q_h)) = -\int_\Sigma \boldsymbol{\lambda}_h^n \cdot \boldsymbol{v}_h \tag{3.3}$$

   for all $(\boldsymbol{v}_h, q_h) \in \boldsymbol{V}_h^{\mathrm{f}} \times M_h^{\mathrm{f}}$.

Algorithm 3.2 Loosely coupled scheme with Neumann-Robin interface conditions and mid-point time discretization (LC-NR-MD)

Given $\boldsymbol{u}_h^0, \boldsymbol{d}_h^0, \dot{\boldsymbol{d}}_h^0, \boldsymbol{\lambda}_h^0$, and α, $\forall n \geq 1$:

1. Solid subproblem: find $\boldsymbol{d}_h^n$, $\dot{\boldsymbol{d}}_h^n \in \boldsymbol{V}_h^{\mathrm{s}}$, such that $\dot{\boldsymbol{d}}_h^{n-\frac{1}{2}} = \partial_\tau \boldsymbol{d}_h^n$ and

$$\rho^{\mathrm{s}} \int_{\Omega^{\mathrm{s}}} \partial_\tau \dot{\boldsymbol{d}}_h^n \cdot \boldsymbol{\xi}_h + a^{\mathrm{s}}(\boldsymbol{d}_h^{n-\frac{1}{2}}, \boldsymbol{\xi}_h) + \alpha \int_\Sigma (\dot{\boldsymbol{d}}_h^{n-\frac{1}{2}} - \boldsymbol{u}_h^{n-1}) \cdot \boldsymbol{\xi}_h = \int_\Sigma \boldsymbol{\lambda}_h^{n-\frac{3}{2}} \cdot \boldsymbol{\xi}_h \tag{3.4}$$

   for all $\boldsymbol{\xi}_h \in \boldsymbol{V}_h^{\mathrm{s}}$.

2. Solid-stress update: set $\boldsymbol{\lambda}_h^{n-\frac{1}{2}} \in \boldsymbol{V}_h^{\mathrm{g}}$ as

$$\boldsymbol{\lambda}_h^{n-\frac{1}{2}} = \boldsymbol{\lambda}_h^{n-\frac{3}{2}} + \alpha(\boldsymbol{u}_h^{n-1} - \dot{\boldsymbol{d}}_h^{n-\frac{1}{2}}) \quad \text{on } \Sigma. \tag{3.5}$$

3. Fluid subproblem: find $(\boldsymbol{u}_h^n, p_h^n) \in \boldsymbol{V}_h^{\mathrm{f}} \times M_h^{\mathrm{f}}$ such that

$$\rho^{\mathrm{f}} \int_{\Omega^{\mathrm{f}}} \partial_\tau \boldsymbol{u}_h^n \cdot \boldsymbol{v}_h + a_h^{\mathrm{f}}((\boldsymbol{u}_h^n, p_h^n), (\boldsymbol{v}_h, q_h)) = -\int_\Sigma \boldsymbol{\lambda}_h^{n-\frac{1}{2}} \cdot \boldsymbol{v}_h \tag{3.6}$$

   for all $(\boldsymbol{v}_h, q_h) \in \boldsymbol{V}_h^{\mathrm{f}} \times M_h^{\mathrm{f}}$.

After combining (3.1) with (3.2), we proceed testing with $\boldsymbol{\xi}_h = \tau \dot{\boldsymbol{d}}_h^n$ the solid subproblem, which reads

$$\rho^{\mathrm{s}} \tau \int_{\Omega^{\mathrm{s}}} \partial_\tau \dot{\boldsymbol{d}}_h^n \cdot \dot{\boldsymbol{d}}_h^n + \tau a^{\mathrm{s}}(\boldsymbol{d}_h^n, \dot{\boldsymbol{d}}_h^n) = \tau \int_\Sigma \boldsymbol{\lambda}_h^n \cdot \dot{\boldsymbol{d}}_h^n.$$

We can use (2.23) to rewrite the first and second term as

$$\begin{aligned}\frac{\rho^{\mathrm{s}}}{2}\|\dot{\boldsymbol{d}}_h^n\|_{0,\Omega^{\mathrm{s}}}^2 + \frac{\rho^{\mathrm{s}}}{2}\|\dot{\boldsymbol{d}}_h^n - \dot{\boldsymbol{d}}_h^{n-1}\|_{0,\Omega^{\mathrm{s}}}^2 + \frac{1}{2}\|\boldsymbol{d}_h^n\|_{\mathrm{s}}^2 + \frac{1}{2}\|\boldsymbol{d}_h^n - \boldsymbol{d}_h^{n-1}\|_{\mathrm{s}}^2 \\ = \frac{\rho^{\mathrm{s}}}{2}\|\dot{\boldsymbol{d}}_h^{n-1}\|_{0,\Omega^{\mathrm{s}}}^2 + \frac{1}{2}\|\boldsymbol{d}_h^n\|_{\mathrm{s}}^2 + \tau \int_\Sigma \boldsymbol{\lambda}_h^n \cdot \dot{\boldsymbol{d}}_h^n.\end{aligned}$$

Similartly, the fluid subproblem (3.3), is tested with $(\boldsymbol{v}_h, q_h) = \tau(\boldsymbol{u}_h^n, p_h^n)$, yielding

$$\rho^{\mathrm{f}} \tau \int_{\Omega^{\mathrm{f}}} \partial_\tau \boldsymbol{u}_h^n \cdot \boldsymbol{u}_h^n + \tau a_h^{\mathrm{f}}((\boldsymbol{u}_h^n, p_h^n), (\boldsymbol{u}_h^n, p_h^n)) = -\tau \int_\Sigma \boldsymbol{\lambda}_h^n \cdot \boldsymbol{u}_h^n.$$

Using (2.23) again, we obtain

$$\begin{aligned}\frac{\rho^{\mathrm{f}}}{2}\|\boldsymbol{u}_h^n\|_{0,\Omega^{\mathrm{f}}}^2 + \frac{\rho^{\mathrm{f}}}{2}\|\boldsymbol{u}_h^n - \boldsymbol{u}_h^{n-1}\|_{0,\Omega^{\mathrm{f}}}^2 + 2\tau\mu\|\boldsymbol{\epsilon}(\boldsymbol{u}_h^n)\|_{0,\Omega^{\mathrm{f}}}^2 + \frac{\gamma_{\mathrm{p}} h^2 \tau}{\mu}\|\nabla p_h^n\|_{0,\Omega^{\mathrm{f}}}^2 \\ = \frac{\rho^{\mathrm{f}}}{2}\|\boldsymbol{u}_h^{n-1}\|_{0,\Omega^{\mathrm{f}}}^2 - \tau \int_\Sigma \boldsymbol{\lambda}_h^n \cdot \boldsymbol{u}_h^n.\end{aligned}$$

Summing the two equations, the only term that remains to be bounded is

$$T_1 := \tau \int_\Sigma \boldsymbol{\lambda}_h^n \cdot (\dot{\boldsymbol{d}}_h^n - \boldsymbol{u}_h^n).$$

As in the proof of Theorem 2.1 we can use (3.8) to rewrite this term in order to obtain a telescopic sum, as:

$$T_1 = \underbrace{\tau \int_\Sigma \boldsymbol{\lambda}_h^n \cdot \frac{1}{\alpha}(\boldsymbol{\lambda}_h^{n-1} - \boldsymbol{\lambda}_h^n)}_{T_2} \underbrace{+\tau \int_\Sigma \boldsymbol{\lambda}_h^n \cdot (\boldsymbol{u}_h^{n-1} - \boldsymbol{u}_h^n)}_{T_3}.$$

The first term can be estimated using (2.23):

$$T_2 = \frac{\tau}{2\alpha}\left(\|\boldsymbol{\lambda}_h^{n-1}\|_{0,\Sigma}^2 - \|\boldsymbol{\lambda}_h^n\|_{0,\Sigma}^2 - \|\boldsymbol{\lambda}_h^n - \boldsymbol{\lambda}_h^{n-1}\|_{0,\Sigma}^2\right).$$

The second term can be estimated using the Cauchy-Schwarz inequality and the discrete

trace inequality [6]:

$$\begin{aligned} T_3 &\geq -\tau C_{\mathrm{T}} h^{-\frac{1}{2}} \|\boldsymbol{\lambda}_h^n\|_{0,\Sigma} \|\boldsymbol{u}_h^{n-1} - \boldsymbol{u}_h^n\|_{0,\Omega^{\mathrm{f}}} \\ &\geq -\underbrace{\frac{2\alpha C_{\mathrm{T}}^2}{h\rho^{\mathrm{f}}}}_{:=\delta_h} \frac{\tau^2}{2\alpha} \|\boldsymbol{\lambda}_h^n\|_{0,\Sigma}^2 - \frac{\rho^{\mathrm{f}}}{4} \|\boldsymbol{u}_h^{n-1} - \boldsymbol{u}_h^n\|_{0,\Omega^{\mathrm{f}}}^2. \end{aligned}$$

Summing all the terms over $m = 1, \ldots, n$, we reach the following estimate:

$$E_h^n + \sum_{m=1}^{n} G_h^m \leq E_h^0 + \sum_{m=1}^{n} \delta_h \frac{\tau^2}{2\alpha} \|\boldsymbol{\lambda}_h^m\|_{0,\Sigma}^2 \leq E_h^0 + \tau \sum_{m=1}^{n} \delta_h E_h^m.$$

Applying Lemma 2.1 as in the proof of Theorem 2.1, we obtain the thesis. □

This theorem is analogous to Theorem 2.1 and its proof follows the same steps. The only difference is that the result now depends on the numerical dissipation of the fluid, i.e. on the quantity $\|\boldsymbol{u}^n - \boldsymbol{u}^{n-1}\|_{0,\Omega^{\mathrm{f}}}$.

3.2.2. Stability for the LC-NR-MD scheme

Regarding the mid-point scheme, the result is analogous and it is formally stated by the following theorem.

Theorem 3.2. *Let $\{(\boldsymbol{u}_h^n, p_h^n, \boldsymbol{d}_h^n, \dot{\boldsymbol{d}}_h^n, \boldsymbol{\lambda}_h^n)\}_{n\geq 1}$ be given by Algorithm 3.2. Assuming that*

$$\tau < \delta_h^{-1} := \frac{\rho^{\mathrm{f}} h}{2\alpha C_{\mathrm{T}}^2}, \tag{3.9}$$

the following energy estimates hold, for $n \geq 1$ and $n\tau \leq T$:

$$E_h^n + \sum_{m=1}^{n} G_h^m \leq \exp\left(\frac{\delta_h T}{1 - \tau\delta_h}\right) E_h^0,$$

where

$$\begin{aligned} E_h^n &:= \frac{\rho^{\mathrm{f}}}{2} \|\boldsymbol{u}_h^n\|_{0,\Omega^{\mathrm{f}}}^2 + \frac{\rho^{\mathrm{s}}}{2} \|\dot{\boldsymbol{d}}_h^n\|_{0,\Omega^{\mathrm{s}}}^2 + \frac{1}{2} \|\boldsymbol{d}_h^n\|_{\mathrm{s}}^2 + \frac{\tau}{2\alpha} \|\boldsymbol{\lambda}_h^{n-\frac{1}{2}}\|_{0,\Sigma}^2, \\ G_h^n &:= \frac{\rho^{\mathrm{f}}}{2} \|\boldsymbol{u}_h^n - \boldsymbol{u}_h^{n-1}\|_{0,\Omega^{\mathrm{f}}}^2 + 2\tau\mu \|\boldsymbol{\epsilon}(\boldsymbol{u}_h^n)\|_{0,\Omega^{\mathrm{f}}}^2 + \frac{\gamma_{\mathrm{p}} h^2 \tau}{\mu} \|\nabla p_h^n\|_{0,\Omega^{\mathrm{f}}}^2 + \frac{\tau}{2\alpha} \|\boldsymbol{\lambda}_h^{n-\frac{1}{2}} - \boldsymbol{\lambda}_h^{n-\frac{3}{2}}\|_{0,\Sigma}^2. \end{aligned}$$

Proof. In this case, the coupling condition (3.10) simply remains

$$\dot{\boldsymbol{d}}_h^{n-\frac{1}{2}} = \boldsymbol{u}_h^n + \frac{1}{\alpha}(\boldsymbol{\lambda}_h^{n-\frac{3}{2}} - \boldsymbol{\lambda}_h^{n-\frac{1}{2}}) + (\boldsymbol{u}_h^{n-1} - \boldsymbol{u}_h^n). \tag{3.10}$$

The solid subproblem (3.4) is tested with $\boldsymbol{\xi}_h = \tau \dot{\boldsymbol{d}}_h^{n-\frac{1}{2}}$ and reads

$$\rho^{\mathrm{s}}\tau \int_{\Omega^{\mathrm{s}}} \partial_\tau \dot{\boldsymbol{d}}_h^n \cdot \dot{\boldsymbol{d}}_h^{n-\frac{1}{2}} + \tau a^{\mathrm{s}}(\boldsymbol{d}_h^{n-\frac{1}{2}}, \dot{\boldsymbol{d}}_h^{n-\frac{1}{2}}) = \tau \int_\Sigma \boldsymbol{\lambda}_h^{n-\frac{1}{2}} \cdot \dot{\boldsymbol{d}}_h^{n-\frac{1}{2}},$$

which yields

$$\frac{\rho^{\mathrm{s}}}{2}\|\dot{\boldsymbol{d}}_h^n\|_{0,\Omega^{\mathrm{s}}}^2 + \frac{1}{2}\|\boldsymbol{d}_h^n\|_{\mathrm{s}}^2 = \frac{\rho^{\mathrm{s}}}{2}\|\dot{\boldsymbol{d}}_h^{n-1}\|_{0,\Omega^{\mathrm{s}}}^2 + \frac{1}{2}\|\boldsymbol{d}_h^{n-1}\|_{\mathrm{s}}^2 + \tau \int_\Sigma \boldsymbol{\lambda}_h^{n-\frac{1}{2}} \cdot \dot{\boldsymbol{d}}_h^{n-\frac{1}{2}}.$$

On the other hand, the fluid subproblem (3.6) is tested with $(\boldsymbol{v}_h, p_h) = \tau(\boldsymbol{u}_h^n, p_h^n)$ and reads

$$\frac{\rho^{\mathrm{f}}}{2}\|\boldsymbol{u}_h^n\|_{0,\Omega^{\mathrm{f}}}^2 + \frac{\rho^{\mathrm{f}}}{2}\|\boldsymbol{u}_h^n - \boldsymbol{u}_h^{n-1}\|_{0,\Omega^{\mathrm{f}}}^2 + 2\tau\mu\|\boldsymbol{\epsilon}(\boldsymbol{u}_h^n)\|_{0,\Omega^{\mathrm{f}}}^2 + \frac{\gamma_{\mathrm{p}} h^2 \tau}{\mu}\|\nabla p_h^n\|_{0,\Omega^{\mathrm{f}}}^2 = \frac{\rho^{\mathrm{f}}}{2}\|\boldsymbol{u}_h^{n-1}\|_{0,\Omega^{\mathrm{f}}}^2 - \tau \int_\Sigma \boldsymbol{\lambda}_h^{n-\frac{1}{2}} \cdot \boldsymbol{u}_h^n.$$

Summing the two equations, the only term that remains to be bounded is

$$T_1 := \tau \int_\Sigma \boldsymbol{\lambda}_h^{n-\frac{1}{2}} \cdot (\dot{\boldsymbol{d}}_h^{n-\frac{1}{2}} - \boldsymbol{u}_h^n).$$

Using (3.10), we can rewrite this term as

$$T_1 = \tau \int_\Sigma \boldsymbol{\lambda}_h^{n-\frac{1}{2}} \cdot \frac{1}{\alpha}(\boldsymbol{\lambda}_h^{n-\frac{3}{2}} - \boldsymbol{\lambda}_h^{n-\frac{1}{2}}) - \tau \int_\Sigma \boldsymbol{\lambda}_h^{n-\frac{1}{2}} \cdot (\boldsymbol{u}_h^{n-1} - \boldsymbol{u}_h^n).$$

For the first term we have

$$T_1 \leq \frac{\tau}{2\alpha}\left(\|\boldsymbol{\lambda}_h^{n-\frac{3}{2}}\|_{0,\Sigma}^2 - \|\boldsymbol{\lambda}_h^{n-\frac{1}{2}}\|_{0,\Sigma}^2 - \|\boldsymbol{\lambda}_h^{n-\frac{1}{2}} - \boldsymbol{\lambda}_h^{n-\frac{3}{2}}\|_{0,\Sigma}^2\right).$$

On the second term, we apply Cauchy-Schwartz inequality, the discrete trace inequality and Young's inequality to obtain:

$$T_2 \geq -\frac{2\alpha C_{\mathrm{T}}^2}{h\rho^{\mathrm{f}}}\frac{\tau^2}{2\alpha}\|\boldsymbol{\lambda}_h^{n-\frac{1}{2}}\|_{0,\Sigma}^2 - \frac{\rho^{\mathrm{f}}}{4}\|\boldsymbol{u}_h^{n-1} - \boldsymbol{u}_h^n\|_{0,\Omega^{\mathrm{f}}}^2.$$

Summing everything together over $m = 1, \dots, n$, we obtain the following estimate:

$$E_h^n + \sum_{m=1}^{n} G_h^m \leq E_h^0 + \sum_{m=1}^{n} \delta_h \frac{\tau^2}{2\alpha} \|\boldsymbol{\lambda}_h^{m-\frac{1}{2}}\|_{0,\Sigma}^2.$$

Applying Lemma 2.1, we obtain the thesis. □

Differently from the standard Robin-Neumann mid-point case (Algorithm 2.3), where we obtained an unconditional instability result, we have just reached conditional stability under a CFL-like condition.

4 | Convergence analysis

Contents

This chapter aims at providing the convergence analysis of the Robin-Neumann loosely coupled scheme as presented in Algorithm 2.2. As a preliminary step, we discuss the convergence analysis in a more simple setting, for instance considering the heat equation (see also [58]). Then, the same strategy will be applied onto the LC-RN-BDF1 scheme.

4.1. Convergence analysis for a parabolic PDE

Given a final time $T > 0$, let's consider the following problem on a general domain Ω, where we denote with $\partial\Omega$ the boundary:

$$\begin{cases} \partial_t u - \Delta u = f & \text{in } \Omega \times (0,T), \\ u = 0 & \text{on } \partial\Omega \times (0,T), \\ u_0 = u(0) & \text{in } \Omega. \end{cases}$$

The weak formulation of the problem reads:

$$\text{Find } u \in V = H_0^1(\Omega) \text{ s.t. } \int_\Omega \partial_t uv + \underbrace{\int_\Omega \nabla u \cdot \nabla v}_{:=a(u,v)} = \underbrace{\int_\Omega fv}_{:=b(v)} \quad \forall v \in V, \tag{4.1}$$

with $a(u,v)$ is a symmetric and coercive bilinear form, with coercivity constant κ. Then, let us introduce a finite element triangulation $\mathcal{T}_h$ of Ω. Define the discrete spaces $V_h \subset V$

such that $\dim V_h < \infty$. The semi-discrete formulation reads

$$\text{Find } u_h \in V_h \text{ s.t. } \int_\Omega \partial_t u_h v_h + \int_\Omega \nabla u_h \cdot \nabla v_h = \int_\Omega f v_h, \quad \forall v_h \in V_h.$$

Now, given a time interval τ, let us define $t_n = n\tau, n \in \mathbb{N}$, and the approximation of the solution $u_h^n \simeq u_h(t_n)$. We employ a backward difference approximation for the time derivative, i.e. the fully discrete formulation becomes

$$\text{Find } u_h^n \in V_h \text{ s.t. } \int_\Omega \partial_\tau u_h^n v_h + \int_\Omega \nabla u_h^n \cdot \nabla v_h = \int_\Omega f(t_n) v_h, \quad \forall v_h \in V_h. \tag{4.2}$$

The goal is to estimate the error $\|u_h^n - u^n\| L^2(\Omega)$. To this end, we will decompose the error into two components: the interpolation error e_Π^n and the discrete error e_h^n. We will first analyze the discrete error, and then apply standard interpolation estimates to bound the interpolation error, which together yield an estimate for the total error.

From (4.1), approximate the solution u in time, test with $v = v_h$ and sum on both sides the derivative approximation:

$$\int_\Omega \partial_\tau u^n v_h + \int_\Omega \nabla u^n \nabla v_h = \int_\Omega f(t_n) v_h + \underbrace{\int_\Omega \left(\partial_\tau u^n - \partial_t u^n\right) v_h}_{:= T^n(v_h)}, \quad \forall v_h \in V_h, \tag{4.3}$$

where the term $T^n(v_h)$ represents the truncation error. We can define the orthogonal projection operator [48] $\Pi_h : V \to V_h$: $\forall w \in V, a(\Pi_h w - w, v_h) = 0, \forall v_h \in V_h$. Then we introduce the error term

$$\begin{aligned} e^n &:= u_h^n - u^n = e_\Pi^n + e_h^n, \\ e_\Pi^n &:= \Pi_h u^n - u^n, \qquad \text{(interpolation error)}, \\ e_h^n &:= u_h^n - \Pi_h u^n, \qquad \text{(discrete error)}. \end{aligned} \tag{4.4}$$

By subtracting (4.3) from (4.2) and assuming that the formulation is initialized with $u_h^0 = \Pi_h u_0$, which immediately yields $e_h^0 = 0$, we obtain:

$$\int_\Omega \partial_\tau e^n v_h + a(e^n, v_h) = T^n(v_h), \quad \forall v_h \in V_h$$

and by expanding the error as in (4.4) we get:

$$\int_\Omega \partial_\tau e_h^n v_h + a(e_h^n, v_h) = T^n(v_h) - \int_\Omega \partial_\tau e_\Pi^n v_h - a(e_\Pi^n, v_h), \quad \forall v_h \in V_h. \tag{4.5}$$

Now test (4.5) with $v_h = e_h^n$:

$$\int_\Omega \partial_\tau e_h^n e_h^n + a(e_h^n, e_h^n) = T^n(e_h^n) - \underbrace{\int_\Omega \partial_\tau e_\Pi^n e_h^n}_{T_1} - \underbrace{a(e_\Pi^n, e_h^n)}_{T_2}.$$

Using the identity (2.23) on the left-hand side, we can rewrite the above relation as

$$\frac{1}{2}\|e_h^n\|_{0,\Omega}^2 + \frac{1}{2}\|e_h^n - e_h^{n-1}\|_{0,\Omega}^2 + \tau\|\nabla e_h^n\|_{0,\Omega}^2 = \frac{1}{2}\|e_h^{n-1}\|_{0,\Omega}^2,$$

where we denote $\|\cdot\|_{0,\Omega} = \|\cdot\|_{L^2(\Omega)}$. Then we sum over $m = 1, \dots, n$ and recall that $e_h^0 = 0$:

$$\frac{1}{2}\|e_h^n\|_{0,\Omega}^2 + \tau\sum_{m=1}^n \|\nabla e_h^m\|_{0,\Omega}^2 \leq \tau\sum_{m=1}^n T^m(e_h^m) - \tau\sum_{m=1}^n T_1(e_h^m) - \tau\sum_{m=1}^n T_2(e_h^m).$$

We proceed by estimating the terms on the right hand side. Recall the Taylor's formula with remainder in integral form [52]:

$$u^n = u^{n-1} + \tau\partial_t u(t_n) + \int_{t_{n-1}}^{t^n} (t_{n-1} - s)\partial_{tt} u(s) ds. \tag{4.6}$$

We can use this formula to estimate the truncation error $T^m(e_h^m)$, indeed, in our case, we can express the difference $\partial_\tau u^m - \partial_t u^m$ as

$$\partial_\tau u^m - \partial_t u^m = \frac{1}{\tau}(u^m - u^{m-1} - \tau\partial_t u^m) = \frac{1}{\tau}\int_{t_{m-1}}^{t_m} (t_{m-1} - s)\partial_{tt} u(s) ds.$$

Taking the $L^2(\Omega)$ norm of this quantity, using the triangle inequality and the fact that $|t_{m-1} - s| \leq \tau$ in the interval $[t_{m-1}, t_m]$:

$$\|\partial_\tau u^m - \partial_t u^m\| = \|\frac{1}{\tau}\int_{t_{m-1}}^{t_m} (t_{m-1} - s)\partial_{tt} u(s) ds\|_{0,\Omega} \leq \int_{t_{m-1}}^{t_m} \|\partial_{tt} u(s)\|_{0,\Omega} ds.$$

Then, using Cauchy-Schwarz, we estimate:

$$\|\partial_\tau u^m - \partial_t u^m\| = \left(\int_{t_{m-1}}^{t_m} 1\, ds\right)^{\frac{1}{2}} \left(\int_{t_{m-1}}^{t_m} \|\partial_{tt} u(s)\|_{0,\Omega}^2\, ds\right)^{\frac{1}{2}} = \tau^{\frac{1}{2}}\|\partial_{tt} u\|_{L^2(t_{m-1}, t_m; L^2(\Omega))}.$$

Substituting this into $T^m(e_h^m)$ and applying Cauchy-Schwarz inequality, we obtain

$$\tau\sum_{m=1}^n T^m(e_h^m) \leq \tau\sum_{m=1}^n \|\partial_{tt} u\|_{L^2(t_{m-1}, t_m; L^2(\Omega))}\tau^{\frac{1}{2}}\|e_h^m\|_{0,\Omega},$$

on which we apply Young's inequality

$$\tau \sum_{m=1}^{n} T^m(e_h^m) \leq \frac{\tau^2}{2\epsilon} \|\partial_{tt} u^n\|^2_{L^2(0,t_n,L^2(\Omega))} + \frac{\epsilon\tau}{2} \sum_{m=1}^{n} \|e_h^m\|^2_{0,\Omega}.$$

Lastly, we can use the Poincaré inequality [48] to bound the $L^2(\Omega)$ norm of the error:

$$\tau \sum_{m=1}^{n} T^m(e_h^m) \leq \frac{\tau^2}{2\epsilon} \|\partial_{tt} u^n\|^2_{L^2(0,t_n,L^2(\Omega))} + \frac{C_{\mathrm{P}}\epsilon\tau}{2} \sum_{m=1}^{n} \|\nabla e_h^m\|^2_{0,\Omega}.$$

For the term T_1, we start using Cauchy-Schwarz:

$$\tau \sum_{m=1}^{n} T_1(e_h^m) = \tau \sum_{m=1}^{n} \int_\Omega \frac{e_\Pi^m - e_\Pi^{m-1}}{\tau} \cdot e_h^m \leq \sum_{m=1}^{n} \|e_\Pi^m - e_\Pi^{m-1}\|_{0,\Sigma} \|e_h^m\|_{0,\Sigma}.$$

We proceed estimating the difference $e_\Pi^m - e_\Pi^{m-1}$ using Taylor's formula [52], as did previously for the truncation error:

$$e_\Pi^m - e_\Pi^{m-1} = \int_{t_{m-1}}^{t_m} \partial_t e_\Pi(s) ds.$$

Taking the $L^2(\Omega)$ norm, applying the triangle inequality and the interpolation inequality [48, Theorem 4.5]:

$$\|v - \Pi_h v\|_{0,\Omega} \leq C h^2 \|v\|_{2,\Omega}, \quad \forall v \in H^2(\Omega), \tag{4.7}$$

we obtain:

$$\tau \sum_{m=1}^{n} T_1(e_h^m) \leq \sum_{m=1}^{n} C_1 h^2 \left(\int_{t_{m-1}}^{t_m} \|\partial_t u\|_{H^2} \right) \|e_h^m\|_{L^2}.$$

Lastly, we apply Cauchy-Schwarz, Young's and Poincarè as follows:

$$\begin{aligned}
\tau \sum_{m=1}^{n} T_1(e_h^m) &\leq \sum_{m=1}^{n} C_1 h^2 \|\partial_t u\|^2_{L^2(t_{m-1},t_m;H^2(\Omega))} \tau^{\frac{1}{2}} \|e_h^m\|_{0,\Sigma} \\
&\leq \frac{C_1 h^4}{2\epsilon} \|\partial_t u\|^2_{L^2(0,t_n;H^2(\Omega))} + \frac{\tau\epsilon}{2} \sum_{m=1}^{n} \|e_h^m\|^2_{0,\Sigma} \\
&\leq \frac{C h^4}{2\epsilon} \|\partial_t u\|^2_{L^2(0,t_n;H^2(\Omega))} + \frac{C_{\mathrm{P}}\tau\epsilon}{2} \sum_{m=1}^{n} \|\nabla e_h^m\|^2_{0,\Sigma}.
\end{aligned}$$

Lastly, the term related to T_2 can be bounded using Cauchy-Schwarz, Young's inequality

and interpolation inequality (4.7) as

$$\begin{aligned}\tau\sum_{m=1}^{n}T_2(e_h^m) &\leq \tau\sum_{m=1}^{n}\|\nabla e_\Pi^m\|_{0,\Omega}\|\nabla e_h^m\|_{0,\Omega}\\ &\leq \tau\sum_{m=1}^{n}\left(\frac{\epsilon}{2}\|\nabla e_h^m\|_{0,\Omega}^2+\frac{1}{2\epsilon}\|\nabla e_\Pi^m\|_{0,\Omega}^2\right)\\ &\leq \tau\sum_{m=1}^{n}\left(\frac{\epsilon}{2}\|\nabla e_h^m\|_{0,\Omega}^2+\frac{C_2h^2}{2\epsilon}\|u^m\|_{2,\Omega}^2\right).\end{aligned}$$

Summing all the terms together and choosing ϵ small enough, we are left with:

$$\|e_h^n\|_{0,\Omega}^2+2\tau\sum_{m=1}^{n}\|\nabla e_h^m\|_{0,\Omega}^2\leq\tau^2\|\partial_{tt}u^n\|_{L^2(0,t_n,L^2(\Omega))}^2+Ch^2\tau\sum_{m=1}^{n}\|u^m\|_{\mathcal{C}((0,t_n),H^2(\Omega))}^2,$$

which yields

$$\|e_h^n\|_{0,\Omega}^2+2\tau\sum_{m=1}^{n}\|\nabla e_h^m\|_{0,\Omega}^2\leq C(\tau^2+h^2).$$

The convergence estimate is therefore

$$\|u_h^n-u(t_n)\|_{0,\Omega}+2\tau\kappa\sum_{m=1}^{n}\|u_h^n-u(t_n)\|_{1,\Omega}\leq C(\tau+h).$$

where we have used the coercivity of the bilinear form a. In this estimate, C is a constant not depending on the time step τ and the mesh size h.

4.2. Convergence analysis for LC-RN-BDF1

We now want to extend the convergence analysis to the Robin-Neumann loosely coupled scheme presented in Algorithm 2.2. We will show that the global errors have a linear convergence rate. The proof follows the same steps as in [13, Section 4] and it is structured in two parts: firstly, we establish a sub-optimal estimate in time ($\mathcal{O}(h+\tau^{\frac{1}{2}})$); then, we show how to improve it to an quasi-optimal estimate ($\mathcal{O}(h+\tau\sqrt{1+\log\tau^{-1}})$) by adding some additional assumptions.

4.2.1. Sub-optimal estimate

We present the first part of the proof, which establishes a sub-optimal estimate in time.

Lemma 4.1. *For $1 \le n \le N$, it holds that*

$$\max_{1\le m\le n}\{\mathcal{S}_h^m + \mathcal{E}_h^m\} + \sum_{m=1}^{n}(\mathcal{W}_h^m + \mathcal{Z}_h^m) \le \mathcal{D}_h^n + \sum_{m=1}^{n}\tau\int_\Sigma \boldsymbol{e}_{\boldsymbol{\lambda},h}^m \cdot \boldsymbol{g}_{2,h}^m,$$

where

$$\begin{aligned}
\mathcal{S}_h^n &:= \frac{\rho^{\mathrm{f}}}{2}\|\boldsymbol{e}_{\boldsymbol{u},h}^n\|_{0,\Omega^{\mathrm{f}}}^2 + \frac{\rho^{\mathrm{s}}}{2}\|\boldsymbol{e}_{\dot{\boldsymbol{d}},h}^n\|_{0,\Omega^{\mathrm{s}}}^2 + \frac{1}{2}\|\boldsymbol{e}_{\boldsymbol{d},h}^n\|_{\mathrm{s}}^2,\\
\mathcal{W}_h^n &:= \frac{\rho^{\mathrm{f}}}{2}\|\boldsymbol{e}_{\boldsymbol{u},h}^n - \boldsymbol{e}_{\boldsymbol{u},h}^{n-1}\|_{0,\Omega^{\mathrm{f}}}^2 + 2\mu\tau\|\boldsymbol{\epsilon}(\boldsymbol{e}_{\boldsymbol{u},h}^n)\|_{0,\Omega^{\mathrm{f}}}^2 + \tau\frac{\gamma_p h^2}{\mu}\|\nabla e_{p,h}^n\|_{0,\Omega^{\mathrm{f}}}^2,\\
&\qquad + \frac{1}{2}\|\boldsymbol{e}_{\boldsymbol{d},h}^n - \boldsymbol{e}_{\boldsymbol{d},h}^{n-1}\|_{\mathrm{s}}^2 + \frac{\rho^{\mathrm{s}}}{4}\|\boldsymbol{e}_{\dot{\boldsymbol{d}},h}^n - \boldsymbol{e}_{\dot{\boldsymbol{d}},h}^{n-1}\|_{0,\Omega^{\mathrm{s}}}^2,\\
\mathcal{E}_h^n &:= \frac{\tau}{2\alpha}\|\boldsymbol{e}_{\boldsymbol{\lambda},h}^n\|_{0,\Sigma}^2,\\
\mathcal{Z}_h^n &:= \frac{\tau}{2\alpha}\|\boldsymbol{e}_{\boldsymbol{\lambda},h}^{n-1} - \boldsymbol{e}_{\boldsymbol{\lambda},h}^n\|_{0,\Sigma}^2,\\
\mathcal{D}_h^n &:= \|\boldsymbol{e}_{\boldsymbol{d},\Pi}^n\|_{\mathrm{s}}^2 + \tau\sum_{m=1}^{n}\Big[T\|R_h^s(\dot{\boldsymbol{d}}^n - \partial_\tau \boldsymbol{d}^n)\|_{\mathrm{s}}^2 + \rho^{\mathrm{f}}T\|\partial_t\boldsymbol{u}^m - \partial_\tau R_h^f\boldsymbol{u}^m\|_{0,\Omega^{\mathrm{f}}}^2\\
&\quad + \mu\|\boldsymbol{\epsilon}(\boldsymbol{e}_{\boldsymbol{u},\Pi}^m)\|_{0,\Omega^{\mathrm{f}}}^2 + \frac{1}{\mu}\|e_{p,\Pi}^m\|_{0,\Omega^{\mathrm{f}}}^2 + \frac{\mu}{h^2}\|\boldsymbol{e}_{\boldsymbol{u},\Pi}^m\|_{0,\Omega^{\mathrm{f}}}^2 + \frac{\mu}{h^2}\|\boldsymbol{e}_{\boldsymbol{u},\Pi}^m\|_{0,\Sigma}^2\\
&\quad + \frac{h^2}{\mu}\|\nabla S_h p^m\|_{0,\Omega^{\mathrm{f}}}^2 + \rho^s T\|\partial_t\dot{\boldsymbol{d}}^m - \partial_\tau R_h^s\dot{\boldsymbol{d}}^m\|_{0,\Omega^{\mathrm{s}}}^2 + T\|\boldsymbol{e}_{\boldsymbol{d},\Pi}^m\|_{\mathrm{s}}^2 + \frac{1}{\alpha}\|\boldsymbol{g}_{2,h}^n\|_{0,\Sigma}^2\Big].
\end{aligned}$$

Proof. We start by introducing the notation for the errors:

$$\begin{aligned}
&\boldsymbol{e}_{\boldsymbol{d}}^n := \boldsymbol{d}_h^n - \boldsymbol{d}^n = \boldsymbol{e}_{\boldsymbol{d},h}^n + \boldsymbol{e}_{\boldsymbol{d},\Pi}^n, && \boldsymbol{e}_{\boldsymbol{d},h}^n := \boldsymbol{d}_h^n - R_h^{\mathrm{s}}\boldsymbol{d}^n, && \boldsymbol{e}_{\boldsymbol{d},\Pi}^n := R_h^{\mathrm{s}}\boldsymbol{d}^n - \boldsymbol{d}^n,\\
&\boldsymbol{e}_{\dot{\boldsymbol{d}}}^n := \dot{\boldsymbol{d}}_h^n - \dot{\boldsymbol{d}}^n = \boldsymbol{e}_{\dot{\boldsymbol{d}},h}^n + \boldsymbol{e}_{\dot{\boldsymbol{d}},\Pi}^n, && \boldsymbol{e}_{\dot{\boldsymbol{d}},h}^n := \dot{\boldsymbol{d}}_h^n - R_h^{\mathrm{s}}\dot{\boldsymbol{d}}^n, && \boldsymbol{e}_{\dot{\boldsymbol{d}},\Pi}^n := R_h^{\mathrm{s}}\dot{\boldsymbol{d}}^n - \dot{\boldsymbol{d}}^n,\\
&\boldsymbol{e}_{\boldsymbol{u}}^n := \boldsymbol{u}_h^n - \boldsymbol{u}^n = \boldsymbol{e}_{\boldsymbol{u},h}^n + \boldsymbol{e}_{\boldsymbol{u},\Pi}^n, && \boldsymbol{e}_{\boldsymbol{u},h}^n := \boldsymbol{u}_h^n - R_h^{\mathrm{f}}\boldsymbol{u}^n, && \boldsymbol{e}_{\boldsymbol{u},\Pi}^n := R_h^{\mathrm{f}}\boldsymbol{u}^n - \boldsymbol{u}^n,\\
&e_p^n := p_h^n - p^n = e_{p,h}^n + e_{p,\Pi}^n, && e_{p,h}^n := p_h^n - S_h p^n, && e_{p,\Pi}^n := S_h p^n - p^n,\\
&\boldsymbol{e}_{\boldsymbol{\lambda}}^n := \boldsymbol{\lambda}_h^n - \boldsymbol{\lambda}^n = \boldsymbol{e}_{\boldsymbol{\lambda},h}^n + \boldsymbol{e}_{\boldsymbol{\lambda},\Pi}^n, && \boldsymbol{e}_{\boldsymbol{\lambda},h}^n := \boldsymbol{\lambda}_h^n - \pi_h\boldsymbol{\lambda}^n, && \boldsymbol{e}_{\boldsymbol{\lambda},\Pi}^n := \pi_h\boldsymbol{\lambda}^n - \boldsymbol{\lambda}^n,
\end{aligned} \tag{4.8}$$

where R_h^{f} and R_h^{s} denote the Scott-Zhang interpolation operators [53], which map onto the finite element spaces $\boldsymbol{V}_h^{\mathrm{f}}$ and $\boldsymbol{V}_h^{\mathrm{s}}$, respectively. The use of the Scott-Zhang interpolants is justified by their flexibility in the choice of degrees of freedom, which is particularly advantageous in our setting. In our formulation, the interpolants R_h^{f} and R_h^{s} are constructed to be consistent across the interface between the subdomains. The operator S_h refers to an interpolation on the space M_h^{f}, modified by a constant to ensure that its mean value over Ω^{f} is zero, necessary to have uniqueness for the pressure. For these interpolants,

there holds the following properties:

$$\begin{aligned}\|R_h^i \boldsymbol{v}\|_{H^1(\Omega^i)} &\leq C\|\boldsymbol{v}\|_{H^1(\Omega^i)}, \quad \text{for } \boldsymbol{v} \in \boldsymbol{H}^1(\Omega^i), \text{ for } i \in \{\mathrm{f}, \mathrm{s}\},\\ \|S_h v\|_{H^1(\Omega^{\mathrm{f}})} &\leq C\|v\|_{H^1(\Omega^{\mathrm{f}})}, \quad \text{for } v \in H^1(\Omega^{\mathrm{f}}).\end{aligned}$$

For projections onto the space $\boldsymbol{V}_h^{\mathrm{g}}$, we denote by π_h the L^2-orthogonal projection from $\boldsymbol{L}^2(\Sigma)$ onto $\boldsymbol{V}_h^{\mathrm{g}}$.

Furthermore, assume that Algorithm 2.2 is initialized with the following conditions:

$$\boldsymbol{d}_h^0 = R_h^{\mathrm{s}} \boldsymbol{d}^0, \qquad \dot{\boldsymbol{d}}_h^0 = R_h^{\mathrm{s}} \dot{\boldsymbol{d}}^0, \qquad \boldsymbol{u}_h^0 = R_h^{\mathrm{f}} \boldsymbol{u}^0, \qquad \boldsymbol{\lambda}_h^0 = \pi_h \boldsymbol{\lambda}^0,$$

immediately yielding

$$\boldsymbol{e}_{\boldsymbol{d},h}^0 = \boldsymbol{0}, \qquad \boldsymbol{e}_{\dot{\boldsymbol{d}},h}^0 = \boldsymbol{0}, \qquad \boldsymbol{e}_{\boldsymbol{u},h}^0 = \boldsymbol{0}, \qquad \boldsymbol{e}_{\boldsymbol{\lambda},h}^0 = \boldsymbol{0}. \tag{4.9}$$

As in the stability proofs of the previous sections, the first passage is to write the error counterpart of (2.22), which is:

$$\boldsymbol{e}_{\boldsymbol{u}}^n = \boldsymbol{e}_{\dot{\boldsymbol{d}}}^n + \frac{1}{\alpha}(\boldsymbol{e}_{\boldsymbol{\lambda}}^{n-1} - \boldsymbol{e}_{\boldsymbol{\lambda}}^n) + (\boldsymbol{e}_{\dot{\boldsymbol{d}}}^{n-1} - \boldsymbol{e}_{\dot{\boldsymbol{d}}}^n).$$

Then, using the definitions of the errors (4.8) and the fact $\dot{\boldsymbol{d}}^n|_\Sigma = \boldsymbol{u}^n|_\Sigma$, which yields $R_h^{\mathrm{s}} \dot{\boldsymbol{d}}^n = R_h^{\mathrm{f}} \boldsymbol{u}^n$ on Σ, we get

$$\begin{aligned}\boldsymbol{e}_{\boldsymbol{u},h}^n - \boldsymbol{e}_{\dot{\boldsymbol{d}},h}^n = \frac{1}{\alpha}(\boldsymbol{e}_{\boldsymbol{\lambda},h}^{n-1} - \boldsymbol{e}_{\boldsymbol{\lambda},h}^n) + (\boldsymbol{e}_{\dot{\boldsymbol{d}},h}^{n-1} - \boldsymbol{e}_{\dot{\boldsymbol{d}},h}^n)\\ + \underbrace{\frac{1}{\alpha}\pi_h(\boldsymbol{\lambda}^{n-1} - \boldsymbol{\lambda}^n) + R_h^{\mathrm{f}}(\boldsymbol{u}^{n-1} - \boldsymbol{u}^n)|_\Sigma}_{:=\boldsymbol{g}_{2,h}^n}.\end{aligned} \tag{4.10}$$

Firstly, we study the fluid subproblem. From (2.5) and using (2.9) it follows that

$$\begin{aligned}\rho^{\mathrm{f}} \int_{\Omega^{\mathrm{f}}} \partial_\tau \boldsymbol{u}^n \cdot \boldsymbol{v}_h + a_h^{\mathrm{f}}((\boldsymbol{u}^n, p^n), (\boldsymbol{v}_h, q_h)) - \int_\Sigma \boldsymbol{\lambda}^n \cdot \boldsymbol{v}_h\\ = \rho^{\mathrm{f}} \int_{\Omega^{\mathrm{f}}} (\partial_\tau \boldsymbol{u}^n - \partial_t \boldsymbol{u}^n) \cdot \boldsymbol{v}_h + \frac{\gamma_{\mathrm{p}} h^2}{\mu} \int_{\Omega^{\mathrm{f}}} \nabla p^n \cdot \nabla q_h\end{aligned}$$

for all $(\boldsymbol{v}_h, q_h) \in \boldsymbol{V}_h^{\mathrm{f}} \times M_h^{\mathrm{f}}$. Subtracting (2.14) from the latter and exploiting the error

definitions (4.8), we get

$$\begin{aligned}\rho^{\mathrm{f}}\int_{\Omega^{\mathrm{f}}}\partial_\tau \boldsymbol{e}^n_{\boldsymbol{u},h}\cdot\boldsymbol{v}_h + a^{\mathrm{f}}_h((\boldsymbol{e}^n_{\boldsymbol{u},h},e^n_{p,h}),(\boldsymbol{v}_h,q_h)) - \int_\Sigma \boldsymbol{e}^n_{\boldsymbol{\lambda},h}\cdot\boldsymbol{v}_h \\ = -\rho^{\mathrm{f}}\int_{\Omega^{\mathrm{f}}}\partial_\tau \boldsymbol{e}^n_{\boldsymbol{u},\Pi}\cdot\boldsymbol{v}_h - a^{\mathrm{f}}_h((\boldsymbol{e}^n_{\boldsymbol{u},\Pi},e^n_{p,\Pi}),(\boldsymbol{v}_h,q_h)) + \int_\Sigma \boldsymbol{e}^n_{\boldsymbol{\lambda},\Pi}\cdot\boldsymbol{v}_h \\ -\rho^{\mathrm{f}}\int_{\Omega^{\mathrm{f}}}(\partial_\tau\boldsymbol{u}^n-\partial_t\boldsymbol{u}^n)\cdot\boldsymbol{v}_h - \frac{\gamma_{\mathrm{p}}h^2}{\mu}\int_{\Omega^{\mathrm{f}}}\nabla p^n\cdot\nabla q_h.\end{aligned}$$

Note that $\int_\Sigma \boldsymbol{e}^n_{\boldsymbol{\lambda},\Pi}\cdot\boldsymbol{v}_h = 0$ since π_h is the L^2 projection onto the space $\boldsymbol{V}^{\mathrm{g}}_h = \mathrm{Tr}\,\boldsymbol{V}_{\mathrm{h}}$, therefore $\boldsymbol{e}^n_{\boldsymbol{\lambda},\Pi}$ is orthogonal to any test function $\boldsymbol{v}_h|_\Sigma \in \boldsymbol{V}_h$. Using (2.9):

$$\begin{aligned}\rho^{\mathrm{f}}\int_{\Omega^{\mathrm{f}}}\partial_\tau \boldsymbol{e}^n_{\boldsymbol{u},h}\cdot\boldsymbol{v}_h + a^{\mathrm{f}}_h((\boldsymbol{e}^n_{\boldsymbol{u},h},e^n_{p,h}),(\boldsymbol{v}_h,q_h)) - \int_\Sigma \boldsymbol{e}^n_{\boldsymbol{\lambda},h}\cdot\boldsymbol{v}_h \\ = -\rho^{\mathrm{f}}\int_{\Omega^{\mathrm{f}}}\partial_\tau \boldsymbol{e}^n_{\boldsymbol{u},\Pi}\cdot\boldsymbol{v}_h - a^{\mathrm{f}}((\boldsymbol{e}^n_{\boldsymbol{u},\Pi},e^n_{p,\Pi}),(\boldsymbol{v}_h,q_h)) - \frac{\gamma_{\mathrm{p}}h^2}{\mu}\int_{\Omega^{\mathrm{f}}}\nabla e^n_{p,\Pi}\cdot\nabla q_h \\ -\rho^{\mathrm{f}}\int_{\Omega^{\mathrm{f}}}(\partial_\tau\boldsymbol{u}^n-\partial_t\boldsymbol{u}^n)\cdot\boldsymbol{v}_h - \frac{\gamma_{\mathrm{p}}h^2}{\mu}\int_{\Omega^{\mathrm{f}}}\nabla p^n\cdot\nabla q_h.\end{aligned}$$

Finally, using the error definitions (4.8) for $\boldsymbol{e}^n_{\boldsymbol{u},\Pi}$ and $e^n_{p,\Pi}$, we reach

$$\begin{aligned}&\rho^{\mathrm{f}}\int_{\Omega^{\mathrm{f}}}\partial_\tau \boldsymbol{e}^n_{\boldsymbol{u},h}\cdot\boldsymbol{v}_h + a^{\mathrm{f}}_h((\boldsymbol{e}^n_{\boldsymbol{u},h},e^n_{p,h}),(\boldsymbol{v}_h,q_h)) - \int_\Sigma \boldsymbol{e}^n_{\boldsymbol{\lambda},h}\cdot\boldsymbol{v}_h \\ &= \underbrace{\rho^{\mathrm{f}}\int_{\Omega^{\mathrm{f}}}(\partial_t\boldsymbol{u}^n-\partial_\tau R^{\mathrm{f}}_h\boldsymbol{u}^n)\cdot\boldsymbol{v}_h}_{T^{\mathrm{f}}_1(\boldsymbol{v}_h,q_h)}\underbrace{-a^{\mathrm{f}}((\boldsymbol{e}^n_{\boldsymbol{u},\Pi},e^n_{p,\Pi}),(\boldsymbol{v}_h,q_h))}_{T^{\mathrm{f}}_2(\boldsymbol{v}_h,q_h)}\underbrace{-\frac{\gamma_{\mathrm{p}}h^2}{\mu}\int_{\Omega^{\mathrm{f}}}\nabla S_h p^n\cdot\nabla q_h}_{T^{\mathrm{f}}_3(\boldsymbol{v}_h,q_h)},\end{aligned}\tag{4.11}$$

where again we have used the fact that $\int_\Sigma \boldsymbol{e}^n_{\boldsymbol{\lambda},\Pi}\cdot\boldsymbol{v}_h = 0$ for all $\boldsymbol{v}_h \in \boldsymbol{V}^{\mathrm{f}}_h$. We can proceed similarly for the solid subproblem: from (2.5) it follows that

$$\rho^{\mathrm{s}}\int_{\Omega^{\mathrm{s}}}\partial_\tau\dot{\boldsymbol{d}}^n\cdot\boldsymbol{\xi}_h + a^{\mathrm{s}}(\boldsymbol{d}^n,\boldsymbol{\xi}_h) = -\int_\Sigma\boldsymbol{\lambda}^n\cdot\boldsymbol{\xi}_h + \rho^{\mathrm{s}}\int_{\Omega^{\mathrm{s}}}(\partial_\tau\dot{\boldsymbol{d}}^n-\partial_t\dot{\boldsymbol{d}}^n)\cdot\boldsymbol{\xi}_h$$

for all $\boldsymbol{\xi}_h \in \boldsymbol{V}^{\mathrm{s}}_h$, so that subtracting (2.16) from this relation and using the error expressions

(4.8), we have

$$\begin{aligned}
&\rho^{\mathrm{s}}\int_{\Omega^{\mathrm{s}}}(\partial_\tau \boldsymbol{e}^n_{\dot{\boldsymbol{d}},h}\cdot\boldsymbol{\xi}_h)+a^{\mathrm{s}}(\boldsymbol{e}^n_{\boldsymbol{d},h},\boldsymbol{\xi}_h)+\int_\Sigma \boldsymbol{e}^n_{\boldsymbol{\lambda},h}\cdot\boldsymbol{\xi}_h\\
&\quad=-\rho^{\mathrm{s}}\int_{\Omega^{\mathrm{s}}}\partial_\tau \boldsymbol{e}^n_{\dot{\boldsymbol{d}},\Pi}\cdot\boldsymbol{\xi}_h-a^{\mathrm{s}}(\boldsymbol{e}^n_{\boldsymbol{d},\Pi},\boldsymbol{\xi}_h)-\int_\Sigma \boldsymbol{e}^n_{\boldsymbol{\lambda},\Pi}\cdot\boldsymbol{\xi}_h-\rho^{\mathrm{s}}\int_{\Omega^{\mathrm{s}}}(\partial_\tau\dot{\boldsymbol{d}}^n-\partial_t\dot{\boldsymbol{d}}^n)\cdot\boldsymbol{\xi}_h\\
&\quad=\underbrace{\rho^{\mathrm{s}}\int_{\Omega^{\mathrm{s}}}(\partial_t\dot{\boldsymbol{d}}^n-\partial_\tau R^{\mathrm{s}}_h\dot{\boldsymbol{d}}^n)\cdot\boldsymbol{\xi}_h}_{T^{\mathrm{s}}_1(\boldsymbol{\xi}_h)}\underbrace{-a^{\mathrm{s}}(\boldsymbol{e}^n_{\boldsymbol{d},\Pi},\boldsymbol{\xi}_h)}_{T^{\mathrm{s}}_2(\boldsymbol{\xi}_h)}.
\end{aligned}\tag{4.12}$$

We can now test the fluid subproblem (4.11) with $(\boldsymbol{v}_h,q_h)=\tau(\boldsymbol{e}^n_{\boldsymbol{u},h},e^n_{p,h})$ to get:

$$\begin{aligned}
&\frac{\rho^{\mathrm{f}}}{2}\|\boldsymbol{e}^n_{\boldsymbol{u},h}\|^2_{0,\Omega^{\mathrm{f}}}+\frac{\rho^{\mathrm{f}}}{2}\|\boldsymbol{e}^n_{\boldsymbol{u},h}-\boldsymbol{e}^{n-1}_{\boldsymbol{u},h}\|^2_{0,\Omega^{\mathrm{f}}}+2\mu\tau\|\boldsymbol{\epsilon}(\boldsymbol{e}^n_{\boldsymbol{u},h})\|^2_{0,\Omega^{\mathrm{f}}}+\tau s_h(e^n_{p,h},e^n_{p,h})\\
&\qquad=\frac{\rho^{\mathrm{f}}}{2}\|\boldsymbol{e}^{n-1}_{\boldsymbol{u},h}\|^2_{0,\Omega^{\mathrm{f}}}+\tau\sum_{i=1}^{3}T^{\mathrm{f}}_i(\boldsymbol{e}^n_{\boldsymbol{u},h},e^n_{p,h})+\tau\int_\Sigma \boldsymbol{e}^n_{\boldsymbol{\lambda},h}\cdot\boldsymbol{e}^n_{\boldsymbol{u},h},
\end{aligned}\tag{4.13}$$

and the solid subproblem (4.12) with $\boldsymbol{\xi}_h=\tau\,\boldsymbol{e}^n_{\dot{\boldsymbol{d}},h}$ to obtain:

$$\begin{aligned}
&\frac{\rho^{\mathrm{s}}}{2}\|\boldsymbol{e}^n_{\dot{\boldsymbol{d}},h}\|^2_{0,\Omega^{\mathrm{s}}}+\frac{\rho^{\mathrm{s}}}{2}\|\boldsymbol{e}^n_{\dot{\boldsymbol{d}},h}-\boldsymbol{e}^{n-1}_{\dot{\boldsymbol{d}},h}\|^2_{0,\Omega^{\mathrm{s}}}+\tau a^{\mathrm{s}}(\boldsymbol{e}^n_{\boldsymbol{d},h},\boldsymbol{e}^n_{\dot{\boldsymbol{d}},h})\\
&\qquad=\frac{\rho^{\mathrm{s}}}{2}\|\boldsymbol{e}^{n-1}_{\dot{\boldsymbol{d}},h}\|^2_{0,\Omega^{\mathrm{s}}}+\tau\sum_{i=1}^{2}T^{\mathrm{s}}_i(\boldsymbol{e}^n_{\dot{\boldsymbol{d}},h})-\tau\int_\Sigma \boldsymbol{e}^n_{\boldsymbol{\lambda},h}\cdot\boldsymbol{e}^n_{\dot{\boldsymbol{d}},h}.
\end{aligned}$$

A key part of the proof consists in showing that the discrete errors (4.8) satisfy Algorithm 2.2 with appropriate perturbations of the right-hand sides. To this purpose, applying the operator ∂_τ to $\boldsymbol{e}^n_{\boldsymbol{d},h}$ and substituting into $\boldsymbol{e}^n_{\dot{\boldsymbol{d}},h}$, we get:

$$\boldsymbol{e}^n_{\dot{\boldsymbol{d}},h}=\partial_\tau \boldsymbol{e}^n_{\boldsymbol{d},h}\underbrace{-R^{\mathrm{s}}_h(\dot{\boldsymbol{d}}^n-\partial_\tau\boldsymbol{d}^n)}_{:=\boldsymbol{g}^n_{1,h}}.\tag{4.14}$$

By using this last relation into the solid elastic term a^{s}, we get:

$$\begin{aligned}
&\frac{\rho^{\mathrm{s}}}{2}\|\boldsymbol{e}^n_{\dot{\boldsymbol{d}},h}\|^2_{0,\Omega^{\mathrm{s}}}+\frac{\rho^{\mathrm{s}}}{2}\|\boldsymbol{e}^n_{\dot{\boldsymbol{d}},h}-\boldsymbol{e}^{n-1}_{\dot{\boldsymbol{d}},h}\|^2_{0,\Omega^{\mathrm{s}}}+\frac{1}{2}\|\boldsymbol{e}^n_{\boldsymbol{d},h}\|^2_{\mathrm{s}}+\frac{1}{2}\|\boldsymbol{e}^n_{\boldsymbol{d},h}-\boldsymbol{e}^{n-1}_{\boldsymbol{d},h}\|^2_{\mathrm{s}}\\
&\quad=\frac{\rho^{\mathrm{s}}}{2}\|\boldsymbol{e}^{n-1}_{\dot{\boldsymbol{d}},h}\|^2_{0,\Omega^{\mathrm{s}}}+\frac{1}{2}\|\boldsymbol{e}^{n-1}_{\boldsymbol{d},h}\|^2_{\mathrm{s}}-\tau a^{\mathrm{s}}(\boldsymbol{e}^n_{\boldsymbol{d},h},\boldsymbol{g}^n_{1,h})+\tau\sum_{i=1}^{2}T^{\mathrm{s}}_i(\boldsymbol{e}^n_{\dot{\boldsymbol{d}},h})-\tau\int_\Sigma \boldsymbol{e}^n_{\boldsymbol{\lambda},h}\cdot\boldsymbol{e}^n_{\dot{\boldsymbol{d}},h}.
\end{aligned}\tag{4.15}$$

After summing the two equations, we define the term

$$\mathcal{R}_h^n := \tau \int_\Sigma \boldsymbol{e}_{\boldsymbol{\lambda},h}^n \cdot (\boldsymbol{e}_{\boldsymbol{u},h}^n - \boldsymbol{e}_{\dot{\boldsymbol{d}},h}^n).$$

This term can be rewritten using relation (4.10) into

$$\begin{aligned}\mathcal{R}_h^n &= \tau \int_\Sigma \boldsymbol{e}_{\boldsymbol{\lambda},h}^n \cdot \left[\frac{1}{\alpha}(\boldsymbol{e}_{\boldsymbol{\lambda},h}^{n-1} - \boldsymbol{e}_{\boldsymbol{\lambda},h}^n) + (\boldsymbol{e}_{\dot{\boldsymbol{d}},h}^{n-1} - \boldsymbol{e}_{\dot{\boldsymbol{d}},h}^n) + \boldsymbol{g}_{2,h}^n\right] \\ &\leq \frac{\tau}{2\alpha}\left(\|\boldsymbol{e}_{\boldsymbol{\lambda},h}^{n-1}\|_{0,\Sigma}^2 - \|\boldsymbol{e}_{\boldsymbol{\lambda},h}^n\|_{0,\Sigma}^2 - \|\boldsymbol{e}_{\boldsymbol{\lambda},h}^{n-1} - \boldsymbol{e}_{\boldsymbol{\lambda},h}^n\|_{0,\Sigma}^2\right) + \frac{2\alpha C_{\mathrm{T}}^2}{h\rho^{\mathrm{s}}}\frac{\tau^2}{2\alpha}\|\boldsymbol{e}_{\boldsymbol{\lambda},h}^n\|_{0,\Sigma}^2 \\ &\quad + \frac{\rho^{\mathrm{s}}}{4}\|\boldsymbol{e}_{\dot{\boldsymbol{d}},h}^{n-1} - \boldsymbol{e}_{\dot{\boldsymbol{d}},h}^n\|_{0,\Omega^{\mathrm{s}}}^2 + \tau \int_\Sigma \boldsymbol{e}_{\boldsymbol{\lambda},h}^n \cdot \boldsymbol{g}_{2,h}^n.\end{aligned}$$

Then, we exploit the perturbation identity (4.14) into the bilinear form $a^{\mathrm{s}}(\boldsymbol{e}_{\boldsymbol{d},h}^n, \boldsymbol{e}_{\dot{\boldsymbol{d}},h}^n)$ and by summing together (4.13) and (4.15), we get

$$\begin{aligned}\mathcal{S}_h^n + \mathcal{W}_h^n + \mathcal{E}_h^n + \mathcal{Z}_h^n = \mathcal{S}_h^{n-1} + \mathcal{E}_h^{n-1} - \tau a^{\mathrm{s}}(\boldsymbol{e}_{\boldsymbol{d},h}^n, \boldsymbol{g}_{1,h}^n) \\ + \tau \sum_{i=1}^{3} T_i^{\mathrm{f}}(\boldsymbol{e}_{\boldsymbol{u},h}^n, e_{p,h}^n) + \tau \sum_{i=1}^{2} T_i^{\mathrm{s}}(\boldsymbol{e}_{\dot{\boldsymbol{d}},h}^n) + \tau \int_\Sigma \boldsymbol{e}_{\boldsymbol{\lambda},h}^n \cdot \boldsymbol{g}_{2,h}^n.\end{aligned}$$

Finally, by summing over $m = 1, \ldots, n$ and noting that $\mathcal{S}_h^n = \mathcal{E}_h^n = 0$ (owning to (4.9)), we have

$$\begin{aligned}\max_{1\leq m\leq n}\{\mathcal{S}_h^m + \mathcal{E}_h^m\} + \sum_{m=1}^{n}(\mathcal{W}_h^m + \mathcal{Z}_h^m) \leq \underbrace{-\sum_{m=1}^{n}\tau a^{\mathrm{s}}(\boldsymbol{e}_{\boldsymbol{d},h}^m, \boldsymbol{g}_{1,h}^m)}_{T_1} + \underbrace{\sum_{m=1}^{n}\tau T_1^{\mathrm{f}}(\boldsymbol{e}_{\boldsymbol{u},h}^m, e_{p,h}^m)}_{T_2} \\ + \underbrace{\sum_{m=1}^{n}\tau T_2^{\mathrm{f}}(\boldsymbol{e}_{\boldsymbol{u},h}^m, e_{p,h}^m)}_{T_3} + \underbrace{\sum_{m=1}^{n}\tau T_3^{\mathrm{f}}(\boldsymbol{e}_{\boldsymbol{u},h}^m, e_{p,h}^m)}_{T_4} + \underbrace{\sum_{m=1}^{n}\tau T_1^{\mathrm{s}}(\boldsymbol{e}_{\dot{\boldsymbol{d}},h}^m)}_{T_5} \\ + \underbrace{\sum_{m=1}^{n}\tau T_2^{\mathrm{s}}(\boldsymbol{e}_{\dot{\boldsymbol{d}},h}^m)}_{T_6} + \sum_{m=1}^{n}\tau\int_\Sigma \boldsymbol{e}_{\boldsymbol{\lambda},h}^m \cdot \boldsymbol{g}_{2,h}^m. \qquad (4.16)\end{aligned}$$

We proceed by bounding each term $T_i, i = 1, \ldots, 6$. In the following calculation, $\epsilon_i, i = 1, \ldots$ will denote generic positive constants independent of the physical and discretization

parameters. For the first term:

$$T_1 \leq \sum_{m=1}^{n} \tau \|\boldsymbol{e}_{\boldsymbol{d},h}^m\|_{\mathrm{s}} \|\boldsymbol{g}_{1,h}^m\|_{\mathrm{s}} \leq \frac{\tau\epsilon_1}{2T} \sum_{m=1}^{n} \|\boldsymbol{e}_{\boldsymbol{d},h}^m\|_{\mathrm{s}}^2 + \frac{2\tau T}{\epsilon_1} \sum_{m=1}^{n} \|\boldsymbol{g}_{1,h}^m\|_{\mathrm{s}}^2$$
$$\leq \epsilon_1 \max_{1\leq m\leq n} \mathcal{S}_h^n + \frac{2\tau T}{\epsilon_1} \sum_{m=1}^{n} \|\boldsymbol{g}_{1,h}^m\|_{\mathrm{s}}^2.$$

For the second term we can apply Young's inequality

$$T_2 \leq \rho^{\mathrm{f}} \frac{\tau\epsilon_2}{2T} \sum_{m=1}^{n} \|\boldsymbol{e}_{\boldsymbol{u},h}^m\|_{0,\Omega^{\mathrm{f}}}^2 + \rho^{\mathrm{f}} \frac{\tau T}{2\epsilon_2} \sum_{m=1}^{n} \|\partial_t \boldsymbol{u}^m - \partial_\tau R_h^{\mathrm{f}} \boldsymbol{u}^m\|_{0,\Omega^{\mathrm{f}}}^2$$
$$\leq \epsilon_2 \max_{1\leq m\leq n} \mathcal{S}_h^n + \rho^{\mathrm{f}} \frac{\tau T}{2\epsilon_2} \sum_{m=1}^{n} \|\partial_t \boldsymbol{u}^m - \partial_\tau R_h^{\mathrm{f}} \boldsymbol{u}^m\|_{0,\Omega^{\mathrm{f}}}^2.$$

For the third term we can use Korn's inequality

$$T_3 = -2\tau\mu \sum_{m=1}^{n} \int_{\Omega^{\mathrm{f}}} \boldsymbol{\epsilon}(\boldsymbol{e}_{\boldsymbol{u},\Pi}^m) : \boldsymbol{\epsilon}(\boldsymbol{e}_{\boldsymbol{u},h}^m) + \tau \sum_{m=1}^{n} \int_{\Omega^{\mathrm{f}}} e_{p,\Pi}^m \mathrm{div}\, \boldsymbol{e}_{\boldsymbol{u},h}^m \underbrace{-\tau \sum_{m=1}^{n} \int_{\Omega^{\mathrm{f}}} e_{p,h}^m \mathrm{div}\, \boldsymbol{e}_{\boldsymbol{u},h}^m}_{T_{3,1}}$$
$$\leq 2(\epsilon_3+\epsilon_4)\tau\mu \sum_{m=1}^{n} \|\boldsymbol{\epsilon}(\boldsymbol{e}_{\boldsymbol{u},h}^m)\|_{0,\Omega^{\mathrm{f}}}^2 + \frac{\tau\mu}{4\epsilon_3} \sum_{m=1}^{n} \|\boldsymbol{\epsilon}(\boldsymbol{e}_{\boldsymbol{u},\Pi}^m)\|_{0,\Omega^{\mathrm{f}}}^2 + \frac{\tau C_K^2}{8\epsilon_4\mu} \sum_{m=1}^{n} \|e_{p,\Pi}^m\|_{0,\Omega^{\mathrm{f}}}^2 + T_{3,1}$$
$$\leq (\epsilon_3+\epsilon_4) \max_{1\leq m\leq n} \mathcal{W}_h^n + \frac{\tau\mu}{4\epsilon_3} \sum_{m=1}^{n} \|\boldsymbol{\epsilon}(\boldsymbol{e}_{\boldsymbol{u},\Pi}^m)\|_{0,\Omega^{\mathrm{f}}}^2 + \frac{\tau C_K^2}{8\epsilon_4\mu} \sum_{m=1}^{n} \|e_{p,\Pi}^m\|_{0,\Omega^{\mathrm{f}}}^2 + T_{3,1}.$$

Let us focus on the term $T_{3,1}$: we proceed by integration by parts and using the trace and Poincaré inequalities on $e_{p,h}^m$ to obtain:

$$T_{3,1} = \tau \sum_{m=1}^{n} \int_{\Omega^{\mathrm{f}}} \boldsymbol{e}_{\boldsymbol{u},\Pi}^m \cdot \nabla e_{p,h}^m - \tau \sum_{m=1}^{n} \int_{\Sigma} e_{p,h}^m \boldsymbol{e}_{\boldsymbol{u},\Pi}^m \cdot \boldsymbol{n}$$
$$\leq \tau\epsilon_5 \frac{\gamma_{\mathrm{p}} h^2}{\mu} \sum_{m=1}^{n} \|\nabla e_{p,h}^m\|_{0,\Omega^{\mathrm{f}}}^2 + \frac{\tau}{4\epsilon_5} \frac{\mu}{\gamma_{\mathrm{p}} h^2} \sum_{m=1}^{n} \|\boldsymbol{e}_{\boldsymbol{u},\Pi}^m\|_{0,\Omega^{\mathrm{f}}}^2 + \tau C_{\mathrm{P}} \sum_{m=1}^{n} \|\nabla e_{p,h}^m\|_{0,\Omega^{\mathrm{f}}}^2 \|\boldsymbol{e}_{\boldsymbol{u},\Pi}^m\|_{0,\Sigma}$$
$$\leq (\epsilon_5+\epsilon_6)\tau \frac{\gamma_{\mathrm{p}} h^2}{\mu} \sum_{m=1}^{n} \|\nabla e_{p,h}^m\|_{0,\Omega^{\mathrm{f}}}^2 + \frac{\tau}{4\epsilon_5} \frac{\mu}{\gamma_{\mathrm{p}} h^2} \sum_{m=1}^{n} \|\boldsymbol{e}_{\boldsymbol{u},\Pi}^m\|_{0,\Omega^{\mathrm{f}}}^2 + \frac{\tau C_{\mathrm{P}}^2}{4\epsilon_6} \frac{\mu}{\gamma_{\mathrm{p}} h^2} \sum_{m=1}^{n} \|\boldsymbol{e}_{\boldsymbol{u},\Pi}^m\|_{0,\Sigma}^2$$
$$\leq (\epsilon_5+\epsilon_6) \max_{1\leq m\leq n} \mathcal{W}_h^n + \frac{\tau}{4\epsilon_5} \frac{\mu}{\gamma_{\mathrm{p}} h^2} \sum_{m=1}^{n} \|\boldsymbol{e}_{\boldsymbol{u},\Pi}^m\|_{0,\Omega^{\mathrm{f}}}^2 + \frac{\tau C_{\mathrm{P}}^2}{4\epsilon_6} \frac{\mu}{\gamma_{\mathrm{p}} h^2} \sum_{m=1}^{n} \|\boldsymbol{e}_{\boldsymbol{u},\Pi}^m\|_{0,\Sigma}^2.$$

For T_4 we can work similarly as T_1, indeed

$$\begin{aligned} T_4 &\leq \tau\epsilon_7 \frac{\gamma_{\mathrm{p}} h^2}{\mu} \sum_{m=1}^{n} \|\nabla e_{p,h}^m\|_{0,\Omega^{\mathrm{f}}}^2 + \frac{\gamma_{\mathrm{p}} h^2}{\mu} \frac{\tau}{4\epsilon_7} \sum_{m=1}^{n} \|\nabla S_h p^m\|_{0,\Omega^{\mathrm{f}}}^2 \\ &\leq \epsilon_7 \max_{1\leq m\leq n} \mathcal{W}_h^n + \frac{\gamma_{\mathrm{p}} h^2}{\mu} \frac{\tau}{4\epsilon_7} \sum_{m=1}^{n} \|\nabla S_h p^m\|_{0,\Omega^{\mathrm{f}}}^2. \end{aligned}$$

For the fifth term we can use again the same argument:

$$\begin{aligned} T_5 &\leq \rho^{\mathrm{s}} \frac{\tau\epsilon_8}{2T} \sum_{m=1}^{n} \|\boldsymbol{e}_{\dot{\boldsymbol{d}},h}^m\|_{0,\Omega^{\mathrm{s}}}^2 + \rho^{\mathrm{s}} \frac{\tau T}{2\epsilon_8} \sum_{m=1}^{n} \|\partial_t \dot{\boldsymbol{d}}^m - \partial_\tau R_h^{\mathrm{f}} \dot{\boldsymbol{d}}^m\|_{0,\Omega^{\mathrm{s}}}^2 \\ &\leq \epsilon_8 \max_{1\leq m\leq n} \mathcal{S}_h^n + \rho^{\mathrm{s}} \frac{\tau T}{2\epsilon_8} \sum_{m=1}^{n} \|\partial_t \dot{\boldsymbol{d}}^m - \partial_\tau R_h^{\mathrm{f}} \dot{\boldsymbol{d}}^m\|_{0,\Omega^{\mathrm{s}}}^2. \end{aligned}$$

For the sixth term, using (4.14), we have:

$$\begin{aligned} T_6 &= \sum_{m=1}^{n} a^{\mathrm{s}}(\boldsymbol{e}_{\boldsymbol{d},\Pi}^m, \boldsymbol{e}_{\boldsymbol{d},h}^m - \boldsymbol{e}_{\boldsymbol{d},h}^{m-1}) + \tau \sum_{m=1}^{n} a^{\mathrm{s}}(\boldsymbol{e}_{\boldsymbol{d},\Pi}^m, \boldsymbol{g}_{1,h}^m) \\ &\leq a^{\mathrm{s}}(\boldsymbol{e}_{\boldsymbol{d},\Pi}^n, \boldsymbol{e}_{\boldsymbol{d},h}^n) - a^{\mathrm{s}}(\boldsymbol{e}_{\boldsymbol{d},\Pi}^0, \boldsymbol{e}_{\boldsymbol{d},h}^0) + \tau \sum_{m=1}^{n} \|\boldsymbol{e}_{\boldsymbol{d},\Pi}^m\|_{\mathrm{s}} \|\boldsymbol{g}_{1,h}^m\|_{\mathrm{s}} \end{aligned}$$

and using and the fact that $\boldsymbol{e}_{\boldsymbol{d},\Pi}^0 = \boldsymbol{e}_{\boldsymbol{d},h}^0 = \boldsymbol{0}$, Cauchy-Schwarz and Young's inequality, we obtain

$$\begin{aligned} T_6 &\leq \|\boldsymbol{e}_{\boldsymbol{d},\Pi}^n\|_{\mathrm{s}} \|\boldsymbol{e}_{\boldsymbol{d},h}^n\|_{\mathrm{s}} + \frac{\tau}{2\epsilon_9} \sum_{m=1}^{n} \|\boldsymbol{e}_{\boldsymbol{d},\Pi}^m\|_{\mathrm{s}}^2 + \frac{\tau\epsilon_9}{2} \sum_{m=1}^{n} \|\boldsymbol{g}_{1,h}^m\|_{\mathrm{s}}^2 \\ &\leq \frac{T}{2\epsilon_9} \|\boldsymbol{e}_{\boldsymbol{d},\Pi}^n\|_{\mathrm{s}}^2 + \frac{\epsilon_9}{2T} \|\boldsymbol{e}_{\boldsymbol{d},h}^n\|_{\mathrm{s}}^2 + \frac{\tau T}{2} \sum_{m=1}^{n} \|\boldsymbol{e}_{\boldsymbol{d},\Pi}^m\|_{\mathrm{s}}^2 + \frac{\tau}{2T} \sum_{m=1}^{n} \|\boldsymbol{g}_{1,h}^m\|_{\mathrm{s}}^2 \\ &\leq \epsilon_9 \max_{1\leq m\leq n} \mathcal{S}_h^n + \frac{T}{2\epsilon_9} \|\boldsymbol{e}_{\boldsymbol{d},\Pi}^n\|_{\mathrm{s}}^2 + \frac{\tau T}{2} \sum_{m=1}^{n} \|\boldsymbol{e}_{\boldsymbol{d},\Pi}^m\|_{\mathrm{s}}^2 + \frac{\tau}{2T} \sum_{m=1}^{n} \|\boldsymbol{g}_{1,h}^m\|_{\mathrm{s}}^2. \end{aligned}$$

Inserting all the previous estimates into (4.16) and supposing that $\epsilon_i, i = 1, \ldots, 9$ are small enough, we obtain the thesis. □

The last term that remains to be bounded, namely,

$$T_7 := \sum_{m=1}^{n} \tau \int_{\Sigma} \boldsymbol{e}_{\boldsymbol{\lambda},h}^m \cdot \boldsymbol{g}_{2,h}^m \tag{4.17}$$

requires special care. Indeed, if we attempt to bound this term with the quantities on the

left-hand side we obtain

$$T_7 \leq \frac{\tau^2}{2\alpha T}\sum_{m=1}^{n}\|\boldsymbol{e}_{\boldsymbol{\lambda},h}^m\|_{0,\Sigma}^2 + \frac{\alpha T}{2}\sum_{m=1}^{n}\|\boldsymbol{g}_{2,h}^m\|_{0,\Sigma}^2.$$

In particular, focusing on $\boldsymbol{g}_{2,h}^m$:

$$\|\boldsymbol{g}_{2,h}^m\|^2 \leq \|\pi_h(\boldsymbol{\lambda}^{m-1}-\boldsymbol{\lambda}^m)\|_{0,\Sigma}^2 + \|R_h^{\mathrm{f}}(\boldsymbol{u}^{m-1}-\boldsymbol{u}^m)\|_{0,\Sigma}^2,$$

where the first term can be bounded as

$$\|\pi_h(\boldsymbol{\lambda}^{m-1}-\boldsymbol{\lambda}^m)\|_{0,\Sigma} \leq \|\boldsymbol{\lambda}^{m-1}-\boldsymbol{\lambda}^m\|_{0,\Sigma} \leq \int_{t_{m-1}}^{t_m}\|\partial_t\boldsymbol{\lambda}\|_{0,\Sigma} = \tau^{\frac{1}{2}}\|\partial_t\boldsymbol{\lambda}\|_{L^2(t_{m-1},t_m;L^2(\Sigma))},$$

while the second term can be bounded using the trace inequality, Poincarè inequality and the H^1 stability of the interpolant R_h^{f}:

$$\begin{aligned}\|R_h^{\mathrm{f}}(\boldsymbol{u}^{m-1}-\boldsymbol{u}^m)\|_{0,\Sigma} &\leq C\|\nabla R_h^{\mathrm{f}}(\boldsymbol{u}^{m-1}-\boldsymbol{u}^m)\|_{L^2(\Omega^{\mathrm{f}})}\\ &\leq C\|\nabla(\boldsymbol{u}^{m-1}-\boldsymbol{u}^m)\|_{L^2(\Omega^{\mathrm{f}})} \leq C\tau^{\frac{1}{2}}\|\partial_t\boldsymbol{u}\|_{L^2(t_{m-1},t_m;L^2(\Omega^{\mathrm{f}}))}.\end{aligned}$$

This ultimately sacrifices a factor of $\tau^{\frac{1}{2}}$ and results in obtaining sub-optimal convergence.

4.2.2. Quasi-optimal estimate

This section aims to present the derivation of an optimal bound for the term (4.17). As done in [13, 20] for the Robin-Robin scheme, the idea is to leverage the error equation of the solid (4.12) to express (4.17) using terms of the domain Ω^{s} only, in order to avoid the interface as much as possible. This requires the construction of an extension of $\boldsymbol{g}_{2,h}^n$ into Ω^{s}, which vanishes on Γ^{s}. To this purpose, we introduce the notation

$$\boldsymbol{g}_{2,h}^n = \underbrace{\frac{1}{\alpha}\pi_h(\boldsymbol{\lambda}^{n-1}-\boldsymbol{\lambda}^n)}_{:=\boldsymbol{g}_{3,h}^n} + \underbrace{R_h^{\mathrm{f}}(\boldsymbol{u}^{n-1}-\boldsymbol{u}^n)|_{\Sigma}}_{:=\boldsymbol{g}_{4,h}^n}. \tag{4.18}$$

Owning to $(2.1)_7$, term $\boldsymbol{g}_{4,h}^n$ can be rewritten as

$$\boldsymbol{g}_{4,h}^n = R_h^{\mathrm{s}}(\dot{\boldsymbol{d}}^{n-1}-\dot{\boldsymbol{d}}^n) \quad \text{on } \Sigma,$$

so that we can simply take

$$\tilde{\boldsymbol{g}}_{4,h}^n := R_h^{\mathrm{s}}(\dot{\boldsymbol{d}}^{n-1}-\dot{\boldsymbol{d}}^n)$$

as extension of $\boldsymbol{g}_{4,h}^n$ onto Ω^s. On the contrary, the term $\boldsymbol{g}_{3,h}^n$ is more delicate. To deal with it, we make two additional assumptions used in [13, 20].

Assumption 4.1. *There exists* $\tilde{\boldsymbol{n}}^s \in [\boldsymbol{W}^{1,\infty}(\Omega^s)]^2$ *such that* $\tilde{\boldsymbol{n}}^s|_\Sigma = \boldsymbol{n}^s$.

This first assumption supposes that there exists an extension $\tilde{\boldsymbol{n}}^s$ of the normal $\boldsymbol{n}^s$ the interface Σ to the solid domain Ω^s, such that its gradient is bounded. It is necessary to introduce this assumption because, in the error proof, it will be required to evaluate the outward facing normal $\boldsymbol{n}^s$ in the interior point of the solid domain, and not just on the interface, where it is naturally defined.

Assumption 4.2. *Assume that* $\tau < \frac{1}{2}$. *There exists a function* $\tilde{\phi} : \Omega^s \to \mathbb{R}$ *satisfying:*

(i) $0 \leq \tilde{\phi} \leq 1$;

(ii) $\tilde{\phi} \in \boldsymbol{V}^s$;

(iii) $|\{\boldsymbol{x} \in \Sigma : \tilde{\phi}(\boldsymbol{x}) \neq 1\}| \leq C\tau$;

(iv) $\|\boldsymbol{\nabla}\tilde{\phi}\|_{0,\Omega^s}^2 \leq C(1 + \log \frac{1}{\tau})$;

where $C > 0$ *is a general constant independent of* τ *and on the physical parameters.*

With the second assumption we introduce an auxiliary function $\tilde{\phi}$ that serves as a pseudo-lifting operator from Σ into Ω^s: it is equal to 1 on the interface and 0 on Γ^s. Relation (iii) allows this cut-off function to go to 0 on Γ^s, while matching the unlifted function on most of Σ. On the other hand, inequality (iv) refers to the smoothness of $\tilde{\phi}$, since it is necessary to control that the gradient does not rapidly transition from 0 to 1 near the interface.

Owning to these assumptions, the goal now is to lift $\boldsymbol{g}_{3,h}^n$ from Σ to Ω^s, using $\boldsymbol{n}^s$ and $\tilde{\phi}$. To this purpose, we define

$$\begin{aligned}
\tilde{\boldsymbol{\ell}}_s &:= \boldsymbol{\sigma}(\boldsymbol{d})\tilde{\boldsymbol{n}}^s, \\
\boldsymbol{\mathcal{L}}_s &:= \tilde{\phi}\tilde{\boldsymbol{\ell}}^s, \\
\tilde{\boldsymbol{g}}_3^n &:= -(\boldsymbol{\mathcal{L}}_s^n - \boldsymbol{\mathcal{L}}_s^{n-1}) = -\tilde{\phi}\boldsymbol{\sigma}(\boldsymbol{d}^n - \boldsymbol{d}^{n-1})\tilde{\boldsymbol{n}}^s, \\
\tilde{\boldsymbol{g}}_{3,h}^n &:= R_h^s \tilde{\boldsymbol{g}}_3^n.
\end{aligned}$$

Therefore, we finally introduce

$$\tilde{\boldsymbol{g}}_{2,h}^n := \tilde{\boldsymbol{g}}_{3,h}^n + \tilde{\boldsymbol{g}}_{4,h}^n. \tag{4.19}$$

Additionally, using Assumptions 4.1 and 4.2, from [20, Lemma 5.2.4], we have the following

estimate

$$\|\tilde{\boldsymbol{g}}^n_{3,h} - \boldsymbol{g}^n_{3,h}\|^2_{0,\Sigma} \leq \tau \|\boldsymbol{g}^n_{3,h}\|^2_{L^\infty(\Sigma)} + h^2 \|\boldsymbol{g}^n_{3,h}\|^2_{1,\Sigma}. \tag{4.20}$$

The introduction of these assumptions yields the following bound:

Lemma 4.2. *Under Assumptions 4.1 and 4.2, for any $\epsilon > 0$, we have*

$$\sum_{m=1}^{n} \tau \int_\Sigma \boldsymbol{e}^m_{\boldsymbol{\lambda},h} \cdot \boldsymbol{g}^m_{2,h} \leq \epsilon \max_{1\leq m\leq n} (\mathcal{E}^m_h + \mathcal{S}^m_h) + \frac{1}{\epsilon} \Psi^n_h,$$

having

$$\begin{aligned}
\Psi^n_h := \frac{\rho^{\mathrm{s}}}{2} \|\tilde{\boldsymbol{g}}^n_{2,h}\|^2_{0,\Omega^{\mathrm{s}}} + \frac{Th^2}{2} \sum_{m=1}^{n} \|\boldsymbol{g}^m_{3,h}\|^2_{1,\Sigma} + \tau \sum_{m=1}^{n} \Big(& \|\boldsymbol{g}^m_{3,h}\|^2_{L^\infty(\Sigma)} \\
& + \rho^{\mathrm{s}} T \tau^2 \|\partial^2_\tau \boldsymbol{\mathcal{L}}^m_{\mathrm{s},h}\|^2_{0,\Omega^{\mathrm{s}}} + \rho^{\mathrm{s}} T \tau^2 \|\partial^2_\tau R^{\mathrm{s}}_h \dot{\boldsymbol{d}}^m\|^2_{0,\Omega^{\mathrm{s}}} + T \|\tilde{\boldsymbol{g}}^m_{2,h}\|^2_{\mathrm{s}} \\
& + \rho^{\mathrm{s}} T \|\partial_t \dot{\boldsymbol{d}}^m - \partial_\tau R^{\mathrm{s}}_h \dot{\boldsymbol{d}}^m\|^2_{0,\Omega^{\mathrm{s}}} + \frac{\rho^{\mathrm{s}}}{T} \|\tilde{\boldsymbol{g}}^m_{2,h}\|^2_{0,\Omega^{\mathrm{s}}} + T \|\boldsymbol{e}^m_{\boldsymbol{d},\Pi}\|^2_{\mathrm{s}} + \frac{1}{T} \|\tilde{\boldsymbol{g}}^m_{2,h}\|^2_{\mathrm{s}} \Big).
\end{aligned}$$

Proof. From (4.18) and owning to (4.19), we can rewrite $\boldsymbol{g}^n_{2,h}$ as

$$\boldsymbol{g}^n_{2,h} = \boldsymbol{g}^n_{3,h} + \tilde{\boldsymbol{g}}^n_{4,h} = \boldsymbol{g}^n_{3,h} + \tilde{\boldsymbol{g}}^n_{2,h} - \tilde{\boldsymbol{g}}^n_{3,h}.$$

Substituting the latter into (4.17), we have

$$T_7 = \tau \sum_{m=1}^{n} \int_\Sigma \boldsymbol{e}^m_{\boldsymbol{\lambda},h} \cdot \boldsymbol{g}^m_{2,h} = \underbrace{\tau \sum_{m=1}^{n} \int_\Sigma \boldsymbol{e}^m_{\boldsymbol{\lambda},h} \cdot (\boldsymbol{g}^m_{3,h} - \tilde{\boldsymbol{g}}^m_{3,h})}_{T_8} \underbrace{+\tau \sum_{m=1}^{n} \int_\Sigma \boldsymbol{e}^m_{\boldsymbol{\lambda},h} \cdot \tilde{\boldsymbol{g}}^m_{2,h}}_{T_9}. \tag{4.21}$$

We now proceed as in [13, 20]. Term T_8 can be bounded using Cauchy-Schwartz and Young's inequality and (4.20) as follows:

$$\begin{aligned}
T_8 &\leq \frac{T}{2\epsilon} \sum_{m=1}^{n} \|\boldsymbol{g}^m_{3,h} - \tilde{\boldsymbol{g}}^m_{3,h}\|^2_{0,\Sigma} + \frac{\epsilon \tau^2}{2T} \sum_{m=1}^{n} \|\boldsymbol{e}^m_{\boldsymbol{\lambda},h}\|^2_{0,\Sigma} \\
&\leq \frac{CT}{2\epsilon} \sum_{m=1}^{n} \left(\tau \|\boldsymbol{g}^m_{3,h}\|^2_{L^\infty(\Sigma)} + h^2 \|\boldsymbol{g}^m_{3,h}\|^2_{1,\Sigma} \right) + \epsilon \max_{1\leq m\leq n} \mathcal{E}^n_h,
\end{aligned}$$

In order to bound term T_9, we test the solid error equation (4.12) with $\boldsymbol{\xi}_h = \tau \tilde{\boldsymbol{g}}^n_{2,h}$ and

sum over $m = 1, \dots, n$, which yields

$$T_9 = \underbrace{\rho^{\mathrm{s}}\tau \sum_{m=1}^{n} \int_{\Omega^{\mathrm{s}}} (\partial_\tau \boldsymbol{e}^m_{\dot{\boldsymbol{d}},h} \cdot \tilde{\boldsymbol{g}}^m_{2,h})}_{T_{9,1}} \underbrace{-\tau \sum_{m=1}^{n} a^{\mathrm{s}}(\boldsymbol{e}^m_{\dot{\boldsymbol{d}},h}, \tilde{\boldsymbol{g}}^m_{2,h})}_{T_{9,2}} \underbrace{-\tau \sum_{m=1}^{n} \sum_{i=1}^{2} T^{\mathrm{s}}_i(\tilde{\boldsymbol{g}}^m_{2,h})}_{T_{9,3}}.$$

As we did previously, we proceed by estimating each term separately. For the first term, we start using summation by parts. For two sequences $\{a^m\}_{m=1}^n$ and $\{b^m\}_{m=1}^n$, the summation by parts formula states: if $a^0 = 0$ and $b^0 = 0$, then

$$\sum_{m=1}^{n} (a^m - a^{m-1}) \cdot b^m = a^n \cdot b^n - \sum_{m=1}^{n} a^{m-1} \cdot (b^m - b^{m-1}).$$

Applying the latter to term $T_{9,1}$ yields

$$T_{9,1} = \sum_{m=1}^{n} \rho^{\mathrm{s}} \int_{\Omega}^{\mathrm{s}} (\boldsymbol{e}^m_{\dot{\boldsymbol{d}},h} - \boldsymbol{e}^{m-1}_{\dot{\boldsymbol{d}},h}) \cdot \tilde{\boldsymbol{g}}^m_{2,h} = \rho^{\mathrm{s}} \int_{\Omega^{\mathrm{s}}} \boldsymbol{e}^n_{\dot{\boldsymbol{d}},h} \cdot \tilde{\boldsymbol{g}}^n_{2,h} - \rho^{\mathrm{s}} \sum_{m=1}^{n} \int_{\Omega^{\mathrm{s}}} \boldsymbol{e}^{m-1}_{\dot{\boldsymbol{d}},h} \cdot (\tilde{\boldsymbol{g}}^m_{2,h} - \tilde{\boldsymbol{g}}^{m-1}_{2,h}).$$

Then, using definition (4.19) we can write the difference $\tilde{\boldsymbol{g}}^m_{2,h} - \tilde{\boldsymbol{g}}^{m-1}_{2,h}$ as

$$\begin{aligned}
\tilde{\boldsymbol{g}}^m_{2,h} - \tilde{\boldsymbol{g}}^{m-1}_{2,h} &= -\tilde{\phi}\boldsymbol{\sigma}(\boldsymbol{d}^m - \boldsymbol{d}^{m-1})\tilde{\boldsymbol{n}}^{\mathrm{s}} + R^{\mathrm{s}}_h(\dot{\boldsymbol{d}}^{m-1} - \dot{\boldsymbol{d}}^m)|_\Sigma \\
&\quad + \tilde{\phi}\boldsymbol{\sigma}(\boldsymbol{d}^{m-1} - \boldsymbol{d}^{m-2})\tilde{\boldsymbol{n}}^{\mathrm{s}} - R^{\mathrm{s}}_h(\dot{\boldsymbol{d}}^{m-2} - \dot{\boldsymbol{d}}^{m-1})|_\Sigma \\
&= -\partial^2_\tau \boldsymbol{\mathcal{L}}^m_{\mathrm{s},h} - \partial^2_\tau R^{\mathrm{s}}_h \dot{\boldsymbol{d}}^m,
\end{aligned}$$

and reasoning as T_8, we have

$$\begin{aligned}
T_{9,1} &\leq 2\epsilon \max_{1\leq m\leq n} \mathcal{S}^m_h + \frac{\rho^{\mathrm{s}}}{2\epsilon} \|\tilde{\boldsymbol{g}}^n_{2,h}\|^2_{0,\Omega^{\mathrm{s}}} + \frac{\rho^{\mathrm{s}} T}{2\tau\epsilon} \sum_{m=1}^{n} \| -\partial^2_\tau \boldsymbol{\mathcal{L}}^m_{\mathrm{s},h} - \partial^2_\tau R^{\mathrm{s}}_h \dot{\boldsymbol{d}}^m\|^2_{0,\Omega^{\mathrm{s}}} \\
&\leq 2\epsilon \max_{1\leq m\leq n} \mathcal{S}^m_h + \frac{\rho^{\mathrm{s}}}{2\epsilon} \|\tilde{\boldsymbol{g}}^n_{2,h}\|^2_{0,\Omega^{\mathrm{s}}} + \rho^{\mathrm{s}} \frac{T\tau^3}{\epsilon} \sum_{m=1}^{n} \|\partial^2_\tau \boldsymbol{\mathcal{L}}^m_{\mathrm{s},h}\|^2_{0,\Omega^{\mathrm{s}}} + \rho^{\mathrm{s}} \frac{T\tau^3}{\epsilon} \|\partial^2_\tau R^{\mathrm{s}}_h \dot{\boldsymbol{d}}^m\|^2_{0,\Omega^{\mathrm{s}}}.
\end{aligned}$$

We proceed similarly for $T_{9,2}$

$$T_{9,2} \leq \frac{\tau\epsilon}{2T} \sum_{m=1}^{n} \|\boldsymbol{e}^m_{\dot{\boldsymbol{d}},h}\|^2_{\mathrm{s}} + \frac{\tau T}{2\epsilon} \sum_{m=1}^{n} \|\tilde{\boldsymbol{g}}^m_{2,h}\|^2_{\mathrm{s}} \leq \epsilon \max_{1\leq m\leq n} \mathcal{S}^m_h + \frac{\tau T}{2\epsilon} \sum_{m=1}^{n} \|\tilde{\boldsymbol{g}}^m_{2,h}\|^2_{\mathrm{s}}.$$

Finally, for the last term, we have

$$\begin{aligned}T_{9,3} &= \sum_{m=1}^{n}\left[\rho^{\mathrm{s}}\int_{\Omega^{\mathrm{s}}}(\partial_t\dot{\boldsymbol{d}}^m-\partial_\tau R_h^{\mathrm{s}}\dot{\boldsymbol{d}}^m)\cdot\tau\tilde{\boldsymbol{g}}_{2,h}^m-a^{\mathrm{s}}(\boldsymbol{e}_{\boldsymbol{d},\Pi}^m,\tau\tilde{\boldsymbol{g}}_{2,h}^m)\right]\\ &\leq \rho^{\mathrm{s}}\frac{\tau T}{2}\sum_{m=1}^{n}\|\partial_t\dot{\boldsymbol{d}}^m-\partial_\tau R_h^{\mathrm{s}}\dot{\boldsymbol{d}}^m\|_{0,\Omega^{\mathrm{s}}}^2+\rho^{\mathrm{s}}\frac{\tau}{2T}\sum_{m=1}^{n}\|\tilde{\boldsymbol{g}}_{2,h}^m\|_{0,\Omega^{\mathrm{s}}}^2+\frac{\tau T}{2}\sum_{m=1}^{n}\|\boldsymbol{e}_{\boldsymbol{d},\Pi}^m\|_{\mathrm{s}}^2\\ &\qquad+\frac{\tau}{2T}\sum_{m=1}^{n}\|\tilde{\boldsymbol{g}}_{2,h}^m\|_{\mathrm{s}}^2.\end{aligned}$$

Inserting the bounds into (4.21), we obtain the thesis. □

The last step is to bound each term in D_h^n and Ψ_h^n in Lemma 4.1 and 4.2. This is done using the approximations properties of R_h^{s} and R_h^{f}. The result reads as follows:

Lemma 4.3. *Under assumptions 4.1 and 4.2, for $1\leq n\leq N$, there follows*

$$D_h^n+\Psi_h^n\leq\tau^2\frac{T(L_1+L_2)^3}{\alpha}\left(1+\log\frac{1}{\tau}\right)\|\dot{\boldsymbol{d}}\|_{L^2(0,T;W^{1,\infty}(\Omega^{\mathrm{s}}))}^2+Y_{\tau,h},$$

where

$$\begin{aligned}Y_{\tau,h}\leq&(L_1+L_2)h^2\|\boldsymbol{d}^n\|_{L^\infty(0,T;H^2(\Omega^{\mathrm{s}}))}^2+\frac{(h^4+\tau^2)(L_1+L_2)^2}{2}\|\boldsymbol{\nabla}\dot{\boldsymbol{d}}\|_{L^2(0,T;H^1(\Omega^{\mathrm{s}}))}^2\\ &+\mu h^2T\|\boldsymbol{u}\|_{L^\infty(0,T;H^2(\Omega^{\mathrm{s}}))}^2+\frac{h^2T}{\mu}\|p\|_{L^\infty(0,T;H^1(\Omega^{\mathrm{f}}))}^2\\ &+T(L_1+L_2)\left(\tau^4\|\partial_t^3\boldsymbol{d}\|_{L^2(0,T;H^1(\Omega^{\mathrm{s}}))}^2+h^2\|\dot{\boldsymbol{d}}\|_{L^2(0,T;H^2(\Omega^{\mathrm{s}}))}^2\right)\\ &+(L_1+L_2)h^2\|\boldsymbol{d}\|_{L^\infty(0,T;H^3(\Omega^{\mathrm{f}}))}^2+\mu Th^2\left(\|\boldsymbol{u}\|_{L^2(0,T;H^2(\Omega^{\mathrm{f}}))}^2+\|\boldsymbol{u}\|_{L^\infty(0,T;H^3(\Omega^{\mathrm{f}}))}^2\right)\\ &+\frac{1}{\alpha}\left(h^2T\|\boldsymbol{u}\|_{L^\infty(0,T;H^3(\Omega^{\mathrm{f}}))}^2+\tau^2\|\partial_t\boldsymbol{u}\|_{L^\infty(0,T;L^2(\Sigma))}^2\right)\\ &+\frac{(L_1+L_2)^2\tau^2}{\alpha}\|\boldsymbol{\nabla}\dot{\boldsymbol{d}}\|_{L^2(0,T;L^2(\Sigma))}^2+\rho^{\mathrm{s}}T\left(\tau^4\|\partial_t^3\dot{\boldsymbol{d}}\|_{L^2(0,T;L^2(\Omega^{\mathrm{s}}))}^2\right.\\ &\left.+h^2\|\partial_t\dot{\boldsymbol{d}}\|_{L^\infty(0,T;H^1(\Omega^{\mathrm{s}}))}^2\right)+\rho^{\mathrm{f}}T\left(\tau^4\|\partial_t^3\boldsymbol{u}\|_{L^2(0,T;L^2(\Omega^{\mathrm{f}}))}^2+h^2\|\partial_t\boldsymbol{u}\|_{L^2(0,T;H^1(\Omega^{\mathrm{f}}))}^2\right)\\ &+\frac{h^2T}{\mu}\|p\|_{L^\infty(0,T;H^1(\Omega^{\mathrm{f}}))}^2+\tau^2(L_1+L_2)^2\|\boldsymbol{\nabla}\dot{\boldsymbol{d}}\|_{L^2(0,T;L^\infty(\Sigma))}^2\\ &+\rho^{\mathrm{s}}T\tau^2\|\partial_t^2\dot{\boldsymbol{d}}\|_{L^2(0,T;L^2(\Omega^{\mathrm{s}}))}^2+\rho^{\mathrm{s}}T\tau^2\|\partial_t^2\boldsymbol{d}\|_{L^2(0,T;H^1(\Omega^{\mathrm{s}}))}^2\\ &+T\tau^2(L_1+L_2)\left(\|\partial_t\dot{\boldsymbol{d}}\|_{L^2(0,T;H^1(\Omega^{\mathrm{s}}))}^2+(L_1+L_2)^2\|\dot{\boldsymbol{d}}\|_{L^2(0,T;H^2(\Omega^{\mathrm{s}}))}^2\right)\\ &+\frac{\rho^{\mathrm{s}}\tau^2}{T}\left(\|\partial_t\dot{\boldsymbol{d}}\|_{L(0,T;L^2(\Omega^{\mathrm{s}}))}^2+(L_1^2+L_2)^2\|\dot{\boldsymbol{d}}\|_{L^2(0,T;H^1(\Omega^{\mathrm{s}}))}^2\right).\end{aligned}$$

A complete proof is provided in [13, Appendix B].

The final error estimates follows by combining all the results stated in Lemmas 4.1–4.3. This establishes a quasi-optimal first-order convergence for the global error in the Robin-Neumann scheme:

Theorem 4.1. *Under Assumptions 4.1 and 4.2, and supposing that* (4.9) *holds, the discrete error is bounded by:*

$$\max_{1\leq m\leq n}\{\mathcal{S}_h^m+\mathcal{E}_h^m\}+\sum_{m=1}^{n}(\mathcal{W}_h^m+\mathcal{Z}_h^m)\leq\tau^2\frac{T(L_1+L_2)^3}{\alpha}\left(1+\log\frac{1}{\tau}\right)\|\dot{\boldsymbol{d}}\|^2_{L^2(0,T;W^{1,\infty}(\Omega^{\mathrm{s}}))}+Y_{\tau,h}.$$

This error bound controls squared terms on the left-hand side by a leading term proportional to $\tau^2(1+\log\tau^{-1})$. Taking the square root on both sides, it leads to an error of order $\mathcal{O}(\tau\sqrt{1+\log\tau^{-1}})$ in time. This is referred to as quasi-optimal since the additional logarithmic factor slightly perturbs the ideal linear rate.

5 | Numerical results

Contents

In this chapter we firstly discuss the optimization of the Robin parameter choice. Then, we present a simple benchmark with the aim of validating the proposed partitioned schemes and theoretical findings reported in the previous chapters. It will highlight the differences between the LC-RN and LC-NR schemes and the choice in time discretization in terms of stability, accuracy and convergence rates, when changing the Robin parameter α, the number of correction iterations and Young's modulus E. The α found heuristically will be compared with the optimal estimates.

5.1. Optimization of the Robin parameter α

Before analyzing the numerical results, a brief digression on how to find the optimal value of the Robin parameter α is needed, as we have not yet discussed it. This section summarizes the main results found in [33].

The study was conducted for a an iterative strongly coupled Robin-Robin scheme, studying separately the optimization of the parameter $\alpha^{\mathrm{f}}_{\mathrm{opt}}$ associated to the fluid Robin condition and parameter $\alpha^{\mathrm{s}}_{\mathrm{opt}}$ associated to the solid Robin one. We will adapt the results to the case of this thesis. It is clear that the Robin-Neumann case is obtained by simply setting and $\alpha = \alpha^{\mathrm{f}}_{\mathrm{opt}}$, and the Neumann-Robin is obtained setting $\alpha = \alpha^{\mathrm{s}}_{\mathrm{opt}}$.

Thanks to Fourier transform, which introduces a new variable k representing the fre-

quency, it is possible to identify the reduction factor

$$\rho^m := \frac{|\hat{p}^m - \hat{p}|}{|\hat{p}^{m-1} - \hat{p}^m|}.$$

This allows to quantify the error at the m-th iteration $\hat{p}^m$ with respect to the exact solution $\hat{p}$. In order to have that the scheme converges, the reduction factor at each iteration must be strictly less than one for all the relevant frequencies of the problem.

The core idea of the optimization procedure is to find the Robin parameters such that the reduction factor is minimized. The optimal fluid coefficient for a potential flow is

$$\alpha^{\mathrm{f}}_{\mathrm{opt}} = \frac{\rho^{\mathrm{s}} H_{\mathrm{s}}}{\Delta t} + \beta H_{\mathrm{s}} \Delta t, \qquad \text{where} \quad \beta = \frac{E}{(1-\nu^2)R^2}. \tag{5.1}$$

This expression separates two contributions: a mass term ($\rho_s H_s/\Delta t$) related to the density effect and time discretization, and a stiffness term ($\beta H_s \Delta t$) related to the structure's elastic stiffness.

It has been shown in [1, 2] that the Robin–Neumann scheme, with parameter $\alpha = \alpha^{\mathrm{f}}_{\mathrm{opt}}$ defined in (5.1), exhibits good performance and is less sensitive to the added mass effect than the Dirichlet–Neumann scheme.

Regarding the solid-side coefficient, the optimization analysis for a potential flow leads to

$$\alpha^{\mathrm{s}}_{\mathrm{opt}} = \frac{2\rho^{\mathrm{f}}}{\tau k_{\max}}, \tag{5.2}$$

where $k_{\max}$ depends on the problem formulation: indeed, in a axisymmetric (radial) formulation, as in [35], when using Bessel functions, the maximum frequency that is possible to reach is $k_{\max} = \frac{R}{h}$, reflecting the resolvable number of radial oscillations within the domain. On the other hand, when working with non-axisymmetric (planar) discretization, the highest frequency is limited by the Nyquist-Shannon criterion [60]: $k < k_{\max} = \frac{\pi}{h}$.

Although the model problem addressed in this thesis is more complex than the one used in [33], (5.1) and (5.2) can nevertheless be employed as approximate estimates to avoid tuning the parameter running multiple simulations changing it every time.

5.2. Numerical setup

Starting from a pre-made code for the Robin-Robin scheme, we have implemented the schemes LC-RN-BDF1, LC-RN-MD, LC-NR-BDF1 and LC-NR-MD (Algorithms 2.2, 2.3,

3.1 and 3.2) in `FreeFem++` on a standard benchmark [28]: we simulated a rectangular tube (Figure 2.1) of dimensions $L = 6$, $R = 0.5$ and $H_s = 0.1$. Moreover, we choose $\rho^f = 1.0$ and $\rho^s = 1.1$, with Lamè coefficients $L_1 = 1.15{\cdot}10^6$ and $L_2 = 1.7{\cdot}10^6$. We also included the transversal membrane effect that appear when the structure is written in axisymmetric form, denoted by the coefficient β. We choose $\beta = 4 \cdot 10^6$ as in [1].

An example of numerical solution with previous parameters is shown in Figure 5.1, which highlights the evolution of the fluid pressure and the solid displacement at different time instances, obtained using the monolithic solver. For illustration purposes, the solid displacement is magnified via a factor 5. The results illustrate the fluid-structure interaction, where the solid displacement is influenced by the fluid pressure, and vice versa.

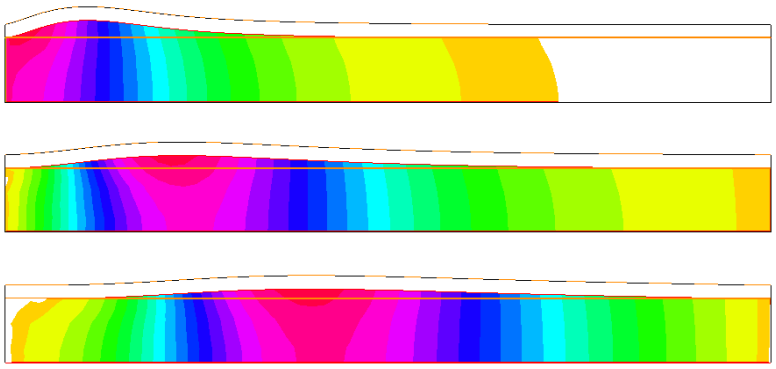

Figure 5.1: Fluid pressure and solid displacement at different time instances (from top to bottom: $t = 1 \cdot 10^{-4}$, $t = 5 \cdot 10^{-4}$, $t = 1 \cdot 10^{-3}$) using MONO-BDF1 (Algorithm 2.1).

In order to check the accuracy of the solution, we firstly computed a reference solution using the monolithic scheme MONO-BDF1 (Algorithm 2.1) on a very fine mesh and with a very fine time-step ($h = 0.1/2^5$ and $\tau = 1 \cdot 10^{-6}$). Since we are working in `FreeFem++`, the software itself chooses the most appropriate solver and preconditioning strategy in order to solve the global system.

The obtained values of the fluid velocity $\boldsymbol{u}^M_{\text{ref}}$, solid velocity $\dot{\boldsymbol{d}}^M_{\text{ref}}$ and solid displacement $\boldsymbol{d}^M_{\text{ref}}$ (in the whole domain and on the interface) at the final time instance M are used as our reference solution. In the labels of the figures of following sections, the reference solution will be referred to as *strongly coupled*.

Then, multiple simulations using Robin-Neumann and Neumann-Robin schemes were done starting from an initial mesh size of $h = 0.1$ and a time step of $\tau = 5 \cdot 10^{-4}$, and

refining them in half each time, i.e

$$\tau = \left\{ \frac{5 \cdot 10^{-4}}{2^i} \right\}_{i=0}^{4}, \quad h = \left\{ \frac{0.1}{2^i} \right\}_{i=0}^{4}.$$

From now on, the term *refinement* at level i, or the notation $"refinement = i"$ will indicate a simultaneous division by 2^i, on the initial mesh size and the time step.

5.3. Robin-Neumann scheme

We first present the results for the Robin-Neumann loosely coupled schemes, which are implemented in Algorithms 2.2 and 2.3. We start by discussing the energy stability of the schemes, showing that LC-RN-MD is unconditionally unstable. Then, the study will focus on the convergence rates for the LC-RN-BDF1 scheme, comparing them with the Robin-Robin loosely coupled schemes.

5.3.1. Energy stability verification

As a first step, the goal is to check whether the LC-RN-BDF1 and LC-RN-MD schemes are stable. In order to do so, we compute the elastic energy from the solid elastic energy:

$$S = \|\boldsymbol{d}_h^n\|_{\mathrm{s}}^2,$$

found in the definition of E_h^n in Theorem 2.1. S represents just one contribution of E_h^n, and it was chosen to simplify the computation. Nevertheless, the blow-up of this term will be used can be used as an indicator of instability: indeed, if this term has a steep increase over time, it suggests fails to preserve stability.

Figure 5.2 shows the energy trend over time for LC-RN-BDF1 and LC-RN-MD, considering different values of α. The figure clearly shows that the energy remains bounded over time for LC-RN-BDF1. It exhibits a stable energy trend, contrary to LC-RN-MD, which exhibits oscillations for all values of α. Even though low values of α could give the impression of a good convergence, the errors are not reliable, as they are not stable over time. Indeed, if we run the simulation for a longer time, we will see the oscillations starting to appear later in time, leading to an unstable solution. This behavior is consistent with the theoretical expectations regarding the stability of these schemes presented in Theorem 2.2.

As a consequence, from now on, the convergence analysis results will be discussed exclusively for LC-RN-BDF1, which is the only one that exhibits stable energy behavior.

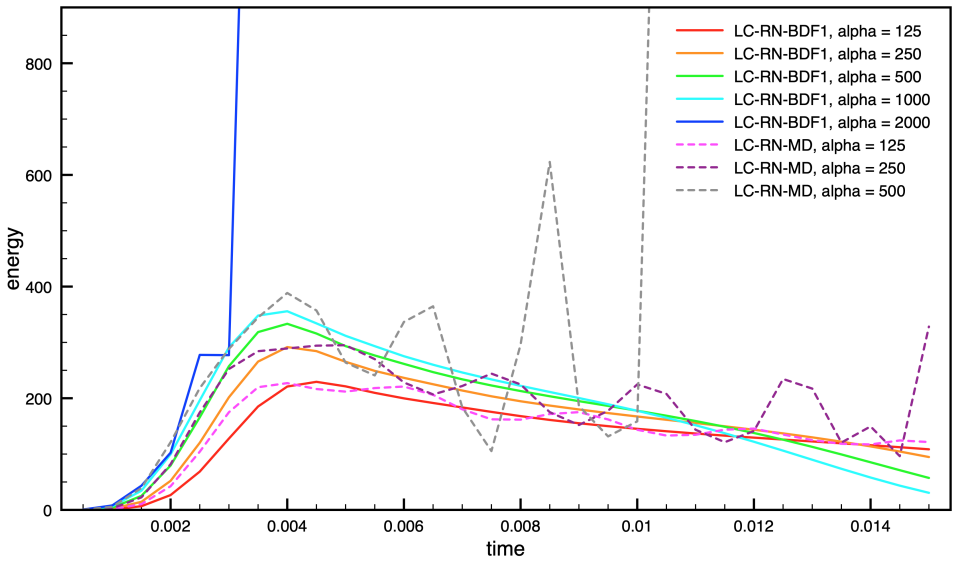

Figure 5.2: Energy trend over time for the LC-RN-BDF1 and LC-RN-MD, considering different values of α with $\tau = 5 \cdot 10^{-4}$ and $h = 0.1$.

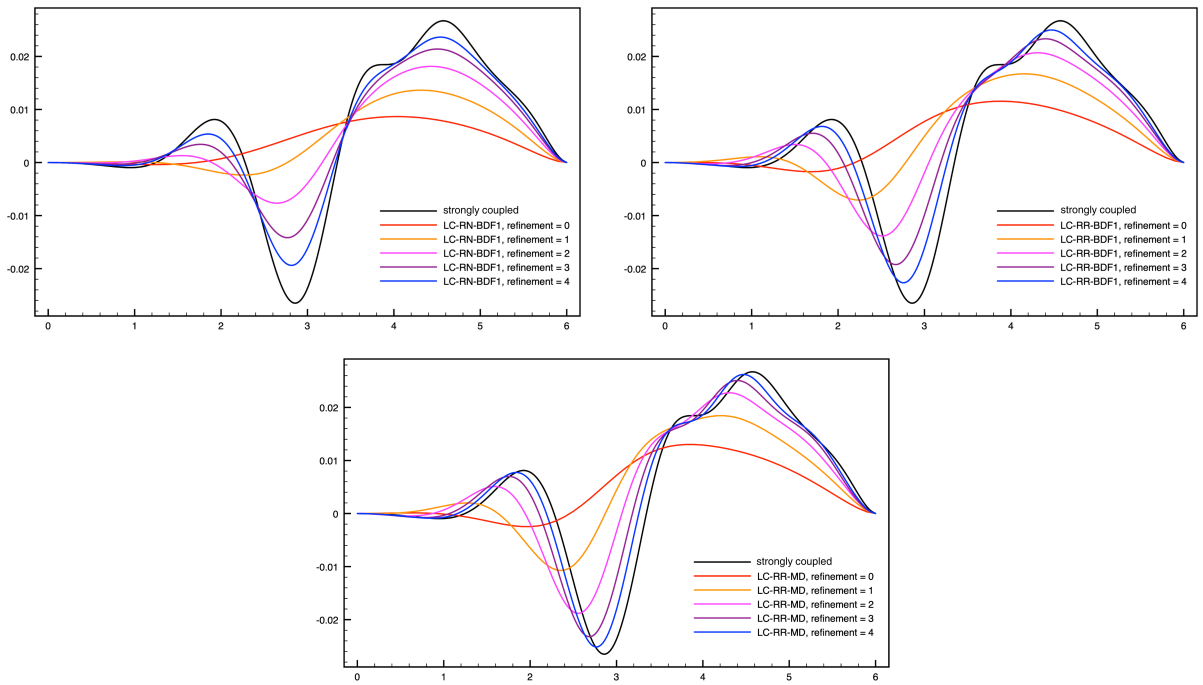

Figure 5.3: Solid displacement at the final time instance $T = 0.015$ using LC-RN-BDF1 (top-left), LC-RR-BDF1 (top-right) and LC-RR-MD (bottom) for $\alpha = 500$ and increasing refinements. Each case is compared with the reference solution obtained by MONO-BDF1.

We computed the solid displacement at the final time instance $T = 0.015$ for different levels of refinements, presented in Figure 5.3, which contains also the solid displacement results for the Robin-Robin schemes, (Algorithms A.1 and A.2), denoted with LC-RR-BDF1 and LC-RR-MD, for comparison purposes. The results are shown for $\alpha = 500$, which is a value that satisfies the stability condition (2.20). Across all schemes, convergence toward the reference solution improves as the mesh is refined. LC-RN-BDF1 shows a consistent convergence trend, closely matching the reference solution atthe fourth refinement, as well as the Robin-Robin schemes. Therefore, we can conclude that the Robin-Neumann scheme is able to capture the solid displacement.

5.3.2. Observed convergence rates

The convergence rates are studied starting from the computational error. The errors are evaluated for all the unknowns of the problem, but the fluid pressure, in order to show the accuracy of the scheme in approximating the reference solution. In particular, they were evaluated using the L^2 norm for $\boldsymbol{u}, \boldsymbol{d}, \dot{\boldsymbol{d}}$ and in the energy norm (2.6) for $\boldsymbol{d}$ as

$$\frac{\|\boldsymbol{d}_{\text{ref}}^M - \boldsymbol{d}(T)\|}{\|\boldsymbol{d}_{\text{ref}}^M\|}.$$

We decided not to study the fluid pressure convergence as it was significantly demanding from a memory point of view. Indeed, unlike all the other variables, from the convergence analysis, we are not able to control the normal at each time step, but only the integral of the error. Therefore, the pressure field would needo to be stored at every time instant.

The results are presented in Figures 5.4 and 5.5. In Figure 5.4, we compare the convergence rates of the solid displacement error in the energy norm for both LC-RR and LC-RN methods, across different values of the Robin parameter α.

The plots clearly show that the error decreases at an approximately linear rate as the mesh and time step are refined, confirming that both schemes exhibit first-order convergence, as theoretically expected. Furthermore, the curves corresponding to LC-RN-BDF1, LC-RR-BDF1 and LC-RR-MD are closely aligned, demonstrating a consistent behavior between the two formulations in terms of accuracy.

Figure 5.5 provides a more detailed breakdown of the convergence behavior for the Robin-Neumann scheme. The figure shows the convergence of the four desired quantities. In all cases, the error curves exhibit a clear trend of first-order convergence as the refinements increase, further validating the reliability and consistency of the numerical scheme.

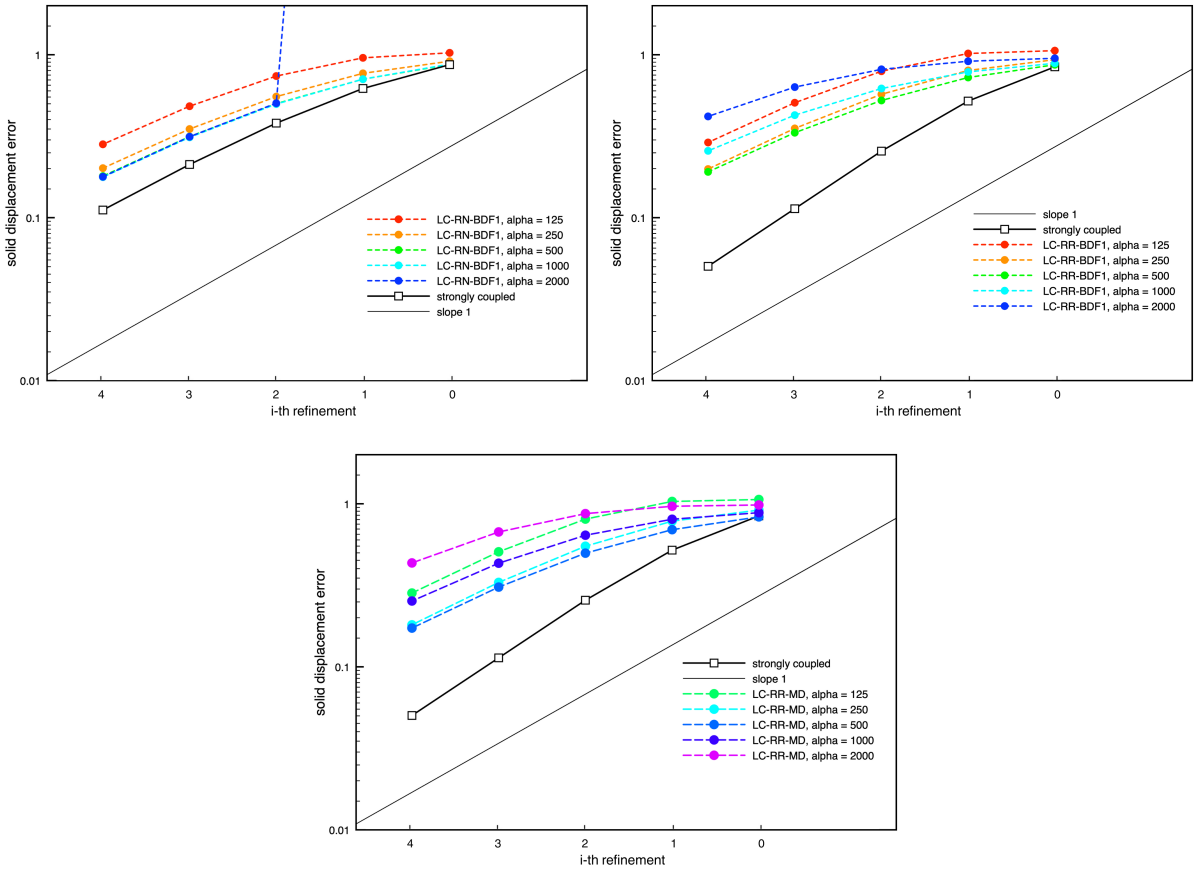

Figure 5.4: Convergence comparison between LC-RN-BDF1 (top-left), LC-RR-BDF1 (top-right) and LC-RR-MD (bottom) for the error of the solid displacement, with different values of α.

It is important to note that, in both Figures 5.4 and 5.5, the behavior of the error is influenced by the value of α: generally, the higher the better, but always satisfying the stability constraint (2.20), which imposes limitations on α. Specifically, for $\alpha = 2000$, the error becomes significantly higher for the coarser refinement. This is highly different from the Robin-Robin case, where the accuracy of the method tends to degrade for larger or smaller values of α.

A convergence study with respect to the number of correction iterations has also been performed to study the sensitivity of the solutions to correction iterations. The results, shown in Figure 5.6, are provided only for the BDF1 formulation for the solid displacement in the energy norm. Although the figure highlights this specific case, it is relevant to notice that a similar convergence behavior is observed for all the other solution variables, indicating a consistent trend. From the plot, it is clear that LC-RN-BDF1 performs already very well in the base case. However, with just a few correction iterations lead to a significant reduction in the error, approaching the accuracy of the strongly coupled refer-

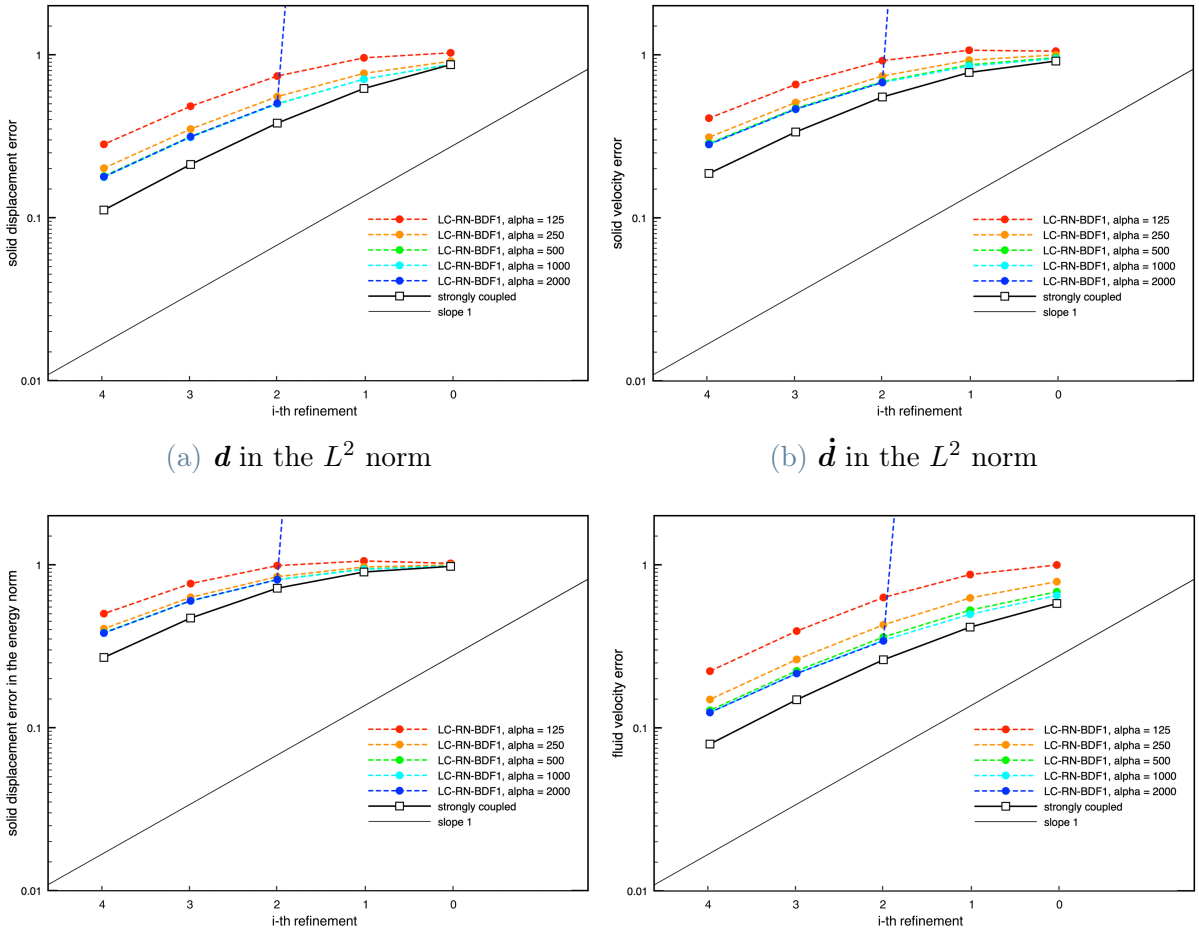

(a) $\boldsymbol{d}$ in the L^2 norm

(b) $\dot{\boldsymbol{d}}$ in the L^2 norm

(c) $\boldsymbol{d}$ in the energy norm

(d) $\boldsymbol{u}$ in the L^2 norm

Figure 5.5: Convergence rates for LC-RN-BDF1 evaluating the errors of the problem unknowns for different values of α and 0 corrections iterations.

ence solution. Overall, the results show the expected first-order accuracy for a restricted set of α, which satisfy (2.20).

Since with $\alpha = 1000$, we already see some instabilities, the next analysis is carried out for $\alpha = 500$. Accordingly to the optimization analysis presented previously, the optimal value of α should be $\alpha_{\text{opt}} = 420$. Therefore, the choice of $\alpha = 500$ can be considered sufficiently close to the theoretical value. Let us recall that the theoretical value was found in a slightly different configuration, hence this small deviation is expected and it does not compromise the validity of our results.

Now, we want to examine the influence of the physical parameters on the accuracy of the solution for $\alpha = 500$. The study is carried out for one value of α, but it is important to highlight that the optimal value of the Robin parameter depends on β, which in its turn, depends on E. Consequently, the optimal value of α changes in the three scenarios. This

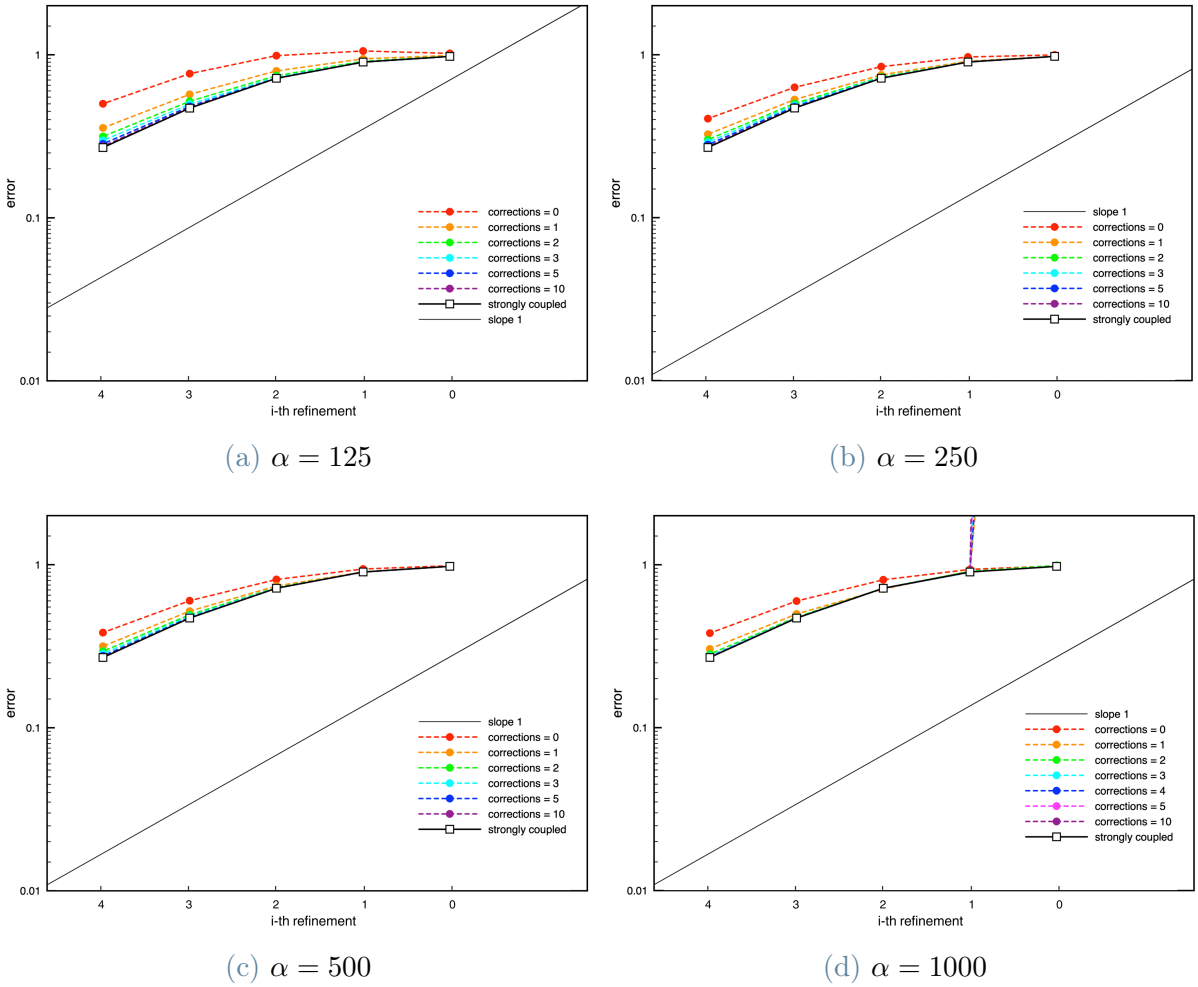

(a) $\alpha = 125$ (b) $\alpha = 250$

(c) $\alpha = 500$ (d) $\alpha = 1000$

Figure 5.6: Convergence rates for LC-RN-BDF1-CI evaluating the errors of the solid displacement in the energy norm for different values of α and different number of corrections.

is proved by Figure 5.7 and 5.8, which show the convergence history for the solid displacement in the energy norm for both the LC-RN-BDF1-CI and LC-RR-CI, with different values of the Young's modulus E. The Robin-Robin case is included for comparison, and its analysis (for the mid-point scheme) is better treated in [13]. It is evident that LC-RN-BDF1-CI is less sensitive to the stiffness of the solid, when the number of corrections is equal to zero, as the error remains relatively stable across different values. At the same time, when $E = 1.58 \cdot 10^5$, we start to see that the error reaches higher values. For both schemes, the error deeply decreases the moment we add a few correction iterations.

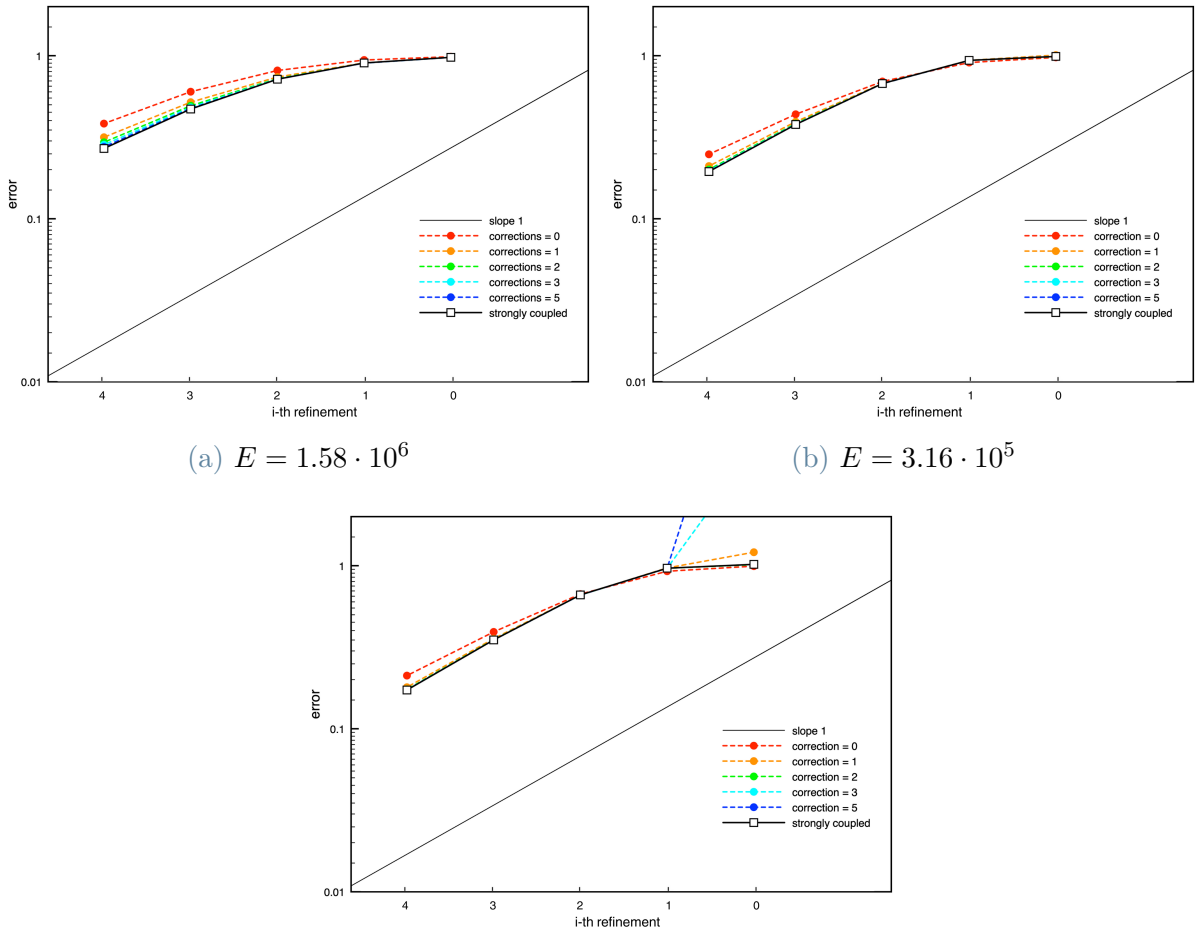

(a) $E = 1.58 \cdot 10^6$

(b) $E = 3.16 \cdot 10^5$

(c) $E = 1.58 \cdot 10^5$

Figure 5.7: Convergence rates for LC-RN-BDF1-CI evaluating the errors of the solid displacement in the energy norm for $\alpha = 500$ and different values of the Young's module E.

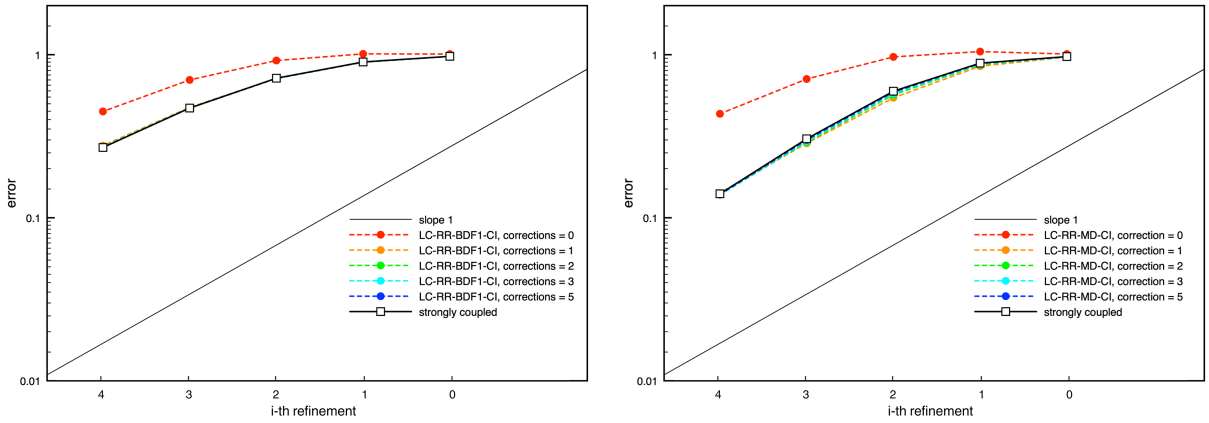

(a) $E = 1.58 \cdot 10^6$

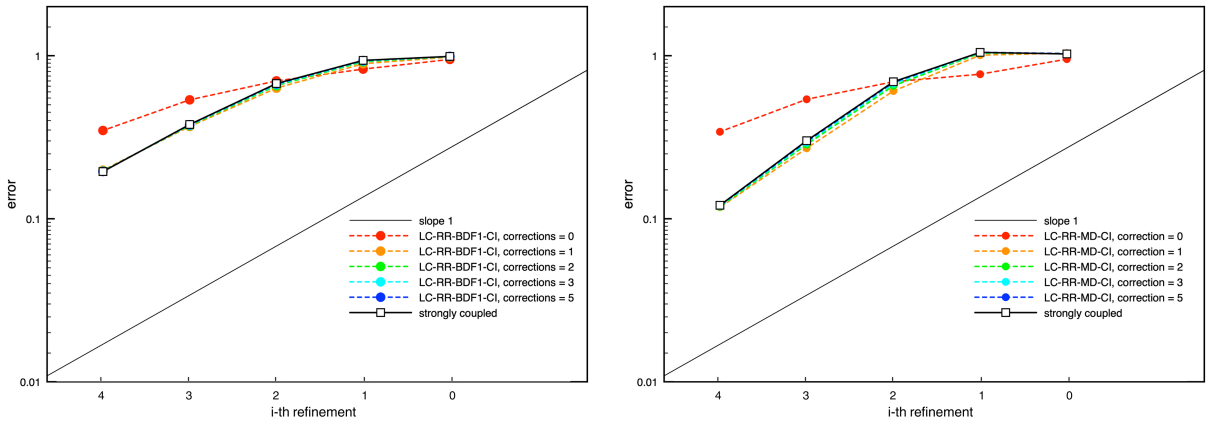

(b) $E = 3.16 \cdot 10^5$

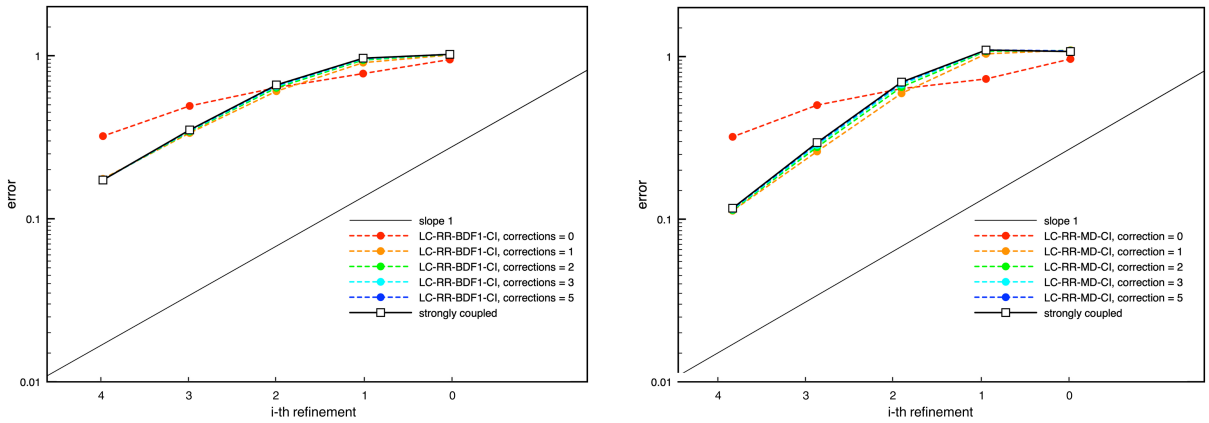

(c) $E = 1.58 \cdot 10^5$

Figure 5.8: Convergence rates for LC-RR-BDF1-CI (on the left column) and LC-RR-MD-CI (on the right column), evaluating the errors of the solid displacement in the energy norm for $\alpha = 500$ and different values of the Young's module E.

5.4. Neumann-Robin scheme

We also implemented the Neumann-Robin loosely coupled scheme, as described in Algorithm 3.1 and 3.2. We proceed the discussion of the results in a similar way as for the standard Robin-Neumann scheme, starting with the energy stability and then presenting the convergence rates.

Figure 5.9 shows the time evolution of the elastic energy for Algorithms 3.1 and 3.2, for different values of α. The energy is computed exactly as the standard case, from the only term $S = \|\boldsymbol{d}_h^n\|_s^2$. The figure shows that the Neumann-Robin scheme maintains a stable energy evolution over time, for both LC-NR-BDF1 and LC-NR-MD schemes. We included also the case of $\alpha = 500$ to show the behavior of the schemes for a value of α that does not satisfy the stability condition (3.7). This is consistent with the theoretical expectations regarding the stability of these scheme, stated in Theorems 3.1 and 3.2, confirming that the reversed coupling conditions do not introduce additional instabilities in the energy evolution.

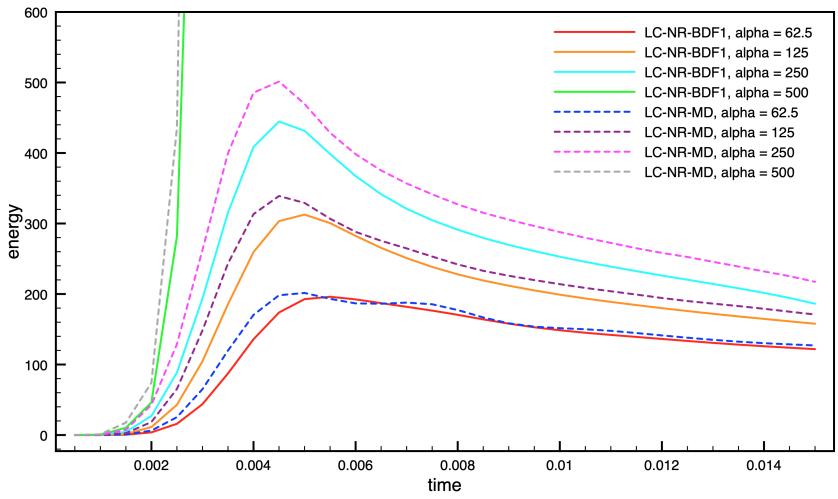

Figure 5.9: Energy trend over time for the LC-NR-BDF1 and LC-NR-MD, considering different values of α with $\tau = 5 \cdot 10^{-4}$ and $h = 0.1$.

Then, we computed the solid displacement at the final time instance $T = 0.015$ using the Neumann-Robin schemes for different levels of refinements, presented in Figure 5.10. The results are shown for $\alpha = 125$, which is a value that satisfies the stability condition (3.7). The figure clearly illustrates that, as the mesh and time step are refined, the solution converges towards the reference solution, demonstrating the effectiveness of both of the Neumann-Robin schemes in capturing the solid displacement accurately.

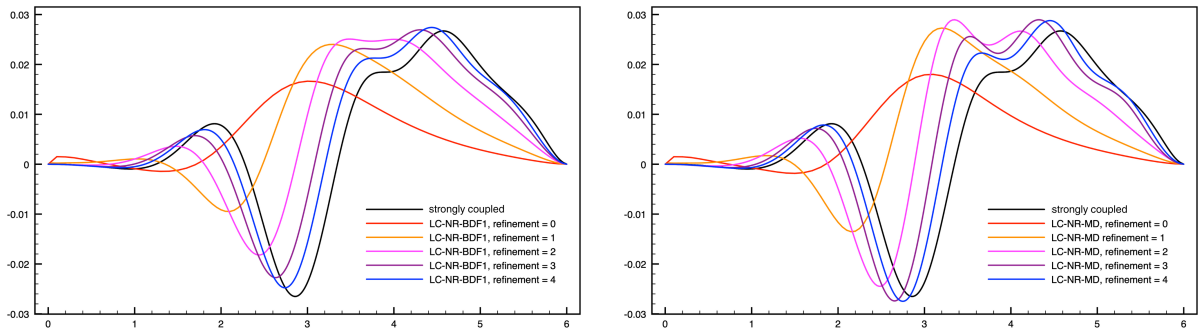

Figure 5.10: Solid displacement at the final time instance $T = 0.015$ using the LC-NR-BDF1 (on the left) and LC-NR-MD (on the right) schemes with $\alpha = 125$ for increasing refinements.

The convergence results are presented in Figure 5.11. The figure shows the convergence of the solid displacement error in the energy norm for different values of α. It is important to remark that the case of $\alpha = 250$ is not reported for the LC-NR-MD case, as its error resulted extremely large, leading to the conclusion that this value is not satisfied by the CFL-like condition for stability. The results indicate that the Neumann-Robin scheme exhibits a similar convergence behavior to the standard Robin-Neumann scheme. However, it is clear that the values of α that satisfy the stability condition (3.7) for the BDF1 scheme and that can produce accurte results are significantly lower than the ones for the standard Robin-Neumann scheme.

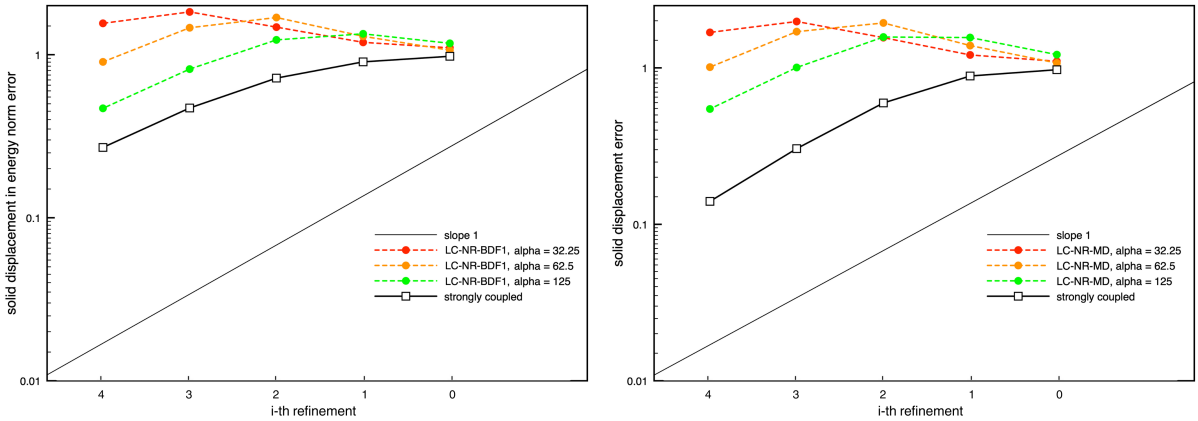

Figure 5.11: Convergence rates for LC-NR-BDF1 (on the left) and LC-NR-MD (on the right) evaluating the errors of the solid displacement in the energy norm for different values of α.

We also performed a convergence study with respect to the number of correction iterations for the Neumann-Robin scheme. The results, shown in Figure 5.12, are provided only for

LC-NR-BDF1-CI and LC-NR-MD-CI for the solid displacement in the energy norm with a Robin parameter of $\alpha = 125$. Here, the optimal value of α, which now refers to the solid, can be found from (5.2). This results in having $\alpha_{\text{opt}} = 127$. We therefore choose $\alpha = 125$ as the best value to carry the analysis.

Figure 5.12a highlights that, similarly to the Robin-Neumann scheme, the Neumann-Robin scheme performs well in the base case. However, with just a few correction iterations, it leads to a significant reduction in the error, approaching the accuracy of the fully coupled reference solution. It is noticeable that, with respect to the previous case, the errors seem to be slightly better that the reference solution. The fact that we don't have an exact solution for the problem, but only a fine approximation of it, obtained using a monolithic formulation, could affect the errors and lead to this behavior.

Lastly, as we did for the Robin-Neumann scheme, we want to examine the influence of the physical parameters on the accuracy of the solution for the best choice of α. The study is carried out only for the value of $\alpha = 125$ in Figures 5.12b and 5.12c. The results show that, as E decreases, the zero-correction case is already able to well capture the implicit solution, and with just a few correction iterations, the error is significantly reduced.

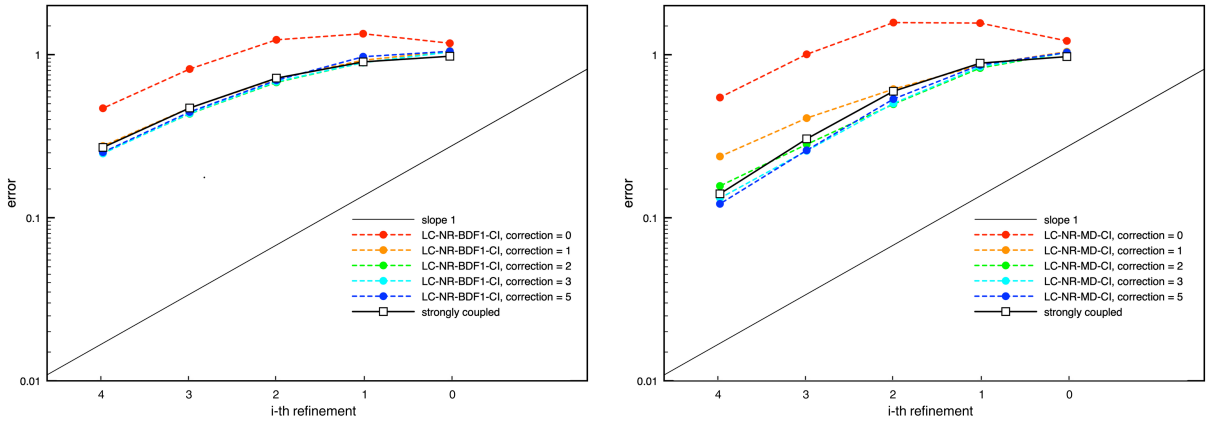

(a) $E = 1.58 \cdot 10^6$

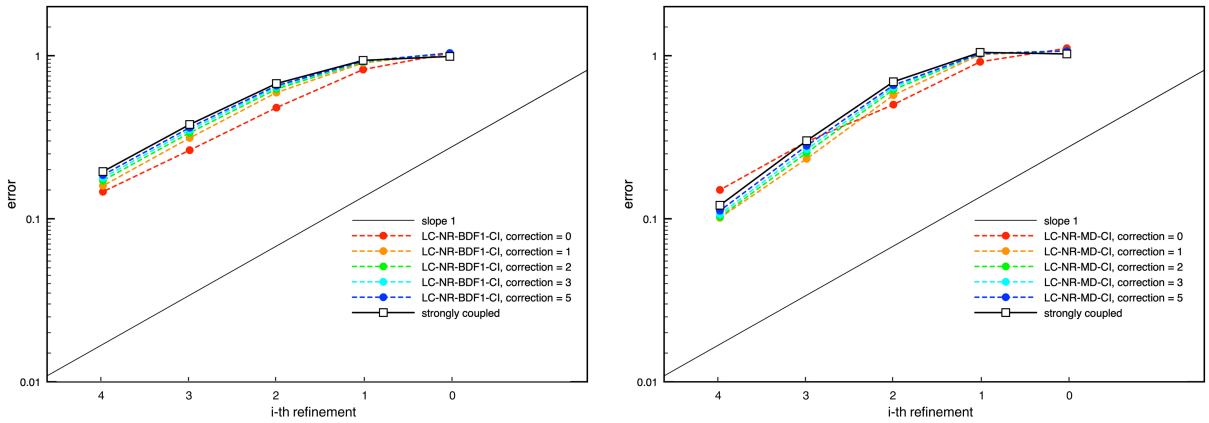

(b) $E = 3.16 \cdot 10^5$

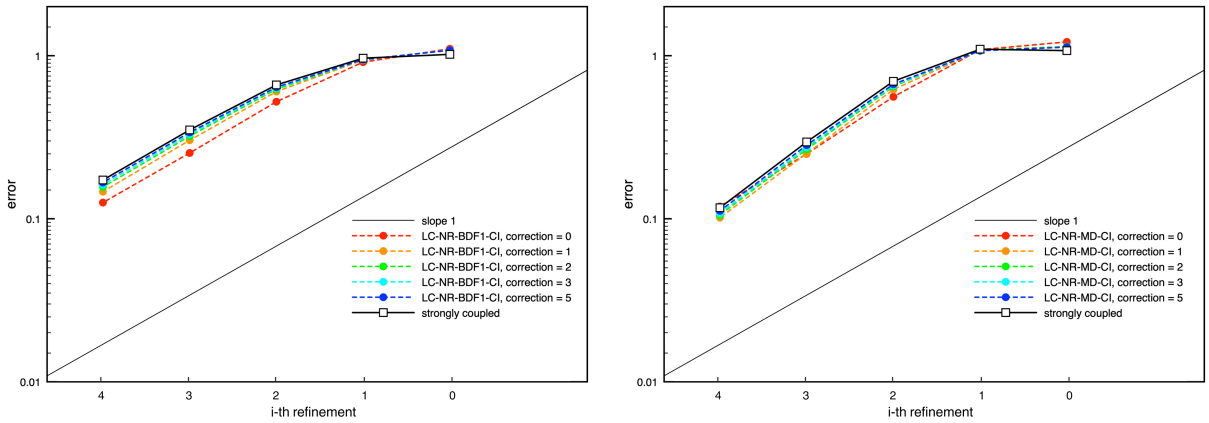

(c) $E = 1.58 \cdot 10^5$

Figure 5.12: Convergence rates for LC-NR-BDF1-CI (on the left) and LC-NR-MD-CI (on the right), evaluating the errors of the solid displacement in the energy norm for $\alpha = 125$, different values of the Young's modulus E.

Part II

Nonlinear Setting

The second part of this thesis extends the study to nonlinear fluid-structure interaction problems, aiming to assess the robustness and applicability of loosely coupled schemes in more realistic and complex settings. The primary goal here is to adapt and evaluate the Neumann-Robin time-splitting strategy in the presence of nonlinearities.

This part is structured as follows:

Chapter 6. It introduces the nonlinear monolithic formulation as a reference point, followed by the derivation of a partitioned Neumann-Robin scheme tailored for the nonlinear context in non moving domains with the ALE map.

Chapter 7. It presents several benchmark test cases in two and three dimensions, including a 2D balloon, a 2D lid-driven cavity and a 3D tube, which serve to assess the scheme's stability and accuracy. The results highlight the potential and limitations of the proposed method in capturing nonlinear FSI dynamics while maintaining computational efficiency and modularity.

6 | The nonlinear problem

Contents

This chapter aims to present the nonlinear fluid-structure interaction problem in a moving domain. After presenting the problem in ALE formalism, the monolithic formulation is proposed. Focus will be on the use of Neumann-Robin coupling conditions: stabilization techniques are incorporated to handle the challenges posed by nonlinearities and high Reynolds numbers. The chapter concludes by outlining the fully discretized algorithm, which will serve as the basis for the numerical assessment in the next chapter.

6.1. Model problem

This section aims to present the fluid equations, solid equations and coupling conditions in non linear settings.

The reference configuration is represented by $\Omega := \Omega^{\mathrm{f}} \cup \Omega^{\mathrm{s}} \subset \mathbb{R}^d$ and with interface $\Sigma := \partial\Omega^{\mathrm{f}} \cap \partial\Omega^{\mathrm{s}}$. For all $t > 0$, we denote the moving fluid domain by $\Omega^{\mathrm{f}}(t)$ and the moving solid domain by $\Omega^{\mathrm{s}}(t)$. The current configuration of the interface is denoted by $\Sigma(t) := \partial\Omega^{\mathrm{f}}(t) \cap \partial\Omega^{\mathrm{s}}(t)$.

As the fluid domain is deformable, it strictly depends on the solid displacement $\boldsymbol{d}$:

$\Omega^s \times \mathbb{R}^+ \to \mathbb{R}^d$, with $d = 2, 3.$, with $d = 2, 3$, through a deformation map

$$\boldsymbol{\varphi} : \Omega^s \times \mathbb{R}^+ \to \mathbb{R}^d.$$

We will denote $\boldsymbol{\varphi}_t := \boldsymbol{\varphi}(\cdot, t)$. As a consequence, it is possible to write the solid domain evolution as $\Omega^s(t) := \boldsymbol{\varphi}_t(\Omega^s)$, as well as the interface evolution as $\Gamma(t) := \boldsymbol{\varphi}_t(\Gamma)$.

Regarding the solid model, the choice falls on the most appropriate one (for instance, rigid models or elastic models), usually written in Lagrangian coordinates. Here, the main focus wants to be on the fluid equations. The equations that describe fluid motions are the Navier-Stokes equations, in Eulerian coordinates. The system equations are:

$$\begin{cases} \rho^s \partial_t \dot{\boldsymbol{d}} - \mathbf{div}\boldsymbol{\sigma}^s(\boldsymbol{d}) = \mathbf{0} & \text{in } \Omega^s, \\ \dot{\boldsymbol{d}} = \partial_t \boldsymbol{d} & \text{in } \Omega^s, \\ \rho^f \partial_t \boldsymbol{u} + \rho^f (\boldsymbol{u} \cdot \boldsymbol{\nabla})\boldsymbol{u} - \mathbf{div}\boldsymbol{\sigma}^f(\boldsymbol{u}, p) = \mathbf{0} & \text{in } \Omega^f(t), \\ \operatorname{div} \boldsymbol{u} = 0 & \text{in } \Omega^f(t). \end{cases}$$

where $\boldsymbol{\sigma}^s(\boldsymbol{d})$ and $\boldsymbol{\sigma}^f(\boldsymbol{u}, p)$ are exactly as defined in (2.2) and (2.3).

In order to couple the Lagrangian model of the solid with the Eulerian model of the fluid, the solid displacement $\boldsymbol{d}$ and the solid velocity $\dot{\boldsymbol{d}}$, living on the reference configuration, must be transformed through the map $\boldsymbol{\varphi}_t$.

6.2. Introduction to the ALE formalism

In FSI problems, the fluid domain Ω^f represents itself an unknown of the problem. To account for its motion, the incompressible Navier-Stokes equations are written in Arbitrary Lagrangian-Eulerian formalism (ALE) [22, 29] while the solid is described by a nonlinear elastodynamic model [14] in total Lagrangian formalism.

This section aims to present the main concepts of the ALE approach, which will be later applied onto the problem of our consideration.

6.2.1. The ALE map

In order to parametrize the fluid domain motion, we employ a bijective map, known as ALE map (see Figure 6.1)

$$\boldsymbol{\mathcal{A}} : \Omega^f \times \mathbb{R}^+ \to \mathbb{R}^d$$

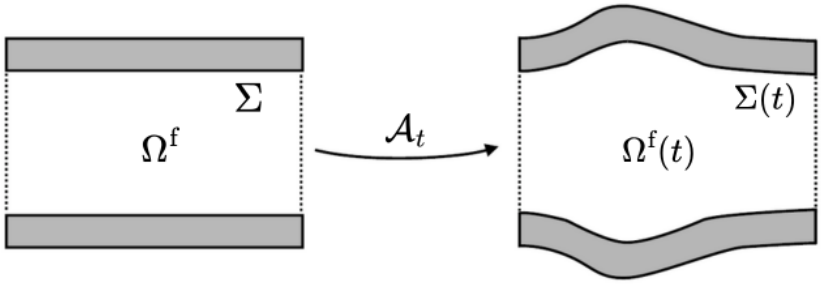

Figure 6.1: Example of computational fluid domain Ω^f, whose evolution $\Omega^f(t)$ is described by the ALE map $\boldsymbol{\mathcal{A}}_t$.

with $d = 2, 3$, defined such that $\Omega^f(t) = \boldsymbol{\mathcal{A}}(\Omega^f, t)$ for any $t > 0$. Introducing the notation $\boldsymbol{\mathcal{A}}_t := \boldsymbol{\mathcal{A}}(\cdot, t)$, for any general Eulerian field f, we will denote its ALE description in Ω^f with a hat, for example $\widehat{f}$, obtained by composing f itself with the ALE map:

$$\widehat{f}(\boldsymbol{x}, t) := f(\boldsymbol{\mathcal{A}}(\boldsymbol{x}, t), t) \quad \forall \boldsymbol{x} \in \Omega^f,$$

or equivalently, $\widehat{f}(\cdot, t) = f(\cdot, t) \circ \boldsymbol{\mathcal{A}}_t$. Conversely, since the ALE map is bijective, the inverse map $\boldsymbol{\mathcal{A}}^{-1}$ can be used, by composition, to transport a given field from the current configuration to the reference configuration:

$$f(\boldsymbol{x}(t), t) = \widehat{f}(\boldsymbol{\mathcal{A}}^{-1}(\boldsymbol{x}(t)), t) \quad \forall \boldsymbol{x}(t) \in \Omega^f(t),$$

also written as $f(\cdot, t) = \widehat{f}(\cdot, t) \circ \boldsymbol{\mathcal{A}}_t^{-1}$.

6.2.2. Construction of the ALE map

The ALE map can be defined as a function of the fluid domain displacement $\boldsymbol{d}^f = \mathrm{Ext}(\boldsymbol{d}|_\Sigma)$, having $\boldsymbol{\mathcal{A}} = \boldsymbol{I}_{\Omega^f} + \boldsymbol{d}^f$. Here, Ext is a lifting operator of the solid displacement from Σ to Ω^f and $\boldsymbol{I}_{\Omega^f}$ is the identity operator on Ω^f. As a consequence, we have that $\boldsymbol{d}^f = \boldsymbol{d}$ on Σ. On the other hand, as the inlet and outlet boundaries are fixed, we have that $\boldsymbol{d}^f = \boldsymbol{0}$ on Γ^f.

One possible way to construct the ALE map is to construct the operator Ext that solves a an harmonic extension of the displacement $\boldsymbol{d}^f$ resulting in the following system:

$$\begin{cases} \Delta \boldsymbol{d}^f = 0 & \text{in } \Omega^f, \\ \boldsymbol{d}^f = \boldsymbol{d} & \text{on } \Sigma, \\ \boldsymbol{d}^f = \boldsymbol{0} & \text{on } \Gamma^f. \end{cases}$$

6.2.3. The ALE time derivative

The fluid domain velocity (or mesh velocity) $\boldsymbol{w}$ is defined as

$$\boldsymbol{w} := \partial_t \boldsymbol{\mathcal{A}}_t = \partial_t \boldsymbol{d}^{\mathrm{f}} \quad \text{in } \Omega^{\mathrm{f}}(t).$$

For a general vectorial Eulerian field $\boldsymbol{f}$, we can define the ALE time derivative as:

$$\partial_t \boldsymbol{f}|_{\boldsymbol{\mathcal{A}}}(\boldsymbol{x}(t), t) = \frac{\mathrm{d}}{\mathrm{d}t}\boldsymbol{f}(\boldsymbol{\mathcal{A}}(\boldsymbol{x}, t), t),$$

which then gives, thanks to the chain rule, the following expression

$$\left.\frac{\partial \boldsymbol{f}}{\partial t}\right|_{\boldsymbol{\mathcal{A}}} := \frac{\partial \boldsymbol{f}}{\partial t} + \boldsymbol{w} \cdot \boldsymbol{\nabla} \boldsymbol{f}. \tag{6.1}$$

6.3. Application to FSI problems

In this section we reformulate the FSI problem (2.1) considered in the first part when applying the ALE formalism.

To apply the ALE formalism, we need to change the reference frame of the Navier-Stokes equations by changing the time derivative term. The strongly coupled problem is defined as follows: find the fluid velocity $\widehat{\boldsymbol{u}} : \Omega^{\mathrm{f}} \times \mathbb{R}^+ \to \mathbb{R}^d$, the fluid pressure $\widehat{p} : \Omega^{\mathrm{f}} \times \mathbb{R}^+ \to \mathbb{R}^d$, the solid displacement $\boldsymbol{d} : \Omega^{\mathrm{s}} \times \mathbb{R}^+ \to \mathbb{R}^d$ and the solid velocity $\dot{\boldsymbol{d}} : \Omega^{\mathrm{s}} \times \mathbb{R}^+ \to \mathbb{R}^d$ such that:

$$\begin{cases} \rho^{\mathrm{f}} \partial_t \boldsymbol{u}|_{\boldsymbol{\mathcal{A}}} + \rho^{\mathrm{f}}(\boldsymbol{u} - \boldsymbol{w}) \cdot \boldsymbol{\nabla} \boldsymbol{u} - \mathbf{div}\, \boldsymbol{\sigma}^{\mathrm{f}}(\boldsymbol{u}, p) = \boldsymbol{0} & \text{in } \Omega^{\mathrm{f}}(t), \\ \operatorname{div} \boldsymbol{u} = 0 & \text{in } \Omega^{\mathrm{f}}(t), \\ \boldsymbol{u} = \boldsymbol{0} & \text{on } \Gamma^{\mathrm{f}}, \\ \rho^{\mathrm{s}} \partial_t \dot{\boldsymbol{d}} - \mathbf{div}\,(\boldsymbol{F}^{\mathrm{s}} \widetilde{\boldsymbol{\Sigma}}(\boldsymbol{d})) = \boldsymbol{0} & \text{in } \Omega^{\mathrm{s}}, \\ \dot{\boldsymbol{d}} = \partial_t \boldsymbol{d} & \text{in } \Omega^{\mathrm{s}}, \\ \boldsymbol{d} = \boldsymbol{0} & \text{on } \Gamma^{\mathrm{s}}, \\ \boldsymbol{d}^{\mathrm{f}} = \boldsymbol{\mathcal{L}}(\boldsymbol{d}|_{\Sigma}), \quad \boldsymbol{w} = \partial_t \boldsymbol{d}^{\mathrm{f}}, \quad \boldsymbol{\mathcal{A}} = \boldsymbol{I}_{\Omega^{\mathrm{f}}} + \boldsymbol{d}^{\mathrm{f}}, \quad \Omega^{\mathrm{f}}(t) = \boldsymbol{\mathcal{A}}(\Omega^{\mathrm{f}}, t), & \\ \widehat{\boldsymbol{u}} = \dot{\boldsymbol{d}} & \text{on } \Sigma, \\ \boldsymbol{F}^{\mathrm{s}} \widetilde{\boldsymbol{\Sigma}}(\boldsymbol{d}) \boldsymbol{n}^{\mathrm{s}} = -J \widehat{\boldsymbol{\sigma}}^{\mathrm{f}}(\boldsymbol{u}, p) \boldsymbol{F}^{-\mathrm{T}} \widehat{\boldsymbol{n}} & \text{on } \Sigma, \end{cases} \tag{6.2}$$

complemented with appropriate initial conditions $\widehat{\boldsymbol{u}}(0) = \widehat{\boldsymbol{u}}_0$ in Ω^{f}, $\boldsymbol{d}(0) = \boldsymbol{d}_0$ and $\dot{\boldsymbol{d}}(0) =$

$\dot{\boldsymbol{d}}_0$ in Ω^{s}.

In system (6.2), $\boldsymbol{F}^{\mathrm{s}} := \boldsymbol{I} + \boldsymbol{\nabla} \boldsymbol{d}$ is the gradient of deformation of the solid and $\widetilde{\boldsymbol{\Sigma}}(\boldsymbol{d})$ is the second Piola-Kirchhoff stress tensor. For an hyperelastic material, it is given as a function of the internal energy functional $W : \mathbb{R}^{d\times d}_{\mathrm{sym}} \to \mathbb{R}^{+}$:

$$\widetilde{\boldsymbol{\Sigma}} = \frac{\partial W}{\partial \boldsymbol{E}}(\boldsymbol{E}), \qquad \boldsymbol{E} = \frac{1}{2}((\boldsymbol{F}^{\mathrm{s}})^{\mathrm{T}}\boldsymbol{F}^{\mathrm{s}} - \boldsymbol{I})$$

where $\boldsymbol{E}$ denotes the Green-Lagrange strain tensor.

The coupling condition $(6.2)_7$ states that the solid displacement $\boldsymbol{d}^{\mathrm{f}}$ is related to the solid displacement $\boldsymbol{d}$ on the interface Σ through a linear lifting operator $\boldsymbol{\mathcal{L}}$. This operator is the mathematical tool that transfers the Lagrangian displacement of the solid at the interface into the ALE displacement of the fluid domain. This connection allows the Eulerian fluid domain to deform consistently with the solid, despite being governed in a different reference frame. Thus, $\boldsymbol{\mathcal{L}}$ is the bridge between the Lagrangian description of the solid and the ALE description of the fluid. In particular, condition $(6.2)_7$ ensures the fluid and solid domains fit together geometrically, while conditions $(6.2)_{8,9}$ guarantee the coupling of motion and forces across the interface.

6.3.1. Monolithic formulation

We consider the same spaces (2.4) as in the linear setting. Let $(\widehat{\boldsymbol{u}}, \widehat{p}, \boldsymbol{d}, \dot{\boldsymbol{d}})$ be the solution of the nonlinear problem (6.2). The monolithic variational formulation reads as in Algorithm 6.1. The coupling conditions (6.2) are applied strongly thanks to the imposition of $\boldsymbol{v} = \boldsymbol{\xi}$ on the interface Σ.

Algorithm 6.1 Continuous weak formulation of the nonlinear coupled problem

For $t > 0$, find $(\widehat{\boldsymbol{u}}(t), \widehat{p}(t), \boldsymbol{d}(t), \dot{\boldsymbol{d}}(t)) \in \boldsymbol{V}^{\mathrm{f}} \times M^{\mathrm{f}} \times \boldsymbol{V}^{\mathrm{s}} \times \boldsymbol{V}^{\mathrm{s}}$ with $\dot{\boldsymbol{d}} = \partial_t \boldsymbol{d}$, $\boldsymbol{u} = \dot{\boldsymbol{d}}$, and such that:

$$\begin{aligned}
&\rho^{\mathrm{f}} \frac{\mathrm{d}}{\mathrm{d}t} \int_{\Omega^{\mathrm{f}}(t)} \boldsymbol{u} \cdot \boldsymbol{v} - \rho^{\mathrm{f}} \int_{\Omega^{\mathrm{f}}(t)} (\operatorname{div} \boldsymbol{w}) \boldsymbol{u} \cdot \boldsymbol{v} + \rho^{\mathrm{f}} \int_{\Omega^{\mathrm{f}}(t)} (\boldsymbol{u} - \boldsymbol{w}) \cdot \boldsymbol{\nabla} \boldsymbol{u} \cdot \boldsymbol{v} + 2\mu \int_{\Omega^{\mathrm{f}}(t)} \boldsymbol{\epsilon}(\boldsymbol{u}) : \boldsymbol{\epsilon}(\boldsymbol{v}) \\
&\quad - \int_{\Omega^{\mathrm{f}}(t)} p \operatorname{div} \boldsymbol{v} + \int_{\Omega^{\mathrm{f}}(t)} q \operatorname{div} \boldsymbol{u} + \rho^{\mathrm{s}} \int_{\Omega^{\mathrm{s}}} \partial_t \dot{\boldsymbol{d}} \cdot \boldsymbol{\xi} + \int_{\Omega^{\mathrm{s}}} \widetilde{\boldsymbol{\Sigma}} : \frac{1}{2} \left[(\boldsymbol{F}^{\mathrm{s}})^{\mathrm{T}} \boldsymbol{\nabla} \boldsymbol{\xi} + (\boldsymbol{\nabla} \boldsymbol{\xi})^{\mathrm{T}} \boldsymbol{F}^{\mathrm{s}} \right] = 0,
\end{aligned}$$

for all $(\boldsymbol{v}, q, \boldsymbol{\xi}) \in \boldsymbol{V}^{\mathrm{f}} \times M^{\mathrm{f}} \times \boldsymbol{V}^{\mathrm{s}}$, with $\boldsymbol{v}|_{\Sigma} = \boldsymbol{\xi}|_{\Sigma}$.

We emphasize that Algorithm 6.1 is written using the conservative formulation, which ensures the preservation of mass and momentum within the moving fluid domain. This is

reflected in the placement of the material derivative $\frac{\mathrm{d}}{\mathrm{d}t}$ outside of the integral over $\Omega^{\mathrm{f}}(t)$ and the appearance of the second integral thanks to Reynolds transport theorem [30, Proposition 3.7]. On the other hand, as the solid domain is considered to be fixed, the time derivative applied to the solid velocity $\partial_t \dot{\boldsymbol{d}}$ can be left inside of the integral.

6.3.2. Neumann-Robin loosely coupled scheme

The purpose of this section is to present the Neumann-Robin loosely coupled scheme applied to the nonlinear problem (6.2). We focus on the discretization in time with BDF1 in the fluid domain and mid-point in the solid domain. This choice motivated by the code structure of the `FELiScE` library, used to implement the scheme, but this point will be better treated in Chapter 7. As a consequence, we will only work with the LC-NR-MD problem, since from Section 2.3.2, we know that Robin-Neumann with midpoint in the solid (LC-RN-MD) is unconditionally unstable. We remind that the actual procedure starts with solving the solid subproblem with the Robin condition. This ordering follows the same convention used for the linear case in Chapter 3.

We use the same spaces as in the linear setting (2.8) and we introduce the solid stresses on the reference configuration on Σ as

$$\boldsymbol{\lambda}^n := \boldsymbol{F}^{\mathrm{s},n} \widetilde{\boldsymbol{\Sigma}}^n \boldsymbol{n}^{\mathrm{s}}.$$

The time stepping procedure is defined as follows:

$$\begin{cases} \rho^{\mathrm{s}} \partial_\tau \dot{\boldsymbol{d}}^n - \mathbf{div}\left(\boldsymbol{F}^{\mathrm{s},n-\frac{1}{2}} \widetilde{\boldsymbol{\Sigma}}^{n-\frac{1}{2}}\right) = \boldsymbol{0} & \text{in } \Omega^{\mathrm{s}}, \\ \dot{\boldsymbol{d}}^{n-\frac{1}{2}} = \partial_\tau \boldsymbol{d}^n & \text{in } \Omega^{\mathrm{s}}, \\ \boldsymbol{d}^n = \boldsymbol{0} & \text{on } \Gamma^{\mathrm{s}}, \\ \boldsymbol{\lambda}^{n-\frac{1}{2}} + \alpha \dot{\boldsymbol{d}}^{n-\frac{1}{2}} = \alpha \widehat{\boldsymbol{u}}^{n-1} + \boldsymbol{\lambda}^{n-\frac{3}{2}} & \text{on } \Sigma, \end{cases}$$

$$\left\{ \boldsymbol{d}^{\mathrm{f},n} = \boldsymbol{\mathcal{L}}(\boldsymbol{d}^{n-1}|_\Sigma), \quad \boldsymbol{w}^n = \partial_\tau \boldsymbol{d}^{\mathrm{f},n}, \quad \boldsymbol{\mathcal{A}}^n = \boldsymbol{I}_{\Omega^{\mathrm{f}}} + \boldsymbol{d}^{\mathrm{f},n}, \quad \Omega^{\mathrm{f},n} = \boldsymbol{\mathcal{A}}^n(\Omega^{\mathrm{f}}), \right.$$

$$\begin{cases} \rho^{\mathrm{f}} \partial_\tau \boldsymbol{u}^n|_{\boldsymbol{\mathcal{A}}} + \rho^{\mathrm{f}}(\boldsymbol{u}^{n-1} - \boldsymbol{w}^n) \cdot \nabla \boldsymbol{u}^n - \mathbf{div}\, \boldsymbol{\sigma}^{\mathrm{f}}(\boldsymbol{u}^n, p^n) = \boldsymbol{0} & \text{in } \Omega^{\mathrm{f},n}, \\ \operatorname{div} \boldsymbol{u}^n = 0 & \text{in } \Omega^{\mathrm{f},n}, \\ \boldsymbol{u}^n = \boldsymbol{0} & \text{on } \Gamma^{\mathrm{f}}, \\ J^n \widehat{\boldsymbol{\sigma}}(\boldsymbol{u}^n, p^n)(\boldsymbol{F}^n)^{-\mathrm{T}} \widehat{\boldsymbol{n}} = -\boldsymbol{\lambda}^{n-\frac{1}{2}} & \text{on } \Sigma, \end{cases}$$

where we have denoted with $\widetilde{\boldsymbol{\Sigma}}^{n-\frac{1}{2}}$ the mid-point approximation of the second Piola-

Kirchhoff stress tensor, defined as

$$\widetilde{\boldsymbol{\Sigma}}^{n-\frac{1}{2}} := \frac{\partial W}{\partial \boldsymbol{E}}(\boldsymbol{E}^{n-\frac{1}{2}}), \quad \boldsymbol{E}^{n-\frac{1}{2}} := \boldsymbol{E}(\boldsymbol{d}^{n-\frac{1}{2}})$$

Regarding the space discretization, we employ the same spaces as in the linear setting (2.8). The fully discrete Neumann-Robin loosely coupled scheme with BDF1 for the nonlinear problem is presented in Algorithm 6.2.

Here, the fluid bilinear form

$$\begin{aligned} a_{\Omega^{\mathrm{f},n}}(\boldsymbol{u}_h^{n-1}, \boldsymbol{w}_h^n; (\boldsymbol{u}_h^n, p_h^n), (\boldsymbol{v}_h, q_h)) &:= \rho^{\mathrm{f}} \int_{\Omega^{\mathrm{f},n}} (\boldsymbol{u}_h^{n-1} - \boldsymbol{w}_h^n) \cdot \nabla u_h^n \cdot v_h \\ &+ \frac{\rho^{\mathrm{f}}}{2} \int_{\Omega^{\mathrm{f},n}} \mathrm{div}\,(\boldsymbol{u}_h^{n-1} - 2\boldsymbol{w}_h^n)\boldsymbol{u}_h^n \cdot \boldsymbol{v}_h - \frac{\rho^{\mathrm{f}}}{2} \int_{\Sigma^n} (\boldsymbol{u}_h^{n-1} - \dot{\boldsymbol{d}}_h^{n-\frac{1}{2}}) \cdot \boldsymbol{n}\boldsymbol{u}_h^n \cdot v_h \\ &+ 2\mu \int_{\Omega^{\mathrm{f},n}} \boldsymbol{\epsilon}_h(\boldsymbol{u}_h^n) : \boldsymbol{\epsilon}_h(\boldsymbol{v}_h) - \int_{\Omega^{\mathrm{f},n}} p_h^n \mathrm{div}\, \boldsymbol{v}_h + \int_{\Omega^{\mathrm{f},n}} q_h \mathrm{div}\, \boldsymbol{u}_h^n \\ &+ s_h^{\mathrm{f}}(\boldsymbol{u}_h^{n-1} - \boldsymbol{w}_h^n; (\boldsymbol{u}_h^n, p_h^n), (\boldsymbol{v}_h, q_h)) \end{aligned}$$

incorporates Temam's trick, that is $\frac{\rho^{\mathrm{f}}}{2} \int_{\Omega^{\mathrm{f},n}} \mathrm{div}\,(\boldsymbol{u}_h^{n-1})\boldsymbol{u}_h^n \cdot \boldsymbol{v}_h$, to address the fact that the discrete fluid velocities are not exactly divergence-free. Additionally, it includes a stabilization term: one $\left(\frac{\rho^{\mathrm{f}}}{2} \int_{\Sigma^n} (\boldsymbol{u}_h^{n-1} - \dot{\boldsymbol{d}}_h^{n-\frac{1}{2}}) \cdot \boldsymbol{n}\boldsymbol{u}_h^n \cdot v_h\right)$ aimed at controlling the energy contribution coming from the convective term, and another $(s_h^{\mathrm{f}}(\boldsymbol{z}_h; (\boldsymbol{v}_h, q_h), (\boldsymbol{v}_h, q_h)) \geq 0,\ \forall (\boldsymbol{z}_h, \boldsymbol{v}_h, q_h) \in \boldsymbol{V}_h^{\mathrm{f}} \times \boldsymbol{V}_h^{\mathrm{f}} \times M_h^{\mathrm{f}})$, which represents an interior penalty approach, that is designed to enhance stability and robustness when dealing with high Reynolds numbers or when the inf-sup condition is not fully met [11, 56].

The algorithm could be adapted to include correction iterations, as in the linear setting, to improve the accuracy of the solution, and it can be found in Appendix B.

Algorithm 6.2 Loosely coupled scheme with Neumann-Robin interface conditions and mid-point scheme (LC-NR-MD) applied to the non linear problem

Given $\boldsymbol{u}_h^0, \boldsymbol{d}_h^{\mathrm{f},0}, \boldsymbol{d}_h^0, \dot{\boldsymbol{d}}_h^0, \boldsymbol{\lambda}_h^0$ and α, find $\forall n \geq 1$:

1. Solid subproblem: find $(\boldsymbol{d}_h^n, \dot{\boldsymbol{d}}_h^n) \in \boldsymbol{V}_h^{\mathrm{s}} \times \boldsymbol{V}_h^{\mathrm{s}}$, such that $\dot{\boldsymbol{d}}_h^{n-\frac{1}{2}} = \partial_\tau \boldsymbol{d}_h^n$ and

$$\rho^{\mathrm{s}} \int_{\Omega^{\mathrm{s}}} \partial_\tau \dot{\boldsymbol{d}}_h^n \cdot \boldsymbol{\xi}_h + \int_{\Omega^{\mathrm{s}}} \widetilde{\boldsymbol{\Sigma}}_h^{n-\frac{1}{2}} : \frac{1}{2}\left[(\boldsymbol{F}_h^{\mathrm{s},n-\frac{1}{2}})^{\mathrm{T}} \boldsymbol{\nabla}\boldsymbol{\xi}_h + (\boldsymbol{\nabla}\boldsymbol{\xi}_h)^{\mathrm{T}} \boldsymbol{F}_h^{\mathrm{s},n-\frac{1}{2}} \right] + \alpha \int_\Sigma (\dot{\boldsymbol{d}}^{n-\frac{1}{2}} - \widehat{\boldsymbol{u}}_h^{n-1}) \cdot \boldsymbol{\xi}_h = \int_\Sigma \boldsymbol{\lambda}_h^{n-\frac{3}{2}} \cdot \boldsymbol{\xi}_h$$

   for all $\boldsymbol{\xi}_h \in \boldsymbol{V}_h^{\mathrm{s}}$.

2. Solid-stress update: set $\boldsymbol{\lambda}_h^{n-\frac{1}{2}} \in \boldsymbol{V}_h^{\mathrm{g}}$ as

$$\boldsymbol{\lambda}_h^{n-\frac{1}{2}} = \boldsymbol{\lambda}_h^{n-\frac{3}{2}} + \alpha(\widehat{\boldsymbol{u}}^{n-1} - \dot{\boldsymbol{d}}^{n-\frac{1}{2}}) \quad \text{on } \Sigma.$$

3. Update fluid domain:

$$\boldsymbol{d}_h^{\mathrm{f},n} = \boldsymbol{\mathcal{L}}(\boldsymbol{d}_h^{n-1}|_\Sigma), \quad \boldsymbol{w}_h^n = \partial_\tau \boldsymbol{d}_h^{\mathrm{f},n}, \quad \boldsymbol{\mathcal{A}}_h^n = \boldsymbol{I}_{\Omega^{\mathrm{f}}} + \boldsymbol{d}_h^{\mathrm{f},n}, \quad \Omega^{\mathrm{f},n} = \boldsymbol{\mathcal{A}}_h^n(\Omega^{\mathrm{f}}).$$

4. Fluid subproblem: find $(\widehat{\boldsymbol{u}}_h^n, \widehat{p}_h^n) \in \boldsymbol{V}_h^{\mathrm{f}} \times M_h^{\mathrm{f}}$ such that

$$\frac{\rho^{\mathrm{f}}}{\tau}\left(\int_{\Omega^{\mathrm{f},n}} \boldsymbol{u}_h^n \cdot \boldsymbol{v}_h - \int_{\Omega^{\mathrm{f},n-1}} \boldsymbol{u}_h^{n-1} \cdot \boldsymbol{v}_h \right) + a_{\Omega^{\mathrm{f},n}}(\boldsymbol{u}_h^{n-1}, \boldsymbol{w}_h^n; (\boldsymbol{u}_h^n, p_h^n), (\boldsymbol{v}_h, q_h)) = -\int_\Sigma \boldsymbol{\lambda}^{n-\frac{1}{2}} \cdot \boldsymbol{v}_h$$

   for all $(\boldsymbol{v}_h, q_h) \in \boldsymbol{V}_h^{\mathrm{f}} \times M_h^{\mathrm{f}}$.

7 | Test cases and numerical results

Contents

This chapter presents the numerical implementation of the LC-NR-MD scheme (Algorithm 6.2) and the results for some more complex fluid-structure interaction problems. The results are provided for three test cases (2D inflating balloon, 2D lid-driven cavity and 3D elastic tube), each illustrating different aspects of the scheme's performance and accuracy.

7.1. Implementation details

For the implementation, we used the finite element library `FELiScE`[1] developed by COMMEDIA project team at Inria Paris. We used the Robin-Robin (LC-RR-MD) code as starting point, adapting it to our case. In order to promote code re-usability and fully leverage `FELiScE` and `MasterFSI` (an auxiliary library in `C++` that helps the communication between the solid and the fluid solver), the choice of mid-point time discretization in the solid discussed in the previous chapter was adopted, as this library was built to exchange the solid quantities evaluated at the mid-point in time.

The structure of the code consists in two separate solvers, one for the fluid and one for the solid. At each time step, the solid solver is called, receiving the velocity $\boldsymbol{u}^{n-1}$ and pressure p^{n-1} from the fluid solver and computes the displacement $\boldsymbol{d}^{n-\frac{1}{2}}$ and the velocity

[1] Finite Elements for LIfe SCiences and Engineering: `https://team.inria.fr/commedia/software/felisce/`

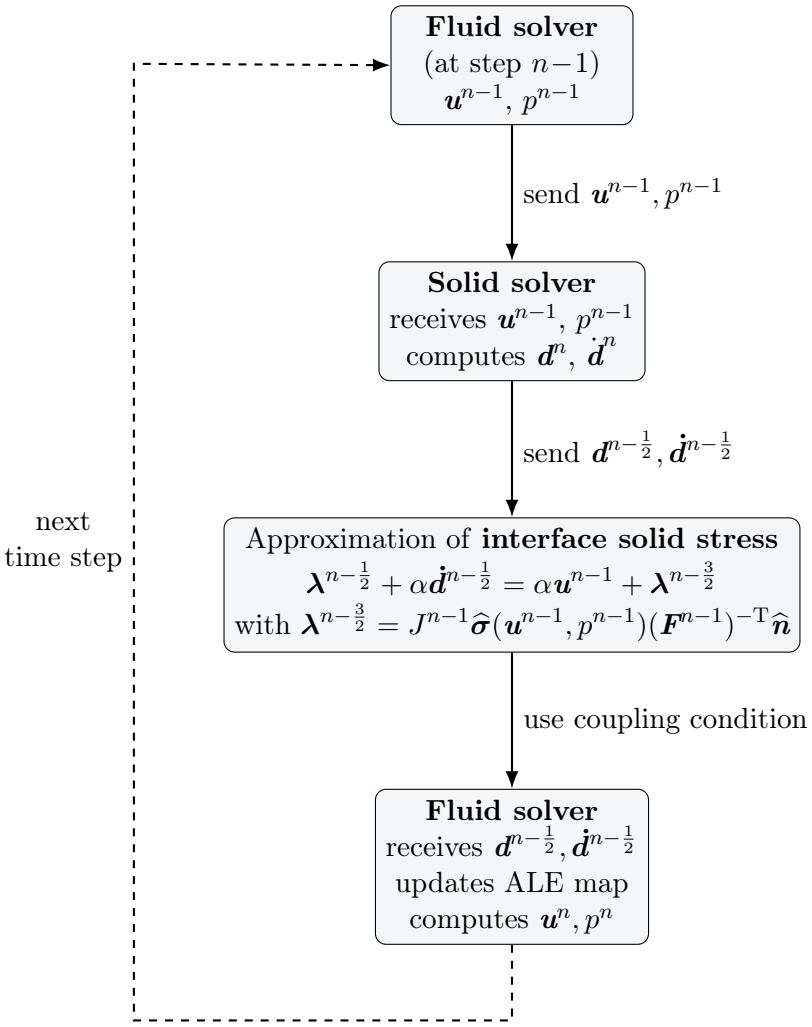

Figure 7.1: Flowchart of the communication beetween solid and fluid solver

$\dot{\boldsymbol{d}}^{n-\frac{1}{2}}$, which are then sent to the fluid solver. Then the fluid solver is called and uses the received displacement to update the ALE map and solve the Navier-Stokes equations in the moving domain.

In particular, we observe that in Algorithm 6.2, the solid stress $\boldsymbol{\lambda}^{n-\frac{1}{2}}$ appears in the coupling condition, but it is not actually computed or sent by the solid solver. To avoid modifying the library structure, we apply a simple trick: we approximate the previous interface stress by assuming we know $\boldsymbol{\lambda}^{n-\frac{3}{2}} = J^{n-1}\widehat{\boldsymbol{\sigma}}(\boldsymbol{u}^{n-1}, p^{n-1})(\boldsymbol{F}^{n-1})^{-\mathrm{T}}\widehat{\boldsymbol{n}}$. This leads to having the following coupling conditions:

$$\boldsymbol{\lambda}^{n-\frac{1}{2}} + \alpha\dot{\boldsymbol{d}}^{n-\frac{1}{2}} = \alpha\boldsymbol{u}^{n-1} + \boldsymbol{\lambda}^{n-\frac{3}{2}} \quad \text{on } \Sigma.$$

This coupling mimics the classical Robin-Robin approach, but avoids implicit coupling by using extrapolated fluid data from the previous time step.

Both the fluid and the solid solver use a "prenonly" approach, which means that the solvers that performs only one preconditioning step, without running more iterative solution cycles. The preconditioning step combined with LU factorization simplifies the problem.

7.2. Test cases

This section presents in more details the different test cases used to validate the proposed Neumann-Robin scheme. The physical parameters of the problems are summarized in Table 7.1. All the units are given in the SI system.

Case	ρ^{f} [kg/m^3]	μ [Pa·s]	ρ^{s} [kg/m^3]	E [Pa]	ν
Balloon 2D	1.1	0.1606	1000	7×10^5	0.45
Cavity 2D	1.0	0.01	250	250	0
Tube 3D	1000	0.0035	1200	3×10^5	0.3

Table 7.1: Physical parameters for the three different test cases (SI units)

The first two test cases do not involve added-mass effects, as their fluid and solid densities ratio is very large, while the third one might exhibit a significant added-mass effect as ρ^{f} and ρ^{s} are comparable.

In order to analyze the accuracy of the scheme, we want to perform a series of numerical tests, comparing the results obtained with LC-NR-MD (Algorithm 6.2) with the ones obtained using a strongly coupled approach. The latter is achieved performing a higher number of correction iterations or until convergence up to a fixed tolerance of 10^{-10}. We set the same time-step τ for all simulations of a specific test case, in order to ensure a fair comparison among the schemes.

7.2.1. 2D inflating balloon

We want to study a nonlinear fluid-structure interaction problem in a 2D domain shaped like a balloon, firstly introduced in [41]. The same problem but on a thin solid has been previously studied in [27]. The fluid domain Ω^{f} is a rectangular duct connected with a chamber of dimensions 3×3. The solid domain Ω^{s} outlines the chamber, with a thickness of $H_{\mathrm{s}} = 0.3$. The interface Σ is the boundary between the two domains, where the fluid and solid interact. For visibility reasons of the figure, the solid domain is represented with a bigger width than the computed one. A fluid velocity is imposed at the inlet boundary ($\max \boldsymbol{u}_{\mathrm{in}} = 1$). The spatial approximation is done using $\mathbb{P}_1/\mathbb{P}_1$ continuous finite elements

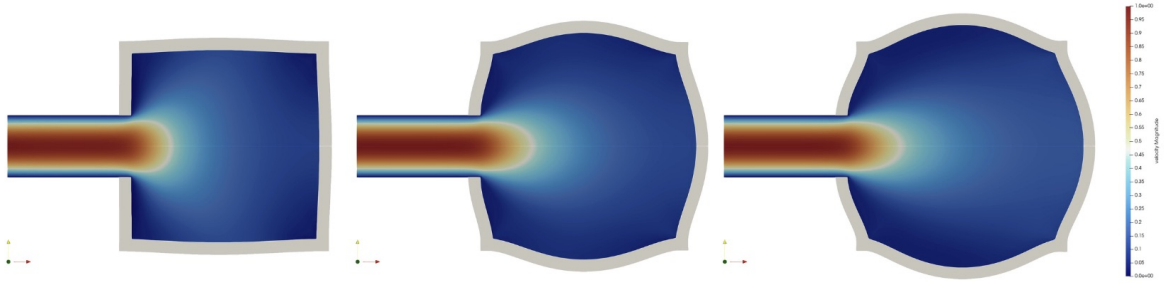

Figure 7.2: Balloon evolution, with LC-NR-MD (Algorithm 6.2 with $\alpha = 25, \tau = 10^{-3}$), at different time instances (from left to right: $t = 1$, $t = 5$, $t = 10$), highlighting the fluid velocity magnitude.

with SUPG stabilisation in the fluid.

Figure 7.2 shows the evolution of the balloon at different time instances, using the LC-NR-MD scheme (Algorithm 6.2). The fluid velocity magnitude is highlighted.

First of all, we plotted the time history of the mid-point solid displacement, using the Neumann-Robin scheme, comparing different values of α for a fixed timestep. The results are shown in Figure 7.3, which includes the LC-RR-MD scheme for comparison (Algorithm A.3). We can see that the choice of α is crucial for the accuracy of the solution. In particular, we observe that for small values of α, the solutions is far off from the monolithic one. We only plotted the values of α that satisfy the stability condition (3.9), since the others (e.g. $\alpha = 50$) lead to instabilities so severe and immediate that they crash the program, making it pointless to include them in the plots.

Through this numerical experiments, we observe that the solution obtained with the Neumann-Robin scheme is not able to reach the same accuracy as the Robin-Robin scheme, even for high values of α. This effect could be circumvented by decreasing the time-step τ, but this would lead to a significant increase in the computational cost.

For different values of the Robin parameter, we performed a series of tests increasing the number of correction iterations. The results are shown in Figure 7.4 for one specific value of $\alpha = 6.25$. We observe that a higher number of correction iterations leads to a more accurate solution, as shown also from Table 7.2. The table reports the L^2-differences between the time history of the average solid displacement obtained with the reversed RN scheme and the one obtained with the monolithic solver. In all cases, we observe that the L^2-difference decreases as we increase α. We note that the symbol '`X`' is used in the table to indicate cases where the method did not converge. This lack of convergence is attributed to values of α lying near the stability limit of the scheme.

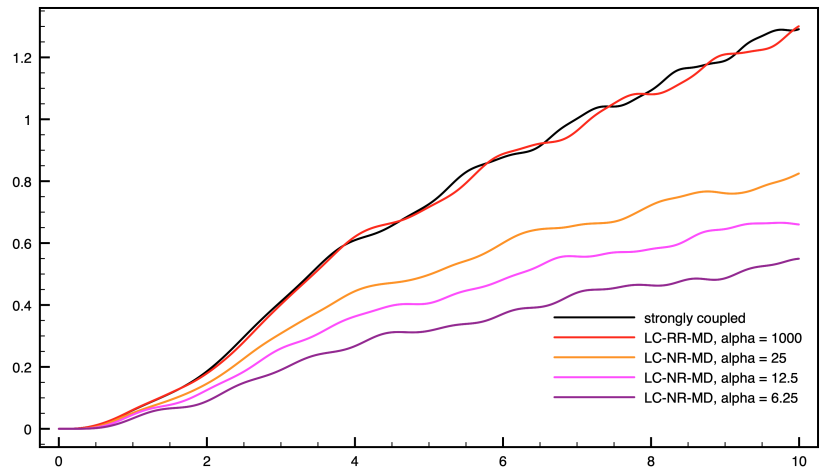

Figure 7.3: Comparison of the time histories of the solid displacement for the balloon test case, using LC-NR-MD (Algorithm 6.2 with $\tau = 10^{-3}$), the LC-RR-MD (Algorithm A.3) comparing different values of α.

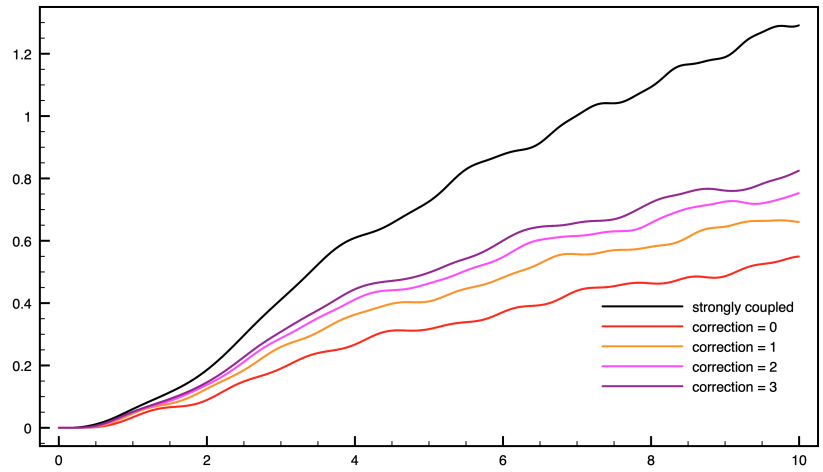

Figure 7.4: Comparison of the time histories of the solid displacement for the balloon test case, using LC-NR-MD-CI scheme (Algorithm B.3 with $\alpha = 6.25$ and $\tau = 10^{-3}$), with different correction iterations.

Correction iterations	$\alpha = 6.25$	$\alpha = 12.5$	$\alpha = 25$
$K = 0$	0.5743	0.4545	0.3420
$K = 1$	0.4545	0.3420	X
$K = 2$	0.3883	0.2801	X
$K = 3$	0.3419	X	X

Table 7.2: L^2-difference between the time history of the average solid displacement obtained with the LC-NR-MD-CI scheme (Algorithm B.3) and the one obtained with the monolithic solver (Algorithm 6.1) on the balloon test case.

7.2.2. 2D lid-driven cavity

For the second test case, we want to analyze is the 2D lid-driven cavity problem [14, 31]. It consists in a unit square domain $\Omega^f = [0,1] \times [0,1]$ where the top lid is moving to the right, creating a shear flow in the fluid, that makes the elastic bottom wall deform. Differently from the previous cases, the solid domain is now thin: we replace the solid subproblem in (6.2) with a nonlinear Timoshenko beam. At the initial time, the overall system is at rest. An horizontal velocity $\boldsymbol{u}(t) = (1 - \cos(0.4\pi t); 0)$ is imposed on the top lid. A no-slip condition is imposed on a portion of the left and right walls $\{0,1\} \times [0, 0.9]$, while on the remaining parts, a zero traction is applied. The spatial approximation is done using $\mathbb{P}_1/\mathbb{P}_1$ continuous finite elements with SUPG stabilization in the fluid.

Figure 7.5 shows the evolution of the cavity at different time instances, using the Neumann-Robin scheme (Algorithm 6.2). The fluid velocity magnitude is highlighted.

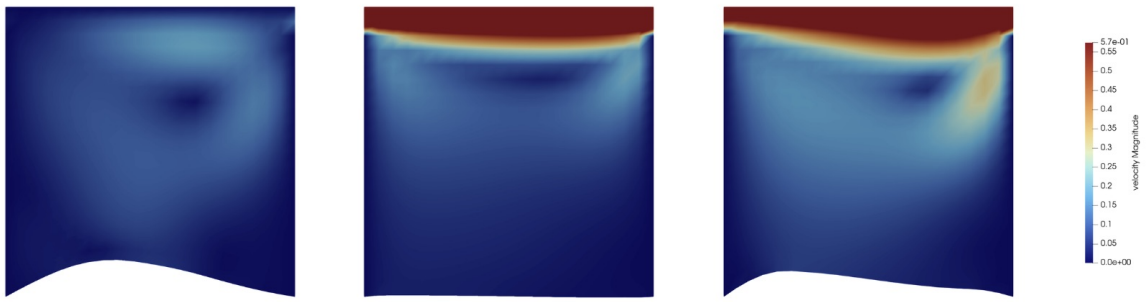

Figure 7.5: Cavity evolution, with LC-NR-MD (Algorithm 6.2 with $\alpha = 0.1, \tau = 0.1$), at different time instances (from left to right: $t = 0.2$, $t = 0.37$, $t = 0.5$), highlighting the fluid velocity.

Figures 7.6 shows the time history of the average solid displacement, comparing different values of α, while Figure 7.7 reports the results when performing a few correction iterations. The L^2-differences of the errrors are reported in Table 7.3.

In this test case, contrary to the previous ones, the Neumann-Robin scheme is able to reach a overall better accuracy, having lower L^2-differences. This could be explained by the fact that the physical parameter of the problem, Young's modulus E, is significantly lower than the ones used for the balloon and the tube. This result is consistent with the findings presented in Figure 5.12, where we observed the same behavior.

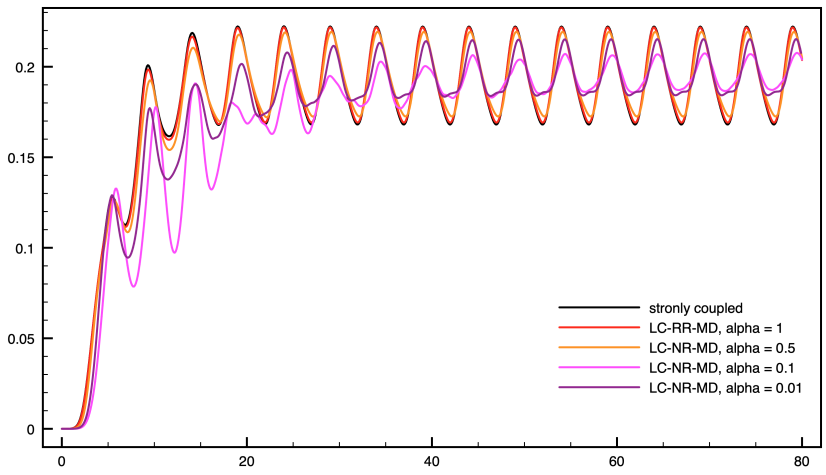

Figure 7.6: Time history of the solid displacement for the cavity test cases, using the LC-NR-MD scheme (Algorithm 6.2 with $\tau = 0.1$) and LC-RR-MD (Algorithm A.3), comparing different values of α.

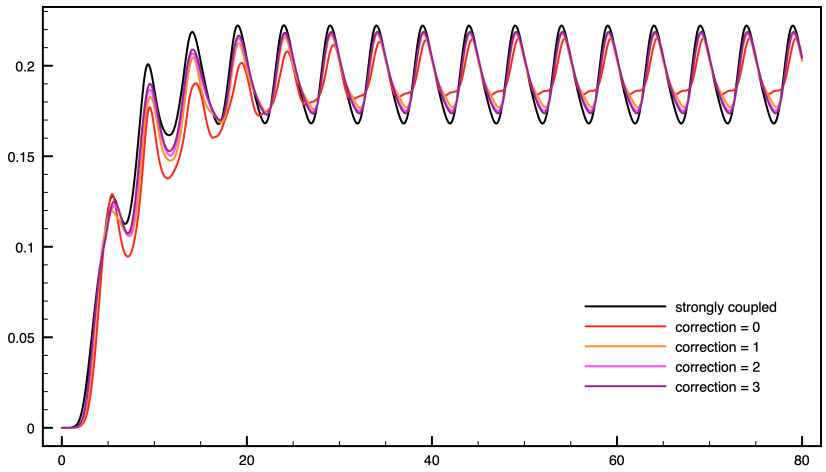

Figure 7.7: Time history of the solid displacement for the cavity test cases, using the LC-NR-MD-CI scheme (Algorithm B.3 with $\alpha = 0.1$ and $\tau = 0.1$) with different correction iterations.

Correction iterations	$\alpha = 0.05$	$\alpha = 0.1$	$\alpha = 0.5$
$K = 0$	0.1224	0.0738	0.0237
$K = 1$	0.0736	0.0442	0.0149
$K = 2$	0.0555	0.0327	X
$K = 3$	0.0442	0.0268	X

Table 7.3: L^2-difference between the time history of the average solid displacement obtained with the LC-NR-MD-CI scheme (Algorithm B.3) and the one obtained with the monolithic solver (MONO-BDF1, Algorithm 6.1) on the cavity test case.

7.2.3. 3D elastic tube

The last test case is the simulation of a pressure wave through a straight elastic tube [29, Chapter 13], representing the 3D counterpart of the problem treated in the first part of the report. The problem is defined in a cylindrical domain of length 5 and radius 0.5, where the fluid flows through a tube with a solid elastic wall, of height 0.1. The systems starts from a stationary state. A pressure of $1.3322 \cdot 10^4$ is applied at the inlet boundary in the time frame $[0, 5 \cdot 10^{-3}]$ seconds. The solid wall is clamped at the outlet boundary, while the other boundaries are set to no-slip conditions. The spatial approximation is done using $\mathbb{P}_1/\mathbb{P}_1$ continuous finite elements with SUPG stabilization in the fluid.

Figure 7.8 shows the evolution of the tube at different time instances, using the reversed Robin-Neumann scheme (Algorithm 6.2). The fluid pressure is highlighted. For visualization purposes, the solid displacement is scaled by a factor of 5.

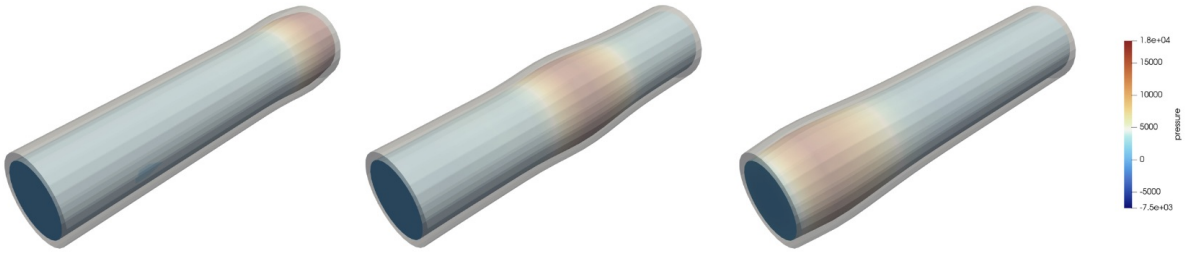

Figure 7.8: Tube evolution, with LC-NR-MD scheme (Algorithm 6.2 with $\alpha = 200, \tau = 10^{-4}$), at different time instances (from left to right: $t = 0.03$, $t = 0.08$, $t = 0.13$), highlighting the fluid pressure.

As the previous test case, we want to analyze the accuracy of the scheme: the time history of the solid displacement is plotted in Figure 7.9, comparing different values of α for a fixed timestep. As the balloon test case, we can see that the choice of α is crucial, but we still don't have the same accuracy as the Robin-Robin scheme. Figure 7.10 reports the results when performing a few correction iterations, while the L^2-differences are reported in Table 7.4. This behavior is a good indication that the Neumann-Robin scheme is able to solve numerical problems under the influence of large added-mass effects.

Overall, the numerical experiments confirm that the proposed LC-NR-MD scheme provides stable results across a range of FSI configurations, with its performance strongly influenced by the choice of the Robin parameter, highlighting the trade-off between computational efficiency and accuracy compared to fully implicit approaches or other loosely coupled approaches.

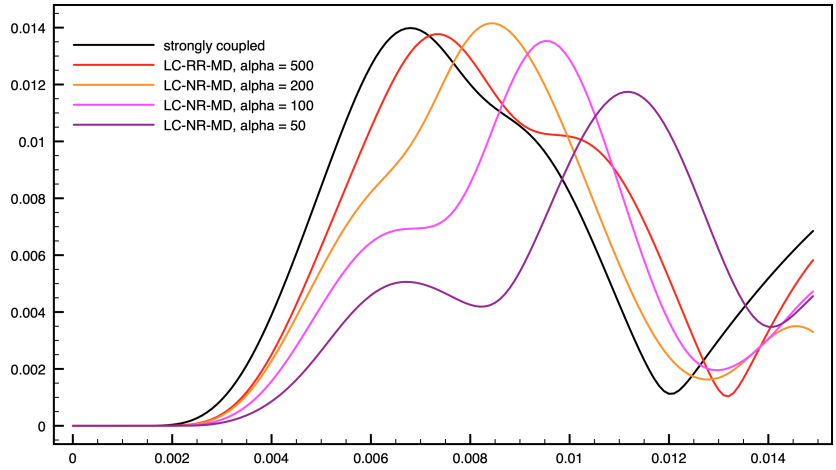

Figure 7.9: Comparison of the time histories of the solid displacement for the tube test case, using LC-NR-MD scheme (Algorithm 6.2 with $\tau = 10^{-4}$) and LC-RR-MD (Algorithm A.3), comparing different values of α.

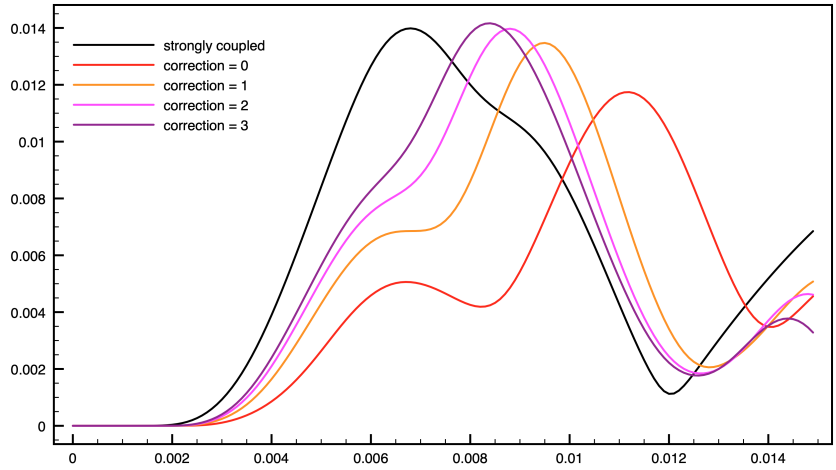

Figure 7.10: Time history of the solid displacement for the tube test cases, using the LC-NR-MD-CI (Algorithm B.3 with $\alpha = 50$ and $\tau = 10^{-4}$) with different correction iterations.

Correction iterations	$\alpha = 50$	$\alpha = 100$	$\alpha = 200$
$K = 0$	0.7149	0.4637	0.2921
$K = 1$	0.4518	0.2662	X
$K = 2$	0.3327	X	X
$K = 3$	0.2739	X	X

Table 7.4: L^2-difference between the time history of the average solid displacement obtained with the LC-NR-MD-CI (Algorithm B.3) and the one obtained with the monolithic solver (Algorithm 6.1) on the tube test case.

8 | Conclusions and future developments

This thesis focused on the numerical analysis of Robin-based loosely coupled schemes for fluid-structure interaction, to allow for the possibility of using separate solvers. We provided a detailed analysis for the stability and convergence in regimes involving large added mass effects.

We started with the classical Robin-Neumann scheme and we continued presenting a reversing strategy: the Neumann-Robin scheme, which represents the main study of this thesis. In the latter, the solid subproblem is solved with a Robin boundary condition and the fluid with a Neumann condition. For both schemes we derived a stability criteria, using energy-based arguments. The Robin-Neumann scheme has been shown to be stable for a wide range of Robin parameters for BDF1, under a CFL-like condition, while the choice of mid-point scheme in the solid resulted unconditionally unstable. On the other hand, the Neumann-Robin scheme appears to be less robust with respect to the Robin parameter, having a smaller range of appropriate α, but it results conditionally stable for both BDF1 and mid-point in the solid. Contrary to classical intuition, this reversal imposes an additional numerical damping effect on the solid velocities analogous to viscous damping, enhancing energy dissipation exclusively on the solid side. In both cases, the schemes are more accurate as the value of α increases, marking a significant difference with the Robin-Robin scheme, where α cannot be too large nor too small.

All the theoretical findings have been checked with standard benchmarks in `FreeFem++` and `FELiScE`. They also show that both schemes are able to achieve optimal accuracy, but the choice of α is highly crucial in the accuracy of the solution, as well as the value of τ. In fact, for the 2D balloon and the 3D tube, the reversed Robin-Neumann scheme struggles to reach the same accuracy as the Robin-Robin scheme when the time-step τ is not sufficiently small. Another key aspect is the number of correction iterations, that along with the choice of α, play a crucial role in improving the accuracy of the solution.

The present work can be developed and improved with the followings:

- Axisymmetric configurations: it can be interesting to modify and extend the linear formulation into an axisymmetric formulation. This helps reduce a 3D formulation to a 2D case, by assuming that variables only depend on the radial and axial coordinates, not on the angular coordinate. In the context of this thesis, extending the formulation to be axisymmetric means adapting and correcting the numerical and mathematical model to accurately reflect the physics under this symmetry assumption;
- More complex simulations: FSI problems that are encountered in nature often involve domains that are much more complex to the ones we addressed in this thesis. For instance, in the field of haemodynamics, simulating heart valves, which interact with moving leaflets represents a more realistic and challenging scenario;
- Improved optimization of the Robin parameters: another crucial improvement could be done on the calibration of the Robin parameter α. In this thesis, we have employed a formulation to determine the optimal value based on a strongly coupled method applied to a potential flow model, which is simpler than the more complex scenarios studied here. Future work might be dedicated to studying a better way to find this parameter in 3D cases.

Bibliography

[1] S. Badia, F. Nobile, and C. Vergara. Fluid–structure partitioned procedures based on Robin transmission conditions. *Journal of Computational Physics*, 227(14):7027–7051, 2008. doi: 10.1016/j.jcp.2008.04.006. URL https://doi.org/10.1016/j.jcp.2008.04.006.

[2] S. Badia, F. Nobile, and C. Vergara. Robin–Robin preconditioned krylov methods for fluid–structure interaction problems. *Computer Methods in Applied Mechanics and Engineering*, 198(33):2768–2784, 2009. ISSN 0045-7825. doi: https://doi.org/10.1016/j.cma.2009.04.004. URL https://www.sciencedirect.com/science/article/pii/S0045782509001546.

[3] A. T. Barker and X.-C. Cai. Scalable parallel methods for monolithic coupling in fluid–structure interaction with application to blood flow modeling. *Journal of Computational Physics*, 229(3):642–659, 2010. ISSN 0021-9991. doi: https://doi.org/10.1016/j.jcp.2009.10.001. URL https://www.sciencedirect.com/science/article/pii/S0021999109005464.

[4] L. Bennati, C. Vergara, M. Domanin, C. Malloggi, D. Bissacco, S. Trimarchi, V. Silani, G. Parati, and R. Casana. A computational fluid structure interaction study for carotids with different atherosclerotic plaques. *Journal of Biomechanical Engineering*, 143(9):091002, 2021. doi: 10.1115/1.4050910. URL https://doi.org/10.1115/1.4050910.

[5] S. Biswas and D. Chakraborty. Aeroelastic flutter analysis of a supersonic wing with multiple external stores. *International Journal of Mechanical and Production Engineering Research and Development*, 4(2):1–10, 2014. doi: 10.31436/iiumej.v15i2.524.

[6] S. C. Brenner and L. R. Scott. *The Mathematical Theory of Finite Element Methods*, volume 15 of *Texts in Applied Mathematics*. Springer, 3rd edition, 2007. ISBN 9780387759333. doi: 10.1007/978-0-387-75934-0.

[7] F. Brezzi and J. Pitkäranta. On the stabilization of finite element approximations of

the stokes equations. In W. Hackbusch, editor, *Efficient Solutions of Elliptic Systems*, volume 10 of *Notes on Numerical Fluid Mechanics*, pages 11–19. Vieweg+Teubner Verlag, Wiesbaden, 1984. doi: 10.1007/978-3-663-14169-3_2.

[8] M. Bucelli, M. Gabriel, A. Quarteroni, G. Gigante, and C. Vergara. A stable loosely-coupled scheme for cardiac electro-fluid-structure interaction. *Journal of Computational Physics*, 490:112326, 2023.

[9] E. Burman and M. A. Fernández. Stabilization of explicit coupling in fluid-structure interaction involving fluid incompressibility. *Computer Methods in Applied Mechanics and Engineering*, 198(5–8):766–784, 2009. doi: 10.1016/j.cma.2008.10.012.

[10] E. Burman and M. A. Fernández. Explicit strategies for incompressible fluid-structure interaction problems: Nitsche type mortaring versus Robin-Robin coupling. *International Journal for Numerical Methods in Engineering*, 97(10):739–758, 2014. ISSN 0249-6399. doi: 10.1002/nme.4607. URL `https://doi.org/10.1002/nme.4607`.

[11] E. Burman, M. A. Fernández, and P. Hansbo. Continuous interior penalty finite element method for Oseen's equations. *SIAM Journal on Numerical Analysis*, 44(3): 1248–1274, 2006.

[12] E. Burman, R. H. W. Hoppe, and J. Guzmán. Stability and error analysis of a splitting method using Robin-Robin coupling applied to a fluid-structure interaction problem. *arXiv e-prints*, 2019.

[13] E. Burman, R. Durst, M. A. Fernández, J. Guzmán, and O. Ruz. Robin-Robin loose coupling for incompressible fluid-structure interaction: non-linear setting and nearly-optimal error analysis. *Preprint*, 2021. URL `https://hal.science/hal-02893444v1`.

[14] E. Burman, R. Durst, M. A. Fernández, and J. Guzmán. Fully discrete loosely coupled Robin-Robin scheme for incompressible fluid-structure interaction: stability and error analysis. *Numerische Mathematik*, 151(4):807–840, 2022. doi: 10.1007/s00211-022-01295-y.

[15] D. Carbonaro, F. Mezzadri, N. Ferro, G. D. Nisco, A. Audenino, D. Gallo, C. Chiastra, U. Morbiducci, and S. Perotto. Design of innovative self-expandable femoral stents using inverse homogenization topology optimization. *Comput. Methods Appl. Mech. Engrg.*, 416:116288, 2023. doi: 10.1016/j.cma.2023.116288. URL `https://doi.org/10.1016/j.cma.2023.116288`.

[16] P. Causin, J.-F. Gerbeau, and F. Nobile. Added-mass effect in the design of parti-

tioned algorithms for fluid-structure problems. *Computer Methods in Applied Mechanics and Engineering*, 194(42-44):4506–4527, 2005.

[17] A. J. Chorin. Numerical solutions of the navier-stokes equations. *Mathematics of Computation*, 22:745–762, 1968.

[18] S. Deparis, M. Discacciati, G. Fourestey, and A. Quarteroni. Fluid–structure algorithms based on steklov–poincaré operators. *Computer Methods in Applied Mechanics and Engineering*, 195(41–43):5797–5812, 2006. doi: 10.1016/j.cma.2006.03.018.

[19] J. Donea, A. Giuliani, and J.-P. Halleux. An arbitrary lagrangian–eulerian finite element method for transient dynamic fluid–structure interactions. *Computer Methods in Applied Mechanics and Engineering*, 33(1-3):689–723, 1982. doi: 10.1016/0045-7825(82)90128-1.

[20] R. Durst. *Recent advances in splitting methods based on Robin–Robin coupling conditions*. PhD thesis, Brown University, 2022. URL `https://repository.library.brown.edu/studio/item/bdr:v34deskr/`.

[21] C. Farhat, M. Lesoinne, and P. LeTallec. Load and motion transfer algorithms for fluid/structure interaction problems with non-matching discrete interfaces: momentum and energy conservation, optimal discretization and application to aeroelasticity. *Computer Methods in Applied Mechanics and Engineering*, 157(1-2):95–114, 1998.

[22] A. Fasano and A. Sequeira. *Hemomath: The Mathematics of Blood*, volume 18 of *MS&A – Modeling, Simulation and Applications*. Springer International Publishing, 2017. ISBN 978-3-319-60512-8. doi: 10.1007/978-3-319-60513-5. URL `https://doi.org/10.1007/978-3-319-60513-5`.

[23] M. A. Fernández and M. Moubachir. An exact block-Newton algorithm for solving fluid–structure interaction problems. *Comptes Rendus Mathematique*, 336(8):681–686, 2003. doi: 10.1016/S1631-073X(03)00136-1.

[24] M. A. Fernández and M. Moubachir. A Newton method using exact Jacobians for solving fluid–structure coupling. *Computers & Structures*, 83(2-3):127–142, 2005. doi: 10.1016/j.compstruc.2004.04.021.

[25] M. A. Fernández and J. Mullaert. Convergence and error analysis for a class of splitting schemes in incompressible fluid-structure interaction. *IMA Journal of Numerical Analysis*, 36(4):1748–1782, 2016.

[26] M. A. Fernández, J.-F. Gerbeau, and C. Grandmont. A projection semi-implicit

scheme for the coupling of an elastic structure with an incompressible fluid. Technical Report RR-5700, INRIA, 2005. URL https://hal.inria.fr/inria-00070315.

[27] M. A. Fernández, M. Landajuela, J. Mullaert, and M. Vidrascu. Robin-Neumann schemes for incompressible fluid-structure interaction. In *Domain Decomposition Methods in Science and Engineering XXII*, pages 65–76, Lugano, Switzerland, 2015. Springer. doi: 10.1007/978-3-319-18827-0_6. URL https://hal.science/hal-01113088.

[28] M. A. Fernández, J. Mullaert, and M. Vidrascu. Generalized Robin–Neumann explicit coupling schemes for incompressible fluid-structure interaction: Stability analysis and numerics. *International Journal for Numerical Methods in Engineering*, 101(3):199–229, 2015. doi: 10.1002/nme.4785. URL https://doi.org/10.1002/nme.4785.

[29] L. Formaggia, A. Quarteroni, and A. Veneziani, editors. *Cardiovascular Mathematics: Modeling and Simulation of the Circulatory System*. MS&A: Modeling, Simulation and Applications. Springer-Verlag Italia, Milan, Berlin, Heidelberg, New York, 2009. ISBN 978-88-470-1151-9. URL https://www.springer.com/gp/book/9788847011519. Library of Congress Control Number: 2008943078.

[30] L. Formaggia, A. Quarteroni, and C. Vergara. On the physical consistency between three-dimensional and one-dimensional models in haemodynamics. *Journal of Computational Physics*, 244:97–112, 2013. ISSN 0021-9991. doi: https://doi.org/10.1016/j.jcp.2012.08.001. URL https://www.sciencedirect.com/science/article/pii/S0021999112004342. Multi-scale Modeling and Simulation of Biological Systems.

[31] C. Förster, W. A. Wall, and E. Ramm. Artificial added mass instabilities in sequential staggered coupling of nonlinear structures and incompressible viscous flows. *Computer Methods in Applied Mechanics and Engineering*, 196(7):1278–1293, 2007.

[32] M. W. Gee, U. Kuttler, and W. A. Wall. Truly monolithic algebraic multigrid for fluid–structure interaction. *International Journal for Numerical Methods in Engineering*, 85(8):987–1016, 2011. doi: 10.1002/nme.3068.

[33] L. Gerardo-Giorda, F. Nobile, and C. Vergara. Analysis and optimization of Robin–Robin partitioned procedures in fluid–structure interaction problems. *SIAM Journal on Numerical Analysis*, 48(6):2091–2116, 2010. doi: 10.1137/09075280X.

[34] J.-F. Gerbeau and M. Vidrascu. A quasi-Newton algorithm based on a reduced model for fluid–structure interaction problems in blood flows. *Mathematical Modelling and Numerical Analysis*, 37(4):631–648, 2003. doi: 10.1051/m2an:2003036.

[35] G. Gigante and C. Vergara. Optimized schwarz methods for the coupling of cylindrical geometries along the axial direction. *ESAIM: Mathematical Modelling and Numerical Analysis (M2AN)*, 52(5):1597–1615, 2018. doi: 10.1051/m2an/2018039.

[36] G. Gigante and C. Vergara. On the stability of a loosely-coupled scheme based on a Robin interface condition for fluid-structure interaction. *Computers & Mathematics with Applications*, 96:109–119, 2021. doi: 10.1016/j.camwa.2021.05.012.

[37] G. Gigante and C. Vergara. On the choice of interface parameters in Robin–Robin loosely coupled schemes for fluid–structure interaction. *Fluids*, 6(6):213, 2021. doi: 10.3390/fluids6060213. URL `https://www.mdpi.com/2311-5521/6/6/213`.

[38] M. Heil. An efficient solver for the fully coupled solution of large-displacement fluid–structure interaction problems. *Computer Methods in Applied Mechanics and Engineering*, 193:1–23, 2004. doi: 10.1016/j.cma.2003.09.006.

[39] J. Heywood and R. Rannacher. Finite-Element approximation of the non-stationary Navier-Stokes problem. iv. error analysis for second-order time discretization. *SIAM Journal on Numerical Analysis*, 27(2):353–384, 1990.

[40] E. H. Hirt, A. A. Amsden, and J. L. Cook. An arbitrary lagrangian–eulerian computing method for all flow speeds. *Journal of Computational Physics*, 14(3):227–253, 1974. doi: 10.1016/0021-9991(74)90051-0.

[41] U. Küttler, C. Förster, and W. A. Wall. A solution for the incompressibility dilemma in partitioned fluid–structure interaction with pure Dirichlet fluid domains. *Computational Mechanics*, 38(4):417–429, 2006. doi: 10.1007/s00466-006-0066-5.

[42] A. Larsen et al. Multimodal flutter of a long-span suspension bridge in service and during construction. *Journal of Wind Engineering and Industrial Aerodynamics*, 227: 105072, 2022. doi: 10.1016/j.jweia.2022.105072.

[43] P. Le Tallec and J. Mouro. Fluid structure interaction with large structural displacements. *Computer Methods in Applied Mechanics and Engineering*, 190(24):3039–3067, 2001. ISSN 0045-7825. doi: https://doi.org/10.1016/S0045-7825(00)00381-9. URL `https://www.sciencedirect.com/science/article/pii/S0045782500003819`. Advances in Computational Methods for Fluid-Structure Interaction.

[44] B. Li, W. Sun, Y. Xie, and W. Yu. Optimal L^2 error analysis of a loosely coupled finite element scheme for thin-structure interactions. *SIAM Journal on Numerical Analysis*, 62(4):1782–1813, 2024. doi: 10.1137/23M1578401.

[45] F. Nobile and C. Vergara. An effective fluid-structure interaction formulation for vascular dynamics by generalized robin conditions. *SIAM Journal on Scientific Computing*, 30:731–763, 02 2008. doi: 10.1137/060678439.

[46] F. Nobile, M. Pozzoli, and C. Vergara. Time accurate partitioned algorithms for the solution of fluid–structure interaction problems in haemodynamics. *Computers & Fluids*, 86:470–482, 2013. ISSN 0045-7930. doi: https://doi.org/10.1016/j.compfluid.2013.07.031. URL `https://www.sciencedirect.com/science/article/pii/S0045793013003101`.

[47] A. Quaini and A. Quarteroni. A semi-implicit approach for fluid–structure interaction based on an algebraic fractional step method. *Mathematical Models and Methods in Applied Sciences*, 17(6):957–983, 2007. doi: 10.1142/S0218202507002206.

[48] A. Quarteroni. *Numerical Models for Differential Problems*. Springer, 2018.

[49] A. Quarteroni, F. Saleri, and A. Veneziani. Analysis of the Yosida method for the incompressible navier–stokes equations. *Journal de Mathématiques Pures et Appliquées*, 78(5):473–503, 1999. ISSN 0021-7824. doi: https://doi.org/10.1016/S0021-7824(99)00027-6. URL `https://www.sciencedirect.com/science/article/pii/S0021782499000276`.

[50] A. Quarteroni, A. Manzoni, and C. Vergara. The cardiovascular system: Mathematical modelling, numerical algorithms and clinical applications. *Acta Numerica*, 26:365–590, 2017. doi: 10.1017/S0962492917000046.

[51] P. Raback, J. Ruokolainen, M. Lyly, and E. Järvinen. Fluid-structure interaction boundary conditions by artificial compressibility. In *ECCOMAS Computational Fluid Dynamics Conference*, Swansea, 2001.

[52] W. Rudin. *Principles of Mathematical Analysis*. McGraw-Hill, New York, 3rd edition, 1976. ISBN 978-0070542358.

[53] L. R. Scott and S. Zhang. Finite Element interpolation of nonsmooth functions satisfying boundary conditions. *Mathematics of Computation*, 54(190):483–493, 1990. doi: 10.2307/2008497. URL `https://www.jstor.org/stable/2008497`.

[54] W. Sun and W. Yu. Optimal error estimates of a 1.5-order stabilized Robin–Neumann scheme for fluid–structure interaction with thin solids. *SIAM Journal on Numerical Analysis*, 2025. To appear.

[55] R. Temam. Une méthode d'approximation de la solution des équations de navier-stokes. *Bulletin de la Société Mathématique de France*, 96:115–152, 1968.

[56] T. E. Tezduyar. Stabilized finite element formulations for incompressible flow computations. *Advances in Applied Mechanics*, 28:1–44, 1991. doi: 10.1016/S0065-2156(08)70153-4.

[57] T. E. Tezduyar. Finite element methods for fluid dynamics with moving boundaries and interfaces. *Archives of Computational Methods in Engineering*, 8:83–130, 2001. doi: 10.1007/BF02736262.

[58] V. Thomée. *Galerkin Finite Element Methods for Parabolic Problems*, volume 25 of *Springer Series in Computational Mathematics*. Springer-Verlag Berlin Heidelberg, Berlin, Heidelberg, second edition edition, 2006. ISBN 978-3-540-33121-6. doi: 10.1007/3-540-33122-0.

[59] E. H. van Brummelen. Added mass effects of compressible and incompressible flows in fluid-structure interaction. *Journal of Applied Mechanics*, 76(2):021206–1–021206–7, 2009. doi: 10.1115/1.3057494.

[60] K. F. Warnick. *Numerical Analysis for Electromagnetic Integral Equations*. Artech House, Norwood, MA, 2008. ISBN 978-1-59693-333-0.

[61] S. Zhao, W. Wu, S. Samant, and et al. Patient-specific computational simulation of coronary artery bifurcation stenting. *Scientific Reports*, 11:16486, 2021. doi: 10.1038/s41598-021-95026-2. URL `https://doi.org/10.1038/s41598-021-95026-2`.

A | Robin-Robin loosely coupled schemes

In this appendix, Algorithms A.1 and A.2 report the fully discrete formulations of the Robin-Robin scheme (see [13, 14]). We use the following notation

$$\partial_\tau f^n := \frac{f^n - f^{n-1}}{\tau}, \qquad f^{n-\frac{1}{2}} := \frac{f^n + f^{n-1}}{2},$$

where f is a generic variable.

We also report below in Algorithm A.3 the LC-RR-MD applied to the nonlinear problem (see Algorithm 1 in [13]).

Algorithm A.1 Loosely coupled scheme with Robin-Robin interface conditions and BDF1 time discretization (LC-RR-BDF1)

Given $\boldsymbol{u}_h^0, \boldsymbol{d}_h^0, \dot{\boldsymbol{d}}_h^0, \boldsymbol{\lambda}_h^0$ and α, $\forall n \geq 1$:

1. Solid subproblem: find $(\boldsymbol{d}_h^n, \dot{\boldsymbol{d}}_h^n) \in \boldsymbol{V}_h^{\mathrm{s}} \times \boldsymbol{V}_h^{\mathrm{s}}$, such that $\dot{\boldsymbol{d}}_h^n = \partial_\tau \boldsymbol{d}_h^n$ and

$$\rho^{\mathrm{s}} \int_{\Omega^{\mathrm{s}}} \partial_\tau \dot{\boldsymbol{d}}_h^n \cdot \boldsymbol{\xi}_h + a^{\mathrm{s}}(\boldsymbol{d}_h^n, \boldsymbol{\xi}_h) + \alpha \int_\Sigma (\dot{\boldsymbol{d}}_h^n - \boldsymbol{u}_h^{n-1}) \cdot \boldsymbol{\xi}_h = -\int_\Sigma \boldsymbol{\lambda}_h^{n-1} \cdot \boldsymbol{\xi}_h$$

   for all $\boldsymbol{\xi}_h \in \boldsymbol{V}_h^{\mathrm{s}}$.

2. Fluid subproblem: find $(\boldsymbol{u}_h^n, p_h^n) \in \boldsymbol{V}_h^{\mathrm{f}} \times M_h^{\mathrm{f}}$ such that

$$\rho^{\mathrm{f}} \int_{\Omega^{\mathrm{f}}} \partial_\tau \boldsymbol{u}_h^n \cdot \boldsymbol{v}_h + a_h^{\mathrm{f}}((\boldsymbol{u}_h^n, p_h^n), (\boldsymbol{v}_h, q_h)) + \alpha \int_\Sigma (\boldsymbol{u}_h^n - \dot{\boldsymbol{d}}_h^{n-1}) \cdot \boldsymbol{v}_h = \int_\Sigma \boldsymbol{\lambda}_h^{n-1} \cdot \boldsymbol{v}_h$$

   for all $(\boldsymbol{v}_h, q_h) \in \boldsymbol{V}_h^{\mathrm{f}} \times M_h^{\mathrm{f}}$.

3. Fluid-stress update: set $\boldsymbol{\lambda}_h^n \in \boldsymbol{V}_h^{\mathrm{g}}$ as

$$\boldsymbol{\lambda}_h^n = \boldsymbol{\lambda}_h^{n-1} + \alpha(\dot{\boldsymbol{d}}_h^{n-1} - \boldsymbol{u}_h^n) \quad \text{on } \Sigma.$$

Algorithm A.2 Loosely coupled scheme with Robin-Robin interface conditions and midpoint time discretization (LC-RR-MD)

Given $\boldsymbol{u}_h^0, \boldsymbol{d}_h^0, \dot{\boldsymbol{d}}_h^0, \boldsymbol{\lambda}_h^0$ and α, $\forall n \geq 1$:

1. Solid subproblem: find $(\boldsymbol{d}_h^n, \dot{\boldsymbol{d}}_h^n) \in \boldsymbol{V}_h^{\mathrm{s}} \times \boldsymbol{V}_h^{\mathrm{s}}$, such that $\dot{\boldsymbol{d}}_h^n = \partial_\tau \boldsymbol{d}_h^n$ and

$$\rho^{\mathrm{s}} \int_{\Omega^{\mathrm{s}}} \partial_\tau \dot{\boldsymbol{d}}_h^n \cdot \boldsymbol{\xi}_h + a^{\mathrm{s}}(\boldsymbol{d}_h^n, \boldsymbol{\xi}_h) + \alpha \int_\Sigma (\dot{\boldsymbol{d}}_h^{n-\frac{1}{2}} - \boldsymbol{u}_h^{n-1}) \cdot \boldsymbol{\xi}_h = -\int_\Sigma \boldsymbol{\lambda}_h^{n-1} \cdot \boldsymbol{\xi}_h$$

   for all $\boldsymbol{\xi}_h \in \boldsymbol{V}_h^{\mathrm{s}}$.

2. Fluid subproblem: find $(\boldsymbol{u}_h^n, p_h^n) \in \boldsymbol{V}_h^{\mathrm{f}} \times M_h^{\mathrm{f}}$ such that

$$\rho^{\mathrm{f}} \int_{\Omega^{\mathrm{f}}} \partial_\tau \boldsymbol{u}_h^n \cdot \boldsymbol{v}_h + a_h^{\mathrm{f}}((\boldsymbol{u}_h^n, p_h^n), (\boldsymbol{v}_h, q_h)) + \alpha \int_\Sigma (\boldsymbol{u}_h^n - \dot{\boldsymbol{d}}_h^{n-\frac{1}{2}}) \cdot \boldsymbol{v}_h = \int_\Sigma \boldsymbol{\lambda}_h^{n-1} \cdot \boldsymbol{v}_h$$

   for all $(\boldsymbol{v}_h, q_h) \in \boldsymbol{V}_h^{\mathrm{f}} \times M_h^{\mathrm{f}}$.

3. Fluid-stress update: set $\boldsymbol{\lambda}_h^n \in \boldsymbol{V}_h^{\mathrm{g}}$ as

$$\boldsymbol{\lambda}_h^n = \boldsymbol{\lambda}_h^{n-1} + \alpha(\dot{\boldsymbol{d}}_h^{n-\frac{1}{2}} - \boldsymbol{u}_h^n) \quad \text{on } \Sigma.$$

Algorithm A.3 Loosely coupled scheme with Robin-Robin interface conditions and midpoint scheme (LC-RR-MD) applied to the non linear problem

Given $\boldsymbol{u}_h^0, \boldsymbol{d}_h^{\mathrm{f},0}, \boldsymbol{d}_h^0, \dot{\boldsymbol{d}}_h^0, \boldsymbol{\lambda}_h^0$ and α, find $\forall n \geq 1$:

1. Solid subproblem: find $(\boldsymbol{d}_h^n, \dot{\boldsymbol{d}}_h^n) \in \boldsymbol{V}_h^{\mathrm{s}} \times \boldsymbol{V}_h^{\mathrm{s}}$, such that $\dot{\boldsymbol{d}}_h^{n-\frac{1}{2}} = \partial_\tau \boldsymbol{d}_h^n$ and

$$\rho^{\mathrm{s}} \int_{\Omega^{\mathrm{s}}} \partial_\tau \dot{\boldsymbol{d}}_h^n \cdot \boldsymbol{\xi}_h + \int_{\Omega^{\mathrm{s}}} \widetilde{\boldsymbol{\Sigma}}_h^{n-\frac{1}{2}} : \partial_{\boldsymbol{d}}(\boldsymbol{E}_h^{n-\frac{1}{2}})\boldsymbol{\xi}_h + \alpha \int_\Sigma (\dot{\boldsymbol{d}}^{n-\frac{1}{2}} - \widehat{\boldsymbol{u}}_h^{n-1}) \cdot \boldsymbol{\xi}_h = \int_\Sigma \boldsymbol{\lambda}_h^{n-\frac{3}{2}} \cdot \boldsymbol{\xi}_h$$

   for all $\boldsymbol{\xi}_h \in \boldsymbol{V}_h^{\mathrm{s}}$.
2. Update fluid domain:

$$\boldsymbol{d}_h^{\mathrm{f},n} = \boldsymbol{\mathcal{L}}(\boldsymbol{d}_h^{n-1}|_\Sigma), \quad \boldsymbol{w}_h^n = \partial_\tau \boldsymbol{d}_h^{\mathrm{f},n}, \quad \boldsymbol{\mathcal{A}}_h^n = \boldsymbol{I}_{\Omega^{\mathrm{f}}} + \boldsymbol{d}_h^{\mathrm{f},n}, \quad \Omega^{\mathrm{f},n} = \boldsymbol{\mathcal{A}}_h^n(\Omega^{\mathrm{f}}).$$

3. Fluid subproblem: find $(\widehat{\boldsymbol{u}}_h^n, \widehat{p}_h^n) \in \boldsymbol{V}_h^{\mathrm{f}} \times M_h^{\mathrm{f}}$ such that

$$\frac{\rho^{\mathrm{f}}}{\tau}\left(\int_{\Omega^{\mathrm{f},n}} \boldsymbol{u}_h^n \cdot \boldsymbol{v}_h - \int_{\Omega^{\mathrm{f},n-1}} \boldsymbol{u}_h^{n-1} \cdot \boldsymbol{v}_h\right) + a_{\Omega^{\mathrm{f},n}}(\boldsymbol{u}_h^{n-1}, \boldsymbol{w}_h^n; (\boldsymbol{u}_h^n, p_h^n), (\boldsymbol{v}_h, q_h)) + \alpha \int_\Sigma (\widehat{\boldsymbol{u}}_h^n - \dot{\boldsymbol{d}}_n^{n-\frac{1}{2}}) \cdot \boldsymbol{v}_h = -\int_\Sigma \boldsymbol{\lambda}^{n-1} \cdot \boldsymbol{v}_h$$

   for all $(\boldsymbol{v}_h, q_h) \in \boldsymbol{V}_h^{\mathrm{f}} \times M_h^{\mathrm{f}}$.
4. Fluid-stress update: set $\boldsymbol{\lambda}_h^n \in \boldsymbol{V}_h^{\mathrm{g}}$ as

$$\boldsymbol{\lambda}_h^n = \boldsymbol{\lambda}_h^{n-1} + \alpha(\dot{\boldsymbol{d}}_h^{n-\frac{1}{2}} - \widehat{\boldsymbol{u}}_h^n) \quad \text{on } \Sigma.$$

B | Neumann-Robin loosely coupled scheme with correction iterations

In this appendix, we want to state the formulation of the LC-NR-BDF1 and LC-NR-MD with correction iterations. We introduce the following notation:

$$\partial_\tau f^{n,k} := \frac{f^{n,k} - f^{n-1}}{\tau}, \qquad f^{n-\frac{1}{2},k} := \frac{f^{n,k} + f^{n-1}}{2}$$

where f is a generic variable, and $f^{n,k}$ is the approximation of f^n at the k-th subiteration.

The formulations are reported in Algorithms B.1 and B.2.

Note that when $K = 1$, the algorithms reduce to the original formulations without correction iterations (Algorithms 3.1 and 3.2 respectively). On the other hand, when $K \to \infty$, i.e. when we iterate until convergence, we retrieve the strongly coupled scheme (Algorithm 2.1).

The same scheme can also be applied to the nonlinear problem (6.2). The formulation is reported in Algorithm B.3. Again, when $K = 1$, it reduces to Algorithm 6.2, whereas, when $K \to \infty$, it coincides with Algorithm 6.1.

Algorithm B.1 Loosely coupled scheme with Neumann-Robin interface conditions and BDF1 time discretization with $K \geq 1$ correction iterations (LC-NR-BDF1-CI)

Given $\boldsymbol{u}_h^0, \boldsymbol{d}_h^0, \dot{\boldsymbol{d}}_h^0, \boldsymbol{\lambda}_h^0$ and α, find $\forall n \geq 1$:

- Initialize iteration $k = 0$:

$$\boldsymbol{u}_h^{n,0} = \boldsymbol{u}_h^{n-1}, \quad \boldsymbol{d}_h^{n,0} = \boldsymbol{d}_h^{n-1}, \quad \dot{\boldsymbol{d}}_h^{n,0} = \dot{\boldsymbol{d}}_h^{n-1}, \quad \boldsymbol{\lambda}_h^{n,0} = \boldsymbol{\lambda}_h^{n-1}.$$

- Repeat for $k = 1, \ldots, K$:
  1. Solid subproblem: find $\boldsymbol{d}_h^{n,k}$, $\dot{\boldsymbol{d}}_h^{n,k} \in \boldsymbol{V}_h^{\mathrm{s}}$, such that $\dot{\boldsymbol{d}}_h^{n,k} = \partial_\tau \boldsymbol{d}_h^{n,k}$ and

$$\rho^{\mathrm{s}} \int_{\Omega^{\mathrm{s}}} \partial_\tau \dot{\boldsymbol{d}}_h^{n,k} \cdot \boldsymbol{\xi}_h + a^{\mathrm{s}}(\boldsymbol{d}_h^{n,k}, \boldsymbol{\xi}_h) + \alpha \int_\Sigma (\dot{\boldsymbol{d}}_h^{n,k} - \boldsymbol{u}_h^{n,k-1}) \cdot \boldsymbol{\xi}_h = \int_\Sigma \boldsymbol{\lambda}_h^{n,k-1} \cdot \boldsymbol{\xi}_h$$

     for all $\boldsymbol{\xi}_h \in \boldsymbol{V}_h^{\mathrm{s}}$.
  2. Solid-stress update: set $\boldsymbol{\lambda}_h^{n,k} \in \boldsymbol{V}_h^{\mathrm{s}}$ as

$$\boldsymbol{\lambda}_h^{n,k} = \boldsymbol{\lambda}_h^{n,k-1} + \alpha(\boldsymbol{u}_h^{n,k-1} - \dot{\boldsymbol{d}}_h^{n,k}) \quad \text{on } \Sigma.$$

  3. Fluid subproblem: find $(\boldsymbol{u}_h^{n,k}, p_h^{n,k}) \in \boldsymbol{V}_h^{\mathrm{f}} \times M_h^{\mathrm{f}}$ such that

$$\rho^{\mathrm{f}} \int_{\Omega^{\mathrm{f}}} \partial_\tau \boldsymbol{u}_h^{n,k} \cdot \boldsymbol{v}_h + a_h^{\mathrm{f}}((\boldsymbol{u}_h^{n,k}, p_h^{n,k}), (\boldsymbol{v}_h, q_h)) = -\int_\Sigma \boldsymbol{\lambda}_h^{n,k} \cdot \boldsymbol{v}_h$$

     for all $(\boldsymbol{v}_h, q_h) \in \boldsymbol{V}_h^{\mathrm{f}} \times M_h^{\mathrm{f}}$.
- Update:

$$\boldsymbol{u}_h^n := \boldsymbol{u}_h^{n,K}, \quad \boldsymbol{d}_h^n := \boldsymbol{d}_h^{n,K}, \quad \dot{\boldsymbol{d}}_h^n := \dot{\boldsymbol{d}}_h^{n,K}, \quad \boldsymbol{\lambda}_h^n := \boldsymbol{\lambda}_h^{n,K}.$$

Algorithm B.2 Loosely coupled scheme with Neumann-Robin interface conditions and mid-point time discretization with $K \geq 1$ correction iterations (LC-NR-MD-CI)

Given $\boldsymbol{u}_h^0, \boldsymbol{d}_h^0, \dot{\boldsymbol{d}}_h^0, \boldsymbol{\lambda}_h^0$ and α, find $\forall n \geq 1$:

- Initialize iteration $k = 0$:

$$\boldsymbol{u}_h^{n,0} = \boldsymbol{u}_h^{n-1}, \quad \boldsymbol{d}_h^{n,0} = \boldsymbol{d}_h^{n-1}, \quad \dot{\boldsymbol{d}}_h^{n,0} = \dot{\boldsymbol{d}}_h^{n-1}, \quad \boldsymbol{\lambda}_h^{n-\frac{1}{2},0} = \boldsymbol{\lambda}_h^{n-\frac{3}{2}}.$$

- Repeat for $k = 1, \ldots, K$:
  1. Solid subproblem: find $\boldsymbol{d}_h^{n,k}$, $\dot{\boldsymbol{d}}_h^{n,k} \in \boldsymbol{V}_h^{\mathrm{s}}$, such that $\dot{\boldsymbol{d}}_h^{n-\frac{1}{2},k} = \partial_\tau \boldsymbol{d}_h^{n,k}$ and

$$\rho^{\mathrm{s}} \int_{\Omega^{\mathrm{s}}} \partial_\tau \dot{\boldsymbol{d}}_h^{n,k} \cdot \boldsymbol{\xi}_h + a^{\mathrm{s}}(\boldsymbol{d}_h^{n-\frac{1}{2},k}, \boldsymbol{\xi}_h) + \alpha \int_\Sigma (\dot{\boldsymbol{d}}_h^{n-\frac{1}{2},k} - \boldsymbol{u}_h^{n,k-1}) \cdot \boldsymbol{\xi}_h = \int_\Sigma \boldsymbol{\lambda}_h^{n-\frac{1}{2},k-1} \cdot \boldsymbol{\xi}_h$$

     for all $\boldsymbol{\xi}_h \in \boldsymbol{V}_h^{\mathrm{s}}$.
  2. Solid-stress update: set $\boldsymbol{\lambda}_h^{n-\frac{1}{2},k} \in \boldsymbol{V}_h^{\mathrm{g}}$ as

$$\boldsymbol{\lambda}_h^{n-\frac{1}{2},k} = \boldsymbol{\lambda}_h^{n-\frac{1}{2},k-1} + \alpha(\boldsymbol{u}_h^{n,k-1} - \dot{\boldsymbol{d}}_h^{n-\frac{1}{2},k}) \quad \text{on } \Sigma.$$

  3. Fluid subproblem: find $(\boldsymbol{u}_h^{n,k}, p_h^{n,k}) \in \boldsymbol{V}_h^{\mathrm{f}} \times M_h^{\mathrm{f}}$ such that

$$\rho^{\mathrm{f}} \int_{\Omega^{\mathrm{f}}} \partial_\tau \boldsymbol{u}_h^{n,k} \cdot \boldsymbol{v}_h + a_h^{\mathrm{f}}((\boldsymbol{u}_h^{n,k}, p_h^{n,k}), (\boldsymbol{v}_h, q_h)) = -\int_\Sigma \boldsymbol{\lambda}_h^{n-\frac{1}{2},k} \cdot \boldsymbol{v}_h$$

     for all $(\boldsymbol{v}_h, q_h) \in \boldsymbol{V}_h^{\mathrm{f}} \times M_h^{\mathrm{f}}$.
- Update:

$$\boldsymbol{u}_h^n := \boldsymbol{u}_h^{n,K}, \quad \boldsymbol{d}_h^n := \boldsymbol{d}_h^{n,K}, \quad \dot{\boldsymbol{d}}_h^n := \dot{\boldsymbol{d}}_h^{n,K}, \quad \boldsymbol{\lambda}_h^{n-\frac{1}{2}} := \boldsymbol{\lambda}_h^{n-\frac{1}{2},K}.$$

Algorithm B.3 Loosely coupled scheme with Neumann-Robin interface conditions and mid-point scheme in the solid and $K \geq 1$ correction iterations (LC-NR-MD-CI) applied to the non linear problem

Given $\boldsymbol{u}^0, \boldsymbol{d}_h^{\mathrm{f},0}, \boldsymbol{d}^0, \dot{\boldsymbol{d}}^0, \boldsymbol{\lambda}_h^0$ and α, find $\forall n \geq 1$:

- Update fluid domain:

$$\boldsymbol{d}_h^{\mathrm{f},n} = \boldsymbol{\mathcal{L}}(\boldsymbol{d}_h^{n-1}|_\Sigma), \quad \boldsymbol{w}_h^n = \partial_\tau \boldsymbol{d}_h^{\mathrm{f},n}, \quad \boldsymbol{\mathcal{A}}_h^n = \boldsymbol{I}_{\Omega^\mathrm{f}} + \boldsymbol{d}_h^{\mathrm{f},n}, \quad \Omega^{\mathrm{f},n} = \boldsymbol{\mathcal{A}}_h^n(\Omega^\mathrm{f}).$$

- Initialize iteration $k = 0$:

$$\boldsymbol{u}_h^{n,0} = \boldsymbol{u}_h^{n-1}, \quad \boldsymbol{d}_h^{n,0} = \boldsymbol{d}_h^{n-1}, \quad \dot{\boldsymbol{d}}_h^{n,0} = \dot{\boldsymbol{d}}_h^{n-1}, \quad \boldsymbol{\lambda}_h^{n-\frac{1}{2},0} = \boldsymbol{\lambda}_h^{n-\frac{3}{2}}.$$

- Repeat for $k = 1, \ldots, K$
  1. Solid subproblem: find $(\boldsymbol{d}_h^{n,k}, \dot{\boldsymbol{d}}_h^{n,k}) \in \boldsymbol{V}_h^\mathrm{s} \times \boldsymbol{V}_h^\mathrm{s}$, such that $\dot{\boldsymbol{d}}_h^{n-\frac{1}{2},k} = \partial_\tau \boldsymbol{d}_h^{n,k}$ and

$$\rho^\mathrm{s} \int_{\Omega^\mathrm{s}} \partial_\tau \dot{\boldsymbol{d}}_h^{n,k} \cdot \boldsymbol{\xi}_h + \int_{\Omega^\mathrm{s}} \widetilde{\boldsymbol{\Sigma}}_h^{n-\frac{1}{2},k} : \partial_{\boldsymbol{d}}(\boldsymbol{E}_h^{n-\frac{1}{2},k})\boldsymbol{\xi}_h + \alpha \int_\Sigma (\dot{\boldsymbol{d}}^{n-\frac{1}{2},k} - \widehat{\boldsymbol{u}}_h^{n,k-1}) \cdot \boldsymbol{\xi}_h = \int_\Sigma \boldsymbol{\lambda}_h^{n-\frac{1}{2},k-1} \cdot \boldsymbol{\xi}_h$$

     for all $\boldsymbol{\xi}_h \in \boldsymbol{V}_h^\mathrm{s}$.
  2. Solid-stress update: set $\boldsymbol{\lambda}_h^{n-\frac{1}{2},k} \in \boldsymbol{V}_h^\mathrm{s}$ as

$$\boldsymbol{\lambda}_h^{n-\frac{1}{2},k} = \boldsymbol{\lambda}_h^{n-\frac{1}{2},k-1} \alpha(\widehat{\boldsymbol{u}}^{n-1} - \dot{\boldsymbol{d}}^{n-\frac{1}{2},k}) \quad \text{on } \Sigma.$$

  3. Fluid subproblem: find $(\widehat{\boldsymbol{u}}_h^{,k}, \widehat{p}_h^{n,k}) \in \boldsymbol{V}_h^\mathrm{f} \times M_h^\mathrm{f}$ such that

$$\frac{\rho^\mathrm{f}}{\tau}\left(\int_{\Omega^{\mathrm{f},n}} \boldsymbol{u}_h^{n,k} \cdot \boldsymbol{v}_h - \int_{\Omega^{\mathrm{f},n-1}} \boldsymbol{u}_h^{n-1} \cdot \boldsymbol{v}_h\right) + a_{\Omega^{\mathrm{f},n}}(\boldsymbol{u}_h^{n-1}, \boldsymbol{w}_h^{n,k}; (\boldsymbol{u}_h^{n,k}, p_h^{n,k}), (\boldsymbol{v}_h, q_h)) = \int_\Sigma J^n \widehat{\boldsymbol{\sigma}}(\boldsymbol{u}^{n,k}, p^{n,k})(\boldsymbol{F}^{n,k})^{-\mathrm{T}} \widehat{\boldsymbol{n}} \cdot \boldsymbol{v}_h$$

     for all $(\boldsymbol{v}_h, q_h) \in \boldsymbol{V}_h^\mathrm{f} \times M_h^\mathrm{f}$.
- Update:

$$\boldsymbol{u}_h^n := \boldsymbol{u}_h^{n,K}, \quad \boldsymbol{d}_h^n := \boldsymbol{d}_h^{n,K}, \quad \dot{\boldsymbol{d}}_h^n := \dot{\boldsymbol{d}}_h^{n,K}, \quad \boldsymbol{\lambda}_h^{n-\frac{1}{2}} := \boldsymbol{\lambda}_h^{n-\frac{1}{2},K}.$$

List of Symbols and Nomenclature

All the main symbols and acronyms are summarized in the following table.

Symbol	Description
Ω^{s}	Solid domain
Ω^{f}	Fluid domain
Σ	Interface
ρ^{s}	Solid density
ρ^{f}	Fluid density
μ	Fluid viscosity
$\boldsymbol{d}$	Solid displacement
$\dot{\boldsymbol{d}}$	Solid velocity
$\boldsymbol{u}$	Fluid velocity
p	Fluid pressure
$\boldsymbol{\sigma}(\boldsymbol{u}, p)$	Fluid stress tensor
$\boldsymbol{\sigma}(\boldsymbol{d})$	Solid stress tensor
$\boldsymbol{\epsilon}(\boldsymbol{u})$	Strain rate tensor of the fluid
$\boldsymbol{\epsilon}(\boldsymbol{d})$	Strain tensor of the solid
L_1, L_2	Lamè coefficients
α	Robin parameter
τ	Time step size
h	Mesh size
ALE	Arbitrary Lagrangian-Eulerian
BDF1	Backward Differentiation Formula of order 1
CI	Correction iterations
CFL	Courant-Friedrichs-Lewy condition
FSI	Fluid-Structure Interaction
LC	Loosely coupled

Symbol	Description
MD	Mid-point scheme
MONO	Monolithic scheme
NR	Neumann-Robin scheme
PDE	Partial Differential Equation
RN	Robin-Neumann scheme
RR	Robin-Robin scheme
SC	Strongly coupled

All the algorithms in this thesis are denoted using a precisely defined nomenclature, with the following structure:

- SC, LC, MONO: defines the type of coupling (strongly coupled, loosely coupled or monolithic);
- RR, RN, NR: specifies the update strategy for the coupling conditions (Robin-Robin, Robin-Neumann or Neumann-Robin);
- BDF1, MD: represents the time stepping scheme (Backward Differentiation Formula of order 1 or Mid-point). The fluid is always treated with BDF1, while the solid equation can be treated either with BDF1 or MD. As a consequence, this label will specify the time discretization of the solid;
- CI: the presence of this label identifies if the algorithm employs correction iterations.

Following this notation, the scheme LC-RN-BDF1-CI will identify a loosely coupled scheme with Robin-Neumann interface coupling, time-integrated using the BDF1 scheme in the solid and the fluid, and employing correction iterations.

List of Figures

List of Algorithms

List of Tables

Acknowledgments

I would like to start thanking my internship's supervisor Miguel, who allowed me to be part of the team. I want to thank you for the support, motivation and patience during my stage. Above all, I want to thank you for giving me a brief insight into how wonderful and rewarding the world of research is.

I also want to express my gratitude to all the members of the COMMEDIA team that I had the pleasure to meet, in particular Corrie, Marguerite, Donjiao, Carlos, Davide, Daniele, and Romain because you welcomed me from the first day. A special mention goes to Carlos for helping me install `FELiScE`, because without your help, part of this thesis would not have been possible.

Un grazie infinite al mio relatore Christian Vergara, per la disponibilità e l'attenzione con cui ha seguito fin da subito il mio percorso di stage dall'Italia. La sua guida costante e i suoi preziosi consigli hanno rappresentato un supporto fondamentale per ampliare il lavoro svolto e trasformarlo in una vera e propria tesi.

E ora, i ringraziamenti che parlano del cuore, forse i più difficili.

Il primo grazie lo dedico alle mie insegnanti di matematica: Maestra Marinella, Prof.ssa Ampollini, Prof.ssa Ermasi e Prof.essa Palermo. Quattro donne, quattro voci che hanno saputo accendere in me la scintilla e desiderio di scoprire i segreti della matematica.

Grazie Simo, Sara, Faby e Mattia. A un'amicizia che da dieci anni attraversa distanze, tempi e imprevisti, ma trova sempre il modo di farci ritrovare. A quel filo invisibile che continua a legarci. Grazie Cri. A te che mi hai riportata in acqua e nel mio equilibrio.

Un grazie a tutti gli amici incontrati all'università per aver reso questi anni più leggeri. In particolare, grazie Leti. La mia *stellina* dal primo giorno di uni, perchè con te ho affrontato ogni singolo momento, ogni esame e ogni cambiamento. A tutta la forza e il sostegno che mi hai trasmesso in questi anni. Grazie Filo, che da quando ti ho conosciuto, sei stato per me la definizione di cosa significa davvero mettere passione in quello che si fa. Grazie Pol, per essere stata la mia controparte calma nei momenti più stressanti e sempre pronto a rispondere a tutti i miei centocinquantamila stupidi dubbi.

Grazie Giuls, Ali, Lu e Nic. Grazie a voi per essere stati i migliori compagni di viaggio, paure, sogni, e leggerezza che potessi desiderare. Con voi, ogni angolo di Parigi ha trovato la sua storia. Thanks to Julia, Sylvia, Ludovica, Enrico, Giovanni, Arthur, Ola, Sam and Sara. I will forever be grateful for Wednesday dinners, because you made me feel home, especially when Paris did not quite feel like home.

Un piccolo grazie va anche a Parigi: non è stato di certo amore a prima vista, ma mi hai offerto possibilità di vita e versioni di me stessa che ancora non conoscevo.

Grazie Mamma e Papà. Il grazie più grande è per voi. Grazie Mamma per avermi insegnato l'importanza della gentilezza, del rispetto e della pazienza, e per rappresentare per me il modello di donna che voglio perseguire. Grazie Papà per avermi sempre spinto a essere curiosa, a pormi domande scomode, stimolandomi costantemente a raggiungere i miei obiettivi, perchè mi hai reso una persona più forte. Grazie a entrambi per la pasta fresca, le crespelle di Natale, e le nostre lunghe chiacchierate serali, perchè mi hanno insegnato che *sono le piccole cose belle che regalano felicità, e ti cambiano la giornata se le vivi con semplcità.* Grazie per aver sempre creduto in me più di quanto ci credessi io: se sono arrivata fino a qua, è anche grazie a voi.

Grazie Nonna Rita, per avermi aiutato *in silenzio* con le tue preghiere. E grazie ai Nonni, che spero ogni tanto guardino giù da lassù. Grazie a Zio Genny, Zio Alfio, Zia Silvana e Zia Alina per tutto l'affetto sincero che mi avete sempre dato.

Grazie Lara, mia complice nel disordine della vita. Che la vita possa sorprenderti con la stessa meraviglia che hai avuto quando hai scoperto perchè $\sin^2 x + \cos^2 x = 1$.

Grazie Jacopo, a te che sei stato il mio compagno di vita per gli ultimi cinque anni. Grazie per essere stato il mio porto sicuro, in ogni luogo e in ogni tempo, anche quando fuori infuriava la tempesta.

Da qualche parte tra Milano e Parigi,
December 10, 2025